

HYDROGEN ADSORPTION ON Cu (I)-EXCHANGED ZEOLITES

A THESIS SUBMITTED TO
THE GRADUATE SCHOOL OF NATURAL AND APPLIED SCIENCES
OF
MIDDLE EAST TECHNICAL UNIVERSITY

BY

İSMIHAN ALTIPARMAK

IN PARTIAL FULFILLMENT OF THE REQUIREMENTS
FOR
THE DEGREE OF MASTER OF SCIENCE
IN
CHEMICAL ENGINEERING

JANUARY 2019

Approval of the thesis:

HYDROGEN ADSORPTION ON CU (I)-EXCHANGED ZEOLITES

submitted by **İSMİHAN ALTIPARMAK** in partial fulfillment of the requirements for the degree of **Master of Science in Chemical Engineering Department, Middle East Technical University** by,

Prof. Dr. Halil Kalıpçılar
Dean, Graduate School of **Natural and Applied Sciences**

Prof. Dr. Pınar Çalık
Head of Department, **Chemical Engineering**

Assist. Prof. Dr. Bahar İpek Torun
Supervisor, **Chemical Engineering, METU**

Prof. Dr. Deniz Üner
Co-Supervisor, **Chemical Engineering, METU**

Examining Committee Members:

Prof. Dr. Halil Kalıpçılar
Chemical Engineering, METU

Assist. Prof. Dr. Bahar İpek Torun
Chemical Engineering, METU

Prof. Dr. Deniz Üner
Chemical Engineering, METU

Assoc. Prof. Dr. Zeynep Çulfaz Emecen
Chemical Engineering, METU

Assoc. Prof. Dr. Berna Topuz
Chemical Engineering, Ankara University

Date: 23.01.2019

I hereby declare that all information in this document has been obtained and presented in accordance with academic rules and ethical conduct. I also declare that, as required by these rules and conduct, I have fully cited and referenced all material and results that are not original to this work.

Name, Surname: İsmihan Altıparmak

Signature:

ABSTRACT

HYDROGEN ADSORPTION ON CU (I)-EXCHANGED ZEOLITES

Altıparmak, İsmihan
Master of Science, Chemical Engineering
Supervisor: Assist. Prof. Dr. Bahar İpek Torun
Co-Supervisor: Prof. Dr. Deniz Üner

January 2019, 85 pages

The growing population of the world increases the energy demand exponentially; necessitating utilization of a clean and renewable energy source. In this manner, H₂ is a prominent candidate to be the future fuel by having gravimetrically high energy density, provided that a new lightweight, safe and economical onboard hydrogen storage system is developed for H₂ fueled fuel cell vehicles. In this thesis, Cu(I)-exchanged micro- and meso-porous zeolites (Cu(I)-[B]-ZSM-5, Cu(I)-[Al]-ZSM-5, mesoporous Cu(I)-[B]-ZSM-5, Cu(I)-SSZ-13, Cu(I)-SSZ-39 and Cu(I)-US-Y) are prepared and tested for H₂ adsorption at ambient temperature and low pressures. For this, a new Cu(I)-exchange method in liquid media that results in homogeneous Cu(I)-exchange is developed in this study. Using this new exchange method, Cl-free Cu(I)-samples are obtained with Cu/Al ratios reaching up to 1. Cu(I)-exchanged samples are tested for H₂ adsorption in a temperature range between 278 K and 323 K. Among the tested zeolites, the highest H₂ adsorption capacity is observed on mesoporous Cu(I)-[B]-ZSM-5 (reaching 125 $\mu\text{mol H}_2 \text{ g}_{\text{zeolite}}^{-1}$, $\text{H}_2 \text{ Cu}^{-1}$ value of 1 at 323 K and at a pressure lower than 1 bar) with initial differential heat of H₂ adsorption value of 76 kJ mol⁻¹. Cu(I)-SSZ-39 also shows high H₂ uptake capacity (reaching 60 $\mu\text{mol H}_2 \text{ g}_{\text{zeolite}}^{-1}$, $\text{H}_2 \text{ Cu}^{-1}$ value of 0.08 at 293 K and 1 bar) with an isosteric heat of adsorption value of 80 kJ mol⁻¹. The adsorption capacities of Cu(I)-zeolites and their potential for

higher pressure applications are discussed considering the H₂ binding energies, pore sizes and pore volumes of the tested zeolites.

Keywords: Hydrogen Energy, Hydrogen Storage, Zeolite, Micro- and Mesoporous Materials, Cu(I)-exchange

ÖZ

Cu(I)- İÇEREN ZEOLİTLER ÜZERİNE HİDROJEN ADSORPSİYONU

Altıparmak, İsmihan
Yüksek Lisans, Kimya Mühendisliği
Tez Danışmanı: Dr. Öğr. Üyesi Bahar İpek Torun
Ortak Tez Danışmanı: Prof. Dr. Deniz Üner

Ocak 2019, 85 sayfa

Gün geçtikçe artan dünya nüfusu enerji talebinin de katlanarak artmasına sebep olmakta ve de temiz ve yenilenebilir bir enerji kaynağına olan gereği açığa çıkarmaktadır. Bu bağlamda, hidrojen, gravimetrik olarak yüksek enerji yoğunluğuna sahip olmasıyla gelecekteki yakıt olmaya adaydır. Bunun için, araçlara monte edilebilir yeni hafif, güvenli ve ekonomik bir hidrojen depolama sisteminin geliştirilmesi gerekmektedir. Bu çalışmada, Cu(I)-iyonu içeren mikro ve mezogözenekli zeolitler (Cu(I)-[B]-ZSM-5, Cu(I)-[Al]-ZSM-5, mezogözenekli Cu(I)-[B]-ZSM-5, Cu(I)-SSZ-13, Cu(I)-SSZ-39 ve Cu(I)-US-Y) hazırlanmış ve oda sıcaklığında, düşük basınçlarda hidrojen adsorpsiyon testleri yapılmıştır. Bu sebeple, homojen bir şekilde Cu(I)- değişimine olanak sağlayacak sıvı ortamda yeni bir Cu(I)-değişim metodu geliştirilmiştir. Bu metot kullanılarak Cu/Al oranları 1'e ulaşan klorinsiz Cu(I)- zeolitler elde edilmiştir. Cu(I)- içeren örneklerin 278 K ve 323 K sıcaklık aralığında H₂ testi yapılmıştır. Test edilen zeolitler arasında, başlangıç diferansiyel H₂ adsorpsiyon ısısı 76 kJ mol⁻¹ olan mezogözenekli Cu(I)-[B]-ZSM-5'in en yüksek H₂ adsorpsiyon kapasitesine (323 K'de ve 1 bardan düşük basınçlarda 125 µmol H₂ g_{zeolit}⁻¹, H₂ Cu⁻¹=1.) sahip olduğu gözlenmiştir. İzosterik H₂ adsorpsiyon ısı değeri 80 kJ mol⁻¹ olan Cu(I)-SSZ-39 da yüksek H₂ depolama kapasitesi (293 K'de ve 1 bar'da 60 µmol H₂ g_{zeolit}⁻¹, H₂ Cu⁻¹=0.08) göstermiştir. Cu(I)-iyonu içeren zeolitlerin

adsorpsiyon kapasiteleri ve daha yüksek basınç uygulamaları için potansiyelleri, test edilen zeolitlerin H₂ bağlama enerjileri, gözenek boyut ve hacimleri dikkate alınarak tartışılmıştır.

Anahtar Kelimeler: Hidrojen Enerjisi, Hidrojen Depolama, Zeolit, Mikro- ve Mezogözenekli Materyaller, Cu(I)-değişimi

To Mom and Dad

ACKNOWLEDGMENTS

Firstly, I would like to express my deepest pleasure to my supervisor Assist. Prof. Dr. Bahar İPEK TORUN and my co-supervisor Prof. Dr. Deniz ÜNER for their advice, guidance and encouragements.

BAP-YÖP-304-2018-2839, BAP-YLT-304-2018-2712 and TÜBİTAK-117-C-024 projects are acknowledged for financial support. Sachem, Inc. is acknowledged for donating the organic structure directing agent, N,N-dimethyl-3,5-dimethylpiperidinium hydroxide for educational purposes.

I wish to thank the Zeolite Synthesis and Application Research Laboratory graduate members for their endless support and friendship through the research; Büşra Karakaya, Özgün Memioğlu, and also the undergraduate members Doğa Tektaş and Melis Özdemir.

I am also grateful to my dearest friend from undergraduate, dormitory and flat-mate Ceren Yenipınar for encouragement, friendship and unconditional support. I also wish to thank to my friends from undergraduate and graduate for their friendship through the study; Esra Alparslan, Ezgi Gözde, Gökhan Gök, Ezgi Altıntaş, Zeynep İmir, Omar Wehbe, Sevil Göktürk, Neslin Güler, Batıkan Şencan and Salih Memiş.

My special thanks to my siblings-in-law Emine Yıldırım from primary school, Ceren Dinçel, Utku Öztürk, İremnur Kara, Berat Şengörür and Ada Çelik from high school for being always by my side, encouraging me and their endless friendship.

Before the final appreciation, I wish to thank to my love, Serhat Kağan Çalışkan, for always holding my hand and making me believe myself in those tiring and stressful times.

Last but foremost, I would like to express my appreciation to my mother Havva Gülseven Altıparmak and my father Yücel Altıparmak for their unconditional love, endless support and trust.

TABLE OF CONTENTS

ABSTRACT	v
ÖZ	vii
ACKNOWLEDGMENTS	x
TABLE OF CONTENTS	xi
LIST OF TABLES	xiv
LIST OF FIGURES	xvi
LIST OF SYMBOLS	xix
CHAPTERS	
1. INTRODUCTION	1
1.1. Hydrogen; the Fuel of Future	1
1.1.1. Production of Hydrogen	2
1.2. Usage of Hydrogen Energy	3
1.3. Advantages and Disadvantages of Hydrogen Energy	4
1.4. Storage of Hydrogen Gas/Energy	5
1.4.1. Compressed Hydrogen	5
1.4.2. Liquified Hydrogen	6
1.4.3. Chemisorption	6
1.4.4. Physisorption	8
1.4.4.1. Porous Carbons	9
1.4.4.2. Metal Organic Frameworks (MOFs)	9
1.4.4.3. Zeolites	13
1.4.4.4. Cu-exchanged Zeolites	15

1.4.4.5. Mesoporous Materials	17
2. EXPERIMENTAL PROCEDURE.....	19
2.1. Synthesis of the Zeolites	19
2.2. Ion-Exchange Procedure	22
2.2.1. Ammonium-Exchange.....	22
2.2.2. Copper(I)-Exchange	22
2.3. Characterization Tests.....	23
2.4. Hydrogen Tests	23
2.4.1. Adsorption Calorimetry Tests	24
2.4.1.1. Vacuum Pretreatment	24
2.4.1.2. Hydrogen Adsorption Experiments	24
2.4.2. Hydrogen Tests in Physisorption Device	24
2.4.2.1. Degas Pretreatment.....	24
2.4.2.2. Hydrogen Adsorption Test	25
3. RESULTS AND DISCUSSION	27
3.1. ZSM-5 Results	27
3.1.1. Characterization Results.....	27
3.1.1.1. XRD.....	27
3.1.1.2. SEM Images.....	28
3.1.1.3. Elemental Analysis	29
3.1.1.4. Pore Volume Characterization.....	31
3.1.2. Adsorption Calorimetry Results.....	32
3.1.2.1. Adsorption Isotherms.....	32
3.1.2.2. Differential Heat of Adsorption.....	34

3.2. SSZ-13, SSZ-39, US-Y Results	35
3.2.1. Characterization Results	35
3.2.1.1. XRD	35
3.2.1.2. SEM Images	37
3.2.1.3. Elemental Analysis.....	38
3.2.1.4. Pore Volume Characterization	41
3.2.2. Hydrogen Adsorption Results.....	44
3.2.2.1. Adsorption Isotherms	44
3.2.2.2. Isosteric Heat of Adsorption	50
4. CONCLUSION.....	57
REFERENCES.....	59
APPENDICES	71
A. Cu(I)-ZSM-5 H ₂ Adsorption Data and Differential Heat of Adsorption Calculations.....	69
B. Cu(I)-SSZ-13, -SSZ-39, -US-Y, H ₂ Isotherms and Isosteric Heat of Adsorption Calculations.....	76

LIST OF TABLES

TABLES

Table 1.1. Chemisorption materials and H ₂ storage capacities	7
Table 1.2. Technical targets for on-board hydrogen storage systems reported by DOE	9
Table 1.3. Surface area, H ₂ uptake capacity and enthalpy of H ₂ adsorption data of metal organic frameworks	12
Table 1.4. Heat of adsorption values of alkali and earth alkali metal containing zeolites	14
Table 1.5. H ₂ uptake capacity and enthalpy of H ₂ adsorption data of alkali metal and alkaline earth metal-exchanged zeolites	15
Table 3.1. Elemental analysis of Cu(I)-[Al]-ZSM-5, Cu(I)-[B]-ZSM-5 and mesoporous Cu(I)-[B]-ZSM-5 exchanged in 0.01 M CuCl-acetonitrile solution.	30
Table 3.2. Cu-exchange results of [B]-ZSM-5 in different molarity of CuCl/acetonitrile solutions.	31
Table 3.3. Micro- and meso-pore volumes of [Al]-ZSM-5, [B]-ZSM-5 and mesoporous [B]-ZSM-5 before and after Cu(I)-exchange.	32
Table 3.4. Elemental analysis of Cu(I)-SSZ-13, Cu(I)-SSZ-39, Cu(I)-US-Y and acid treated Cu(I)-SSZ-39 (acid-Cu(I)-SSZ-39) obtained by ICP-EOS and EDX methods.	40
Table 3.5. Pore volumes of zeolites; SSZ-13, SSZ-39, US-Y and acid-treated SSZ-39 (acid-SSZ-39) before and performing Cu(I)-exchange.	43
Table 3.6. Sips adsorption model fitting parameters of Cu(I)-SSZ-39, Cu(I)-SSZ-1 and, Cu(I)-US-Y at 77 K.	49
Table 3.7 Langmuir adsorption model fitting parameters of Cu(I)-SSZ-39, Cu(I)-SSZ-1 and, Cu(I)-US-Y at 77 K	50

Table 3.8. Data used to obtain isosteric heat of adsorption of Cu(I)-SSZ-39 between the temperatures 278.6 K and 304 K.....	52
Table A.1. H ₂ adsorption data obtained from adsorption calorimetry device for Cu(I)-[Al]-ZSM-5	71
Table A.2. H ₂ adsorption data obtained from adsorption calorimetry device for Cu(I)-[B]-ZSM-5	72
Table A.3. H ₂ adsorption data obtained from adsorption calorimetry device for mesoporous Cu(I)-[B]-ZSM-5	73
Table A.4: Hydrogen adsorption data at different temperatures of Cu(I)-SSZ-39	76
Table A.5: Hydrogen adsorption data at different temperatures of Cu(I)-US-Y	77
Table A.6. Cu(I)-SSZ-39 Sips adsorption model fitting parameters for pressures between 10.40-198.47 mmHg for 278.6 K; 10.09-198.34 mmHg for 295.9 K and 1.25-198.38 mmHg for 304 K.	78
Table A.7. Cu(I)-SSZ-39 Linear adsorption model fitting parameters for pressures between 198.47-807.40 mmHg for 278.6 K; 198.34-812.95 mmHg for 295.9 K and 198.38-807.30 mmHg for 304 K.....	78
Table.A.8 Cu(I)-US-Y Linear adsorption model fitting parameters for pressures between 148.80-811.98 mmHg for 278.8 K; 364.94-811.36 mmHg for 293.9 K and 364.94-811.36 mmHg for 295.9 K.....	78
Table A.9. Data used to obtain isosteric heat of adsorption of Cu(I)-US-Y between the temperatures 278.6 K and 304 K.....	80
Table A.10 : Hydrogen adsorption data at different temperatures of Cu(I)-SSZ-13 .	82
Table A.11. Cu(I)-SSZ-13 Sips adsorption model fitting parameters for pressures between 1.55-263.45 mmHg for 278.6 K; 1.78-159.39 mmHg for 295.9 K and 10.60-148.70 mmHg for 304 K.....	83
Table A.12. Cu(I)-SSZ-13 Linear adsorption model fitting parameters for pressures between 263.45-811.09 mmHg for 278.6 K;159.39-813.05 mmHg for 295.9 K and 148.70-807.40 mmHg for 304 K.....	83
Table A.13.Data used to obtain isosteric heat of adsorption of Cu(I)-SSZ-13 between the temperatures 278.6 K and 304 K.....	87

LIST OF FIGURES

FIGURES

Figure 1.1. Schematic of a single fuel-cell	4
Figure 3.1. XRD patterns of [B]-ZSM-5, [Al]-ZSM-5 and mesoporous [B]-ZSM-5 (wavelength= 0.15418 nm).....	28
Figure 3.2. XRD patterns of [B]-ZSM-5 and [Al]-ZSM-5 in Na and Cu form (wavelength=0.15418 nm).....	28
Figure 3.3. SEM images of zeolites; a) Cu(I)-[B]-ZSM-5, b) Cu(I)-[Al]-ZSM-5, c) mesoporous Cu(I)-[B]-ZSM-5.....	29
Figure 3.4. H ₂ adsorption isotherms of Cu(I)-[Al]-ZSM-5, Cu(I)-[B]-ZSM-5 and mesoporous Cu(I)-[B]-ZSM-5 at 293 K.....	33
Figure 3.5. H ₂ adsorption isotherms of Cu(I)-[Al]-ZSM-5, Cu(I)-[B]-ZSM-5 and mesoporous Cu(I)-[B]-ZSM-5 on a per Cu-basis at 293 K.....	33
Figure 3.6. Differential heat of adsorption for Cu(I)-[Al]-ZSM-5, Cu(I)-[B]-ZSM-5 and mesoporous Cu(I)-[B]-ZSM-5 obtained at 323 K.	35
Figure 3.7. A) XRD patterns of SSZ-13, SSZ-39, acid-treated SSZ-39 (acid-SSZ-39), US-Y and acid-treated US-Y (acid-US-Y) B) Cu(I)-SSZ-13, Cu(I)-SSZ-39, Cu(I)-US-Y.	36
Figure 3.8. SEM images of zeolites a) Cu(I)-SSZ-13, b) Cu(I)-SSZ-39, c) Cu(I)-US-Y, d) acid-treated Cu(I)-SSZ-39.	37
Figure 3.9: Nitrogen adsorption/desorption isotherms at 77 K for SSZ-13 before and after Cu(I)-exchange.....	42
Figure 3.10: Nitrogen adsorption/desorption isotherms at 77 K for SSz-39 before and after Cu(I)-exchange.....	42
Figure 3.11: Nitrogen adsorption/desorption isotherms at 77 K for US-Y before and after Cu(I)-exchange.....	43

Figure 3.12. Adsorption isotherms of Cu(I)-SSZ-13, Cu(I)-SSZ-39 and Cu(I)-US-Y at 293 K.....	45
Figure 3.13. Adsorption isotherms in H ₂ /Cu of Cu(I)-SSZ-13, Cu(I)-SSZ-39 and Cu(I)-US-Y at 293 K.....	45
Figure 3.14. H ₂ adsorption isotherms of Cu(I)-SSZ-13, Cu(I)-SSZ-39 and Cu(I)-US-Y at 77 K.....	47
Figure 3.15. H ₂ adsorption isotherms in H ₂ /Cu of Cu(I)-SSZ-13, Cu(I)-SSZ-39 and Cu(I)-US-Y at 77 K.....	47
Figure 3.16. Experimental H ₂ adsorption on Cu(I)-SSZ-13 at 77 K, Sips adsorption model and Langmuir adsorption model	48
Figure 3.17. Experimental H ₂ adsorption on Cu(I)-SSZ-39 at 77 K, Sips adsorption model and Langmuir adsorption model	48
Figure 3.18. Experimental H ₂ adsorption on Cu(I)-US-Y at 77 K, Sips adsorption model and Langmuir adsorption model	49
Figure 3.19. Experimental H ₂ adsorption data on Cu(I)-SSZ-39 at 278.6 K, 295.9 K and 304 K, fitted Sips adsorption (continuous line) and linear models (dashed lines)	51
Figure 3.20. ln(P) versus 1/T of Cu(I)-SSZ-39 at quantity adsorbed = 0.024 mmol H ₂ g ⁻¹	52
Figure 3.21. Isothermic heat of H ₂ adsorption of Cu(I)-SSZ-39 between 278.6 K and 304 K.....	53
Figure 3.22. Isothermic heat of H ₂ adsorption of Cu(I)-US-Y between 278.8 K and 303 K.....	53
Figure 3.23. Isothermic heat of adsorption data versus H ₂ Cu ⁻¹ ratio of Cu(I)-SSZ-39 and Cu(I)-US-Y between the temperatures of 278 and 304 K.....	55
Figure 3.24. Schematic drawing of SSZ-39 (AEI), SSZ-13 (CHA), Zeolite-Y (FAU) and building units.....	55
Figure A.1: Nitrogen adsorption/desorption isotherms at 77 K for [B]-ZSM-5	69
Figure A.2: Nitrogen Adsorption/desorption isotherms at 77 K for [Al]-ZSM-5	70

Figure A.3: Nitrogen adsorption/desorption isotherms at 77 K for mesoporous [B]-ZSM-5.....	70
Figure A.4. H ₂ adsorption isotherms of Cu(I)-SSZ-39, Cu(I)-US-Y, Cu(I)-SSZ-13 and blank tube at 293 K.....	74
Figure A.5. H ₂ adsorption isotherms of Cu(I)-SSZ-13, Cu(I)-SSZ-39, Cu(I)-US-Y, Acid-Cu(I)-SSZ-39 at 278 K	74
Figure A.6. H ₂ adsorption isotherms of Cu(I)-SSZ-39 at different temperatures	75
Figure A.7. H ₂ adsorption isotherms of Cu(I)-US-Y at different temperatures	75
Figure A.8. Experimental H ₂ adsorption data on Cu(I)-US-Y at 278.6 K, 293.9 K and 304 K linear models (dashed lines)	79
Figure A.9. ln(P) versus 1/T of Cu(I)-US-Y at quantity adsorbed = 0.018 mmol H ₂ g ⁻¹	79
Figure A.10. XRD patterns of SSZ-13 before and after Cu(I)-exchange	81
Figure A.11. H ₂ adsorption isotherms of Cu(I)-SSZ-13 at different temperatures ...	83
Figure A.12. Experimental H ₂ adsorption data on Cu(I)-SSZ-13 at 278.6 K, 295.9 K and 304 K, fitted Sips adsorption (continuous line) and linear models (dashed lines)	84
Figure A.13. ln(P) versus 1/T of Cu(I)-SSZ-13 at quantity adsorbed = 0.020 mmol H ₂ g ⁻¹	84

LIST OF SYMBOLS

SYMBOLS

b	Affinity constant, $mmHg^{-1/n}$
K_{eq}	Adsorption equilibrium constant, $mmHg^{-1}$
P	Pressure, $mmHg$
Q_e	Equilibrium solid phase concentration, $mmol g^{-1}$
Q_{max}	Maximum adsorption capacity, $mmol g^{-1}$
Q_{st}	Isosteric heat of adsorption, $kJ mol^{-1}$
R	Ideal gas constant ($8.314 \cdot 10^{-3}$), $kJ K^{-1} mol^{-1}$
T	Temperature, K
V	Specific Volume, $cm^3 g^{-1}$
ΔH	Heat of reaction, $kJ mol^{-1}$
ΔH_{ads}	Adsorption enthalpy, $kJ mol^{-1}$
λ	Wavelength, \AA
$1/n$	Exponent

CHAPTER 1

INTRODUCTION

The growing population of the world effects the energy demand exponentially; thus, today's the most used energy sources, which are fossil fuels and natural gas, become inadequate. Moreover, fossil fuel and natural gas are not suitable to meet the energy need since these sources will eventually be depleted. Even if they are infinitely available, their combustion and end products are not environmentally benign such as CO₂, a common greenhouse gas.[1] Carbon dioxide levels reached up to 408 ppm by 2018.[2] This problem urges scientists to find more appropriate and renewable energy sources. In this manner, hydrogen is a prominent candidate to avoid the situation.

In this project, Cu(I)-exchange zeolites are prepared in order to develop lightweight, safe and economic onboard H₂ storage systems reaching 5.5 wt. % target storage capacity values at ambient temperature. Mesoporous zeolites are synthesized to increase the H₂ storage capacity at elevated pressures since H₂ uptake capacity of microporous zeolites are limited (2.6 wt. %) due to the total micropore volumes of zeolites that are smaller than metal organic frameworks. In this thesis, in Chapter 1, H₂ as an energy carrier, its production techniques, utilization in fuel cells, current H₂ storage systems and recent results are discussed in detail. In the second chapter, experimental methods of synthesis of zeolites, Cu(I)-exchange, characterization tests and H₂ adsorption tests are explained. In Chapter 3, characterization and H₂ adsorption results and discussion is given in two parts; i) ZSM-5 H₂ adsorption and adsorption calorimetry results and ii) SSZ-13, SSZ-39 & US-Y H₂ adsorption and isosteric heat of H₂ adsorption results

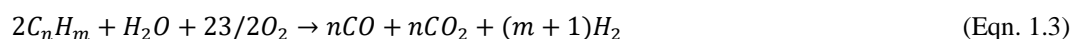
1.1. Hydrogen; the Fuel of Future

Hydrogen is a non-toxic, clean and renewable fuel when its production method is also renewable such as wind power or photovoltaic-electrolysis [1][3]. Hydrogen is a promising alternative to fossil fuels since it has the highest energy content by weight that is 3 times higher than gasoline or any other hydro-carbon fuel (142 MJ kg⁻¹ vs. 47 MJ kg⁻¹). Its only end-product is water vapor, and there is no leaking or pooling worries [1][4][5]. One disadvantage of hydrogen is its low energy content by volume, that is 4 times lower than gasoline [4].

1.1.1. Production of Hydrogen

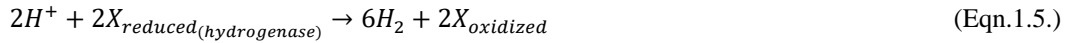
Hydrogen molecule is not a direct primary energy source; it is actually an energy carrier. Free hydrogen is not found naturally; it needs to be produced from other primary energy sources [6].

Hydrogen can be produced by various techniques from conventional sources and renewable energy sources. Today, the most often used hydrogen production techniques are i) steam reforming of natural gas and fossil fuels, which occurs in two-step reaction given in Equation (1.1) and (1.2), ii) partial oxidation of hydrocarbons that are heavier than naphtha in Equation (1.3), and iii) coal gasification, whose chemical reaction equation is given in Equation (1.4) below.



Moreover, hydrogen can also be produced from renewable energy sources such as biological sources, wind power, thermolysis of water, electrolysis of water, solar photovoltaic power for direct conversion via photolysis and photovoltaic-electrolysis system [6]. To emphasize, hydrogen energy is said to be renewable only if hydrogen is produced from one of the renewable energy sources explained below.

Among the biological sources, cyanobacteria and microalgae, which do not contain sulphur, manage to produce hydrogen in a bioreactor with the enzyme named hydrogenase, whose efficiency is reported in the range of 10–20% [1][7]. The equation is given below.

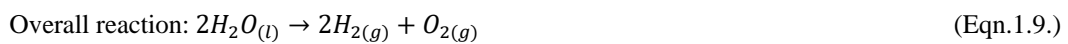
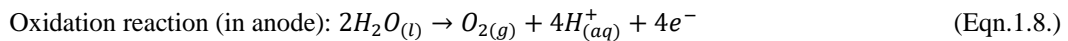
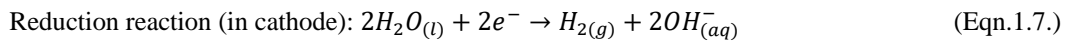


Wind energy is another renewable source to produce hydrogen. In this production method, wind energy is used to produce electrical energy, which will be used in electrolysis of water to generate hydrogen [8].

Thermolysis of water is breaking water molecules' covalent bonds into oxygen and hydrogen by using heat, and thermolysis reaction is given in Equation 1.6 [1][9].



Electrolysis of water is another way to generate hydrogen by splitting molecules of water into pure oxygen and hydrogen via reduction and oxidation reactions given below [10][11].



1.2. Usage of Hydrogen Energy

Hydrogen has diverse applications; it can be used as fuel to generate energy in fuel cells (as shown in Figure 1.1) and in chemical reactions mainly in methanol and ammonia production (see Equation (1.10-12) and Equation (1.13), respectively) [12].

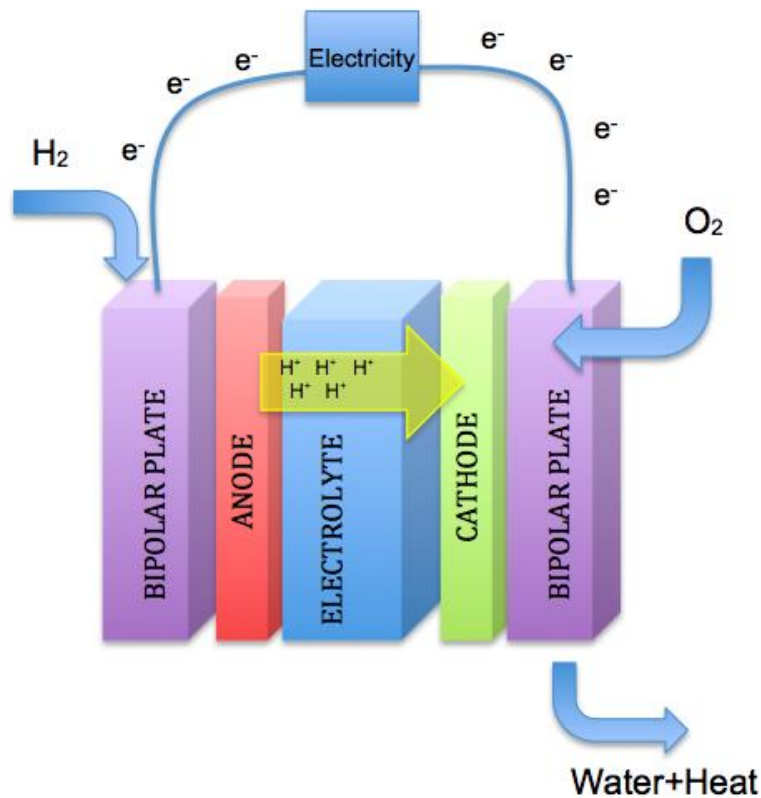
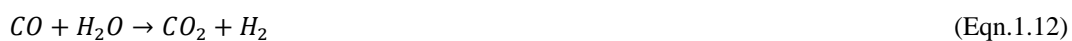


Figure 1.1. Schematic of a single fuel-cell



1.3. Advantages and Disadvantages of Hydrogen Energy

Hydrogen gas usage is appropriate in terms of environmental issues because it is a non-toxic and clean energy source. Once produced, hydrogen is a clean synthetic fuel because the only end product is water vapor; in other words, it only releases water vapor into the atmosphere when it reacts with oxygen. Hydrogen disperses quickly into the air; thus, there are not any pooling or spilling issues. Moreover, its energy

content by weight is very high around 142 MJ, which is three times more than gasoline, whose gravimetric energy density is around 47 MJ. [4][13] Hydrogen energy is much more efficient (60%) when compared with diesel (45%) and gasoline (22%) which advances the efficiency for future energy usage [12]. Thus, usage of hydrogen energy is appealing to be implemented fuel cell power technology in transportation, portable and stationary purposes [14].

However, the volumetric energy density of hydrogen gas is relatively low around 10 MJ L⁻¹ (in liquid state), which is around four times lower than gasoline [1][4]. Therefore, so as to keep hydrogen more energy dense, advanced storage methods are required.

1.4. Storage of Hydrogen Gas/Energy

Many researches have been conducted to improve hydrogen gas storage considering volume, weight, cost, consistency and safety so that it can be used in fuel cell technology (as shown in Figure 1) to produce energy mainly for transportation, stationary and portable purposes. In addition to mentioned concerns, designers also need to take the release rate of the hydrogen gas from the storage systems and the reversibility of the uptake and release into consideration [15]. In today's technology, hydrogen gas can be stored as compressed hydrogen, liquefied hydrogen, by chemisorption and physisorption. When storage materials are used, it is adsorbed in ionic or molecular form on the main material surfaces by using temperature, pressure and electro-chemical potential.

1.4.1. Compressed Hydrogen

Conventionally, hydrogen gas can be stored as compressed hydrogen in its pure form in tanks whose pressure ranges are commonly 200 to 350 bar, although there are systems with at least 700 bar capacity [16]. As the pressure of the hydrogen gas is increased, volumetric energy density is also rising. Even though this method is seems to be beneficial for energy purposes because storing in a smaller space by retaining its

energy effectiveness is simple, it is not safe to implement such a highly pressurized tanks in stationary or portable energy units [1][13].

1.4.2. Liquified Hydrogen

Liquid hydrogen is a concentrated form, which can be obtained at around 20 K and it is colorless and non-corrosive. Hydrogen liquefaction requires greater densities (around 0.070 kg L^{-1}) than the compressed hydrogen (around 0.030 kg L^{-1}); moreover, this method requires specialized infrastructure and instruments as the liquefaction procedure and the packing practices are energy intensive [1][16]. Even though this technique seems to be volumetrically and gravimetrically efficient, further research needs to be conducted to solve the problems about high rate of hydrogen liquefaction which may cause large amount of energy loss. Furthermore, to maintain the cryogenic temperature, additional refrigeration units are required; which increases the weight of the equipment and the total energy costs, and decreasing the overall energy content around 40% [17].

1.4.3. Chemisorption

Chemical adsorption, which is also named as chemisorption, is chemical binding of hydrogen atoms to the storage medium. According to the IUPAC (International Union of Pure and Applied Chemistry), strong interaction, also chemical bond formation, between the adsorbate and adsorbent in a monolayer on the exterior surface is named as chemisorption [14][18]. The stability of the chemisorption depends highly on the temperature and pressure.

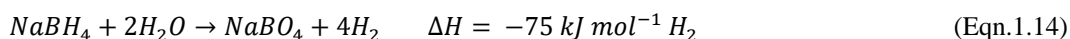
Chemisorption may preferably be reversible (reaching 7 wt. % H_2 storage [19]); however, in some cases it may be irreversible depending on the activation energy values of desorption. With high activation energies, it requires higher temperatures for desorption (400 –600 K). Moreover, chemisorption on complex hydrides (e.g. Mg_2NiH_4) is susceptible to their impurities, costlier and may possess lower reversible gravimetric capacity [1].

Among the Mg- and Li-based hydrates, MgH₂ has the highest reversible H₂ uptake capacity of 7.3 wt.% [20]; hence, they can be the potential candidate for mobile storage. On the other hand, their adsorption and desorption kinetics are very slow and also desorption of hydrogen requires high temperatures up to 573 K, so that their efficiency is decreasing and the applicability in transportation becomes unfavorable [17]. Moreover, chemisorption on intermetallic compounds cannot be said to be promising candidate for mobile applications, as they do not meet the requirements set by DOE with very low hydrogen storage capacities lower than 2 wt.% [17][21].

Table 1.1. Chemisorption materials and H₂ storage capacities

Material	Adsorption Temperature (K)	Pressure (bar)	H₂ Uptake (wt.%)	Ref.
NaBH ₄ (55 gr of NaBH ₄ per 100 g H ₂ O)	293		6.7	[22][23]
MgH ₂	573	8.4	7.00	[24]
MgH ₂ - 1 at% Al	453	0.6	7.30	[20]
Li ₂ NH	255-285	10	6.5	[25]
LiBH ₄ - 1/2MgH ₂ - 2 mol%	315-450	4.5-19	10	[26]
La _{0.59} Ce _{0.29} Pr _{0.03} Ni ₄ Co _{0.45}	0-100	50	1.40	[21]
Mn _{0.45} Al _{0.3}	0-100	50	1.44	[21]

Among metal hydrides, NaBH₄ (sodium borohydride) had great attention over the past decade. In 1953, it was firstly reported by Schlesinger et al. that NaBH₄ releases hydrogen and forms NaBO₂ (sodium metaborate) as a by-product when it goes hydrolysis in its highly stable aqueous solution. According to the reaction equation given below, with the presence of heterogeneous catalyst, the release of hydrogen is easy to control [19] [20].



According to the reaction given above, when fully hydrolyzed, the reaction gives 10.8 wt.% of hydrogen uptake capacity [29].

1.4.4. Physisorption

Physical adsorption (or named as physisorption) is the process where hydrogen can be stored in its molecular form on the surface of the adsorbent, which is mainly a solid porous material. Physical adsorption is a reversible process because there is no activation energy involved and the interaction energies are relatively low. Moreover, in this process adsorbate gas can be adsorbed and desorbed during several cycles without corrosion of the adsorbent solid or unintentional loss of the adsorbate gas [16].

The main advantage of physisorption is the fast adsorption/desorption kinetics; moreover, there is not a major change in the electronic structure of both adsorbent and adsorbate. Physisorption can occur by multilayer adsorption, whereas chemisorption occurs only monolayer depending on the temperature and pressure of the system [15].

Hydrogen molecules can be physically adsorbed on the surface of the materials such as porous carbons, zeolites and metal organic frameworks (MOF). In this storage method, the pore volume and surface area are the two main factors affecting the hydrogen storage capacity. Moreover, physisorption of hydrogen on porous particles is basically the result of weak van der Waals interactions between the surface of the adsorbents and hydrogen molecules. However, the weak van der Waals interactions are the main limitation of usage of these adsorbents as hydrogen storage materials; thus, physical adsorption of these adsorbent materials has higher storage capacities at higher pressures and relatively low (even cryogenic) temperatures. On the other hand, at ambient conditions (relatively low pressure and ambient temperature) these capacities are very low [14][15][16].

The main challenge of storing hydrogen using physisorption on nanoporous materials at desired conditions; i.e., ambient conditions (<100 bar and room temperature), is the weak interaction of H₂ and the adsorbate, which is not high enough to meet the targets set by the United States Department of Energy (DOE). The target data set by DOE are listed in Table 1.2 [1][30][31]. Moreover, the vehicles should be designed to store 5-

6 kg of hydrogen and manage to cover a distance of up to 350 mile with a full of fuel charge [1].

Table 1.2. *Technical targets for on-board hydrogen storage systems reported by DOE*

Storage Parameter	2005	2010	2015	2017
Usable specific energy from H ₂ (kg H ₂ kg ⁻¹)	0.045	0.060	0.090	0.055
Usable energy density from H ₂ (kg H ₂ L ⁻¹)	0.036	0.045	0.081	0.040

1.4.4.1. Porous Carbons

Hydrogen adsorption on the porous carbon materials occur through van der Waals bonding, whose binding energy is relatively low which is around 6 kJ mol⁻¹[1]. Carbon foam, carbon nanotubes, carbon aerogels and activated carbon are some carbon structures with high surface area, which show very low energy density by volume [1]. Wang et al. reported that among porous activated carbons, AC-K5 shows the highest gravimetric hydrogen uptake capacity of 7.08 wt.% at 77 K and 20 bar with a high surface area of up to 3190 m² g⁻¹ [32]. Furthermore, the research conducted by Jordá-Beneyto points out two porous carbon materials, KUA5 and KUA6. Hydrogen uptake capacity of KUA 5 is 6.8 wt.% at 77 K and 50 bar; whereas, that of KUA 6 reaches to 8 wt.% at 77 K and 40 bar with the highest surface area among all other porous carbon materials studied in this research [33]. Chen et al. reported in their study that Li-doped and K-doped multi-walled nanotubes (MWNTs) show a hydrogen uptake capacity of 20 wt.% and 14 wt.%, respectively [34]. K-doped multi-walled nanotubes are chemically unstable, whereas Li-doped ones are chemically stable, but they require very high temperatures (473 to 673 K) for adsorption and desorption of hydrogen [34].

1.4.4.2. Metal Organic Frameworks (MOFs)

Metal organic frameworks, which are also named as porous coordination polymers (PCPs), are a class of crystalline nanoporous particles composed of metal ions connected with organic ligands so that the composition generates pores smaller than 2 nm. They received great interest due to their compositional diversity. Researches have many studies to explore the combining of MOF with other functional materials so as to obtain substances with advanced chemical and physical properties due to the structural diversity feature of MOFs [35][36][37][38]. They are also famous for their ultra-high porosity, reaching to 90% free volume, and high internal surface areas, which extends $10,000 \text{ m}^2 \text{ g}^{-1}$ of a Langmuir surface area [38][39]. By considering these unique functional properties, metal organic frameworks are used in separation and storage [35], proton conduction [40], sensing [41] and drug delivery [42]. MOFs generally show micro-porous characters whose pore sizes can change from several angstroms up to several nanometers [37].

Metal organic frameworks are promising candidates for hydrogen storage applications due to their high surface areas and porosity. In addition, some metal organic frameworks show high hydrogen storage capacities, higher than 7 wt.%, at 77 K and high pressures [14][43]. On the other hand, their hydrogen uptake capacities are very low, less than 1 wt.%, at ambient conditions due to the interaction energies between the hydrogen and the framework, which are around $3\text{-}10 \text{ kJ mol}^{-1}$ [43]. Farha et al. reported the highest hydrogen uptake capacity (excess capacity) is 9.95 wt.% at 77 K and 56 bar in NU-100 (NU = North-western University) with total capacity of 16.4 wt.% at 77 K and 77 bar [44]. Moreover, in MOF-210 the highest hydrogen uptake capacity is reported as 8.5 wt.% at 77 K and 80 bar. Moreover, MOF-200 and MOF-205 also have larger hydrogen storage capacity which are 7 wt.% and 6.5 wt.% at 77 K, respectively, as reported by Furukawa et al. [39][45]. Maximum hydrogen storage capacity in MOF-5 is reported as 7.1 wt.% at 77 K and 40 bar, which has total capacities of 10 wt.% at 77 K and 100 bar, and 11.5 wt.% at 77 K and 180 bar [46][14]. Furthermore, MOF-74 and IRMOF-11 shows hydrogen saturation at 26 bar and 34 bar around 2.3 wt.% and 3.5 wt.%, whereas MOF-177 and IRMOF-20 reach saturation at

70 and 80 bar with hydrogen uptakes of 7.5 wt.% and 6.7 wt.%, respectively [43]. In 2010, Tedds et al. reported that IRMOF-1 have the absolute hydrogen uptake capacity at 15 bar around 4.86 wt.% and 1.80 wt.% at 77 and 117 K, respectively [15]

Table 1.3. Surface area, H₂ uptake capacity and enthalpy of H₂ adsorption data of metal organic frameworks

Material	Surface Area (m ² g ⁻¹)	Temperature (K)	Pressure (bar)	H ₂ Uptake (wt.%)	ΔH (kJ mol ⁻¹)	Ref.
PCN-10	1407	30	3.5	6.84	6.8	[47]
Cu(dcectp)(NO ₃)	268	77	1	1.34	6.12	[48]
Cu(dcectp)(NO ₃)	268	77	20	1.91	6.12	[48]
SNU-21H	695	77	1	1.64	6.09	[49]
SNU-21H	695	77	70	4.36	6.09	[49]
SNU-21S	905	77	1	1.95	6.65	[49]
MOF-74	1132	77	26	2.3	-	[4][43]
Cu ₂ (BDC) ₂ (dabco)	1461	77	1	1.8	-	[50]
Cu ₂ (BDC) ₂ (dabco)	1461	77	33.7	2.7	-	[51]
Cu (peip)	1560	77	1	2.51	6.63	[52]
Cu (peip)	1560	77	40	4.14	6.63	[52]
MN(BTT)	2100	77	90	6.9	10.1	[53]
HKUST-1	2175	77	10	3.6	6.8	[53]
IRMOF-11	2180	77	34	3.5		[43][4]
SNU-50'	2300	77	1	2.1	7.2	[54]
SNU-50'	2300	77	60	5.53	7.2	[54]
Cu ₂ (BDDC)	2357	77	0.95	1.64	-	[55]
Cu ₂ (BDDC)	2357	77	17	3.98	-	[55]
MIL-100	2800	77	26	3.28	6.3	[53]
NOTT-111	2930	77	1	2.56	6.21	[56]
NOTT-110	2960	77	1	2.64	5.68	[56]
MOF-5	4170	77	48	5.2	4.8	[53]
MOF-5	4170	77	180	11.5	4.8	[14][57]
MOF-205	4460	77	80	6.5		[45][39]
MOF-177	4500	77	70	7.5	4.4	[43][45]

1.4.4.3. Zeolites

Zeolites are highly crystalline aluminosilicate structured porous nanomaterials, which can be defined by a network of interconnected cavities and pores. They are known for their adjustable compositions and high stability [57][58]. Zeolites are composed of tetrahedrally coordinated aluminum oxide (AlO_4) and silicon oxide (SiO_4) units that are interlinked with a formula given in Equation (1.15.). Notation ‘M’ in the equation (1.15) stands for the positive ions, that counterbalances the negative charge on the aluminosilicate framework [58].



For many decades, zeolites are commercially used in catalytic reactions and gas separation. Thanks to developing technology on solid-state hydrogen storage, zeolites are considered as potential candidates for hydrogen storage because of their adjustable pores and channels by performing ion-exchange to modify the size of the exchangeable cations and the valence state [57][59].

Generally, pore sizes of the zeolites are smaller than 1 nanometer, which constricts hydrogen molecules into the pore of the zeolite with the help of the van der Waals forces. In previous studies, zeolites were reported to store gravimetrically small amounts of hydrogen, which is smaller than 0.3 wt.% at ambient conditions [59][60][61] or either temperatures higher than 473 K [59][61]. On the other hand, if they are loaded at cryogenic temperatures, gravimetric storage amounts reach higher than 1 wt.% [59][62]. To illustrate, Annemieke et al. reported that maximum hydrogen uptake capacity of zeolites is found in the range of 2.6 to 2.9 wt.% [4][63]. In addition to the adsorption capacities, Otero Arian et. al. [64]–[67] examined adsorption enthalpies of alkali metal, alkaline earth metal exchanged zeolites (see Table 1.4).

Table 1.4. Heat of adsorption values of alkali and earth alkali metal containing zeolites

Zeolites	ΔH (kJ mol⁻¹)	Reference
Li-ZSM-5	6.5	[65]
Na-ZSM-5	10.3	[66]
K-ZSM-5	9.1	[67]
(Mg,Na)-Y	18.2	[64]
Ca-Y	11	[68]
Mg-X	15	[69]

As seen from Table 1.4, adsorption enthalpies of the zeolites containing alkali and earth alkali metals are relatively low, with maximum value of 18 kJ mol⁻¹ (Mg,Na)-Y, when compared with that of the zeolites containing Cu(I)-ion whose heat of adsorption values are reported by Georgiev et al. to be in the range of 39 – 73 kJ mol⁻¹ [63]. These low heat of adsorption values are the explanation for the low hydrogen uptake capacities of the zeolites containing alkali and earth-alkali given in Table 1.5.

Table 1.5. H_2 uptake capacity and enthalpy of H_2 adsorption data of alkali metal and alkaline earth metal-exchanged zeolites

Material	Surface Area ($\text{cm}^3 \text{g}^{-1}$)	Temperature (K)	Pressure (bar)	H_2 uptake (wt.%)	ΔH (kJ mol^{-1})	Ref.
NaA	-	77	15	1.54	-	[59]
H-SAPO-34	547	77	0.92	1.09	-	[70]
H-SSZ-13 (Si/Al=11.6)	638	77	0.92	1.28	-	[71]
NaX	662	77	15	1.79		[59]
CaX	669	77	15	2.19		[57]
NaY	725	77	15	1.81	18.2	[59][64]
NaY	725	77	0.57	0.37	18.2	[62][64]
H-ZSM-5	-	77	0.80	0.24		[72]
H-ZSM5	-	77	0.67	0.72		[72]
(Si/Al = 16)						[73]
H-Y	-	77	0.95	0.56		[74]
NaY	-	77	15	1.81		[59]
NaY	853	295	100	0.45		[75]
NaA	-	298	10	0.11		[60]
NaA	-	298	700	1.2		[76]

1.4.4.4. Cu-exchanged Zeolites

Cu-exchanged zeolites have many applications; hence, they are the most studied transition metal exchanged zeolites. After Iwamoto et al. reported that NO decomposition activity on Cu-Y [77] and Cu-ZSM-5 [78] during 80's, the interest on Cu-exchanged zeolites have increased. Cu-exchanged zeolites are studied in the treatment of oxygen-rich exhaust gas from diesel engines, they show superior activity and selectivity at selective catalytic reduction (SCR) [79], are used in catalytic reactions such as hydroxylation of benzene to phenol [80], selective oxidation of methane [81] and carbonylation of alcohols [82].

In addition to these mentioned catalytic reactions, Cu(I)-exchanged zeolites show remarkable H₂ adsorption and storage capacities at room temperature [63]. Cu(I)-exchanged zeolites adsorb hydrogen with higher binding energies among all the adsorbents (39-73 kJ mol⁻¹, Cu(I)-ZSM-5 [63]) at the ambient conditions because Cu(I) sites in the zeolite ZSM-5 shows unusual ability to bind hydrogen [83][84].

In addition to the Cu(I)-ZSM-5, Solans-Monfort et al. theoretically calculated the binding energy between hydrogen and Cu(I)-adsorption sites on SSZ-13 to be between 13 to 56 kJ mol⁻¹ [85]. Moreover, Ipek et. al. reported in their study that the isosteric adsorption enthalpies of Cu(I)-SSZ-13 and Cu(I)-[B]-ZSM-5 are found in the range of 18 – 56 kJ mol⁻¹ at temperatures between 293 and 323 K [86]. Consequently, it can be said that these high heat of adsorption values are promising for high hydrogen storage capacities on Cu(I)-exchanged zeolites.

In 2013, Kozyra et al. reported theoretical analysis of ion transfer between different parts of three components system, which are hydrogen, copper and a generalized ligand (a zeolite) to examine the activation of hydrogen and adsorption on cationic sites in zeolites. The electron donation from σ (H-H) to 4s (Cu), back-donation from 3d _{π} (for Cu) to σ^* (H-H) anti-bonding orbital and electron transfer into the bonding region between hydrogen and positive ion are analyzed by ETS-NOCV method. Kozyra et al. proved the improved interaction between H₂ and Cu(I)-site on zeolite framework by showing the improved electron back donation to hydrogen molecule antibonding orbital when compared with free cations. To conclude, Cu(I) sites in zeolites are especially good adsorber and activators for hydrogen molecule [83].

Cu-exchange Methods:

Conventionally, Cu-exchange is often performed using aqueous solutions of Cu(II) salts (Cu(SO₄)₂, Cu(NO₃)₂, Cu(aca)₂, Cu(acac)₂) [87][88][89], which often results in Cu(II)/Al ratios not exceeding 0.5. However, increased concentration of Cu(II) or Cu(I) centers on zeolites are crucial in determining the catalytic activity and storage capacities. Therefore, Cu(I)-exchange on zeolites are often preferred.

Solid [90][91] and vapor-phase [92][93][94] exchange of Cu(I)Cl salts can result in Cu(I)/Al ratios reaching to 1, in which, vapor-phase or solid-phase CuCl reacts with the H⁺-on the zeolite to give Cu(I)-zeolite and HCl vapor as products. One major drawback of these methods is the residual chlorine on the zeolite pores reaching Cl/Al 0.58 [90], which decreases available catalytic/adsorption area. Thus, a Cl-free method needs to be developed with Cu/Al ratios as high as possible.

In this project, we have developed a new Cu(I)-exchange method in liquid media to ensure homogeneous distribution of bare Cu(I)-cations in the zeolite pores and to achieve Cl-free Cu(I)-exchanged zeolites. For this reason, we used CuCl/acetonitrile solutions as Cu(I)-exchange media. We investigated the effect of different CuCl concentrations and degree of dehydration of the starting zeolite on the extent of Cu(I)-exchange and Cl amounts on prepared zeolites.

1.4.4.5. Mesoporous Materials

The reported hydrogen uptake capacities do not depend only on the framework type of the nanoporous materials and the electrochemical interactions between the ions but also on the specific pore sizes of the adsorbents [71][58]. In previous research conducted by Frost et al., the effects of surface area, heat of adsorption and free volume on hydrogen storage are investigated with different pressure ranges with same surface chemistry and framework topology, but varying pore sizes. Their results show that there are three different types of adsorption regimes; 1-low pressure loading (bar), where hydrogen storage correlates with the adsorption enthalpy; 2- intermediate pressure loading (bar), where storage correlates with surface area; 3- high pressure loading, where storage correlates with free volume. Therefore, especially at the low-pressure region, or equivalently at room temperature conditions, heat of H₂ adsorption is critical in determining the maximum H₂ storage capacity. However, as the pressure is increased, the open adsorption centers such as the metal cations on zeolites or MOFs will be saturated with H₂ and the interaction of the H₂ molecule with the adsorbent pores through van der Waals forces will become more important. For maximizing

these interactions, it is reported that the narrow pore size distribution of the adsorbents below 1-2 nm promotes H₂ adsorption [95]. In this regard, zeolites having uniform pore sizes below 1 nm are potential adsorbents especially at medium pressure range (1–30 bar).

At higher pressure ranges (> 30 bar), the total pore volume of the adsorbent will play an important role on the H₂ adsorption capacity. Vitillo et al. reported the theoretical H₂ storage capacities of zeolites depending on their micropore volumes [58]. According to their calculation results, maximum H₂ storage capacity by zeolites can be at best 2.86 wt. % [58] due to the maximum micropore volume of 0.338 cm³ g⁻¹ on FAU (Zeolite X or Y). In order to achieve higher H₂ storage capacities (to be able to reach target values of 5.5 wt. %), pore volume of the zeolites should be increased by modification of the zeolite structure such as mesopore additions. By this way, one can use both the optimal micropore sizes of zeolites (smaller than 1 nm) that enhances the van der Waals forces and also the extra mesopore volume that would increase the potential H₂ storage capacities especially at increased pressures.

Mesopore addition into zeolites can be achieved using either top-down or bottom-up methods. In top-down methods, zeolites are synthesized using an additional mesoporegen (such as CTABr) in the gel mixture to create pores in the range of 2–50 nm [96]. In bottom-up methods, synthesized microporous zeolites are treated in acid or alkaline solutions to dealuminate or desilicate the sample to create pores > 2 nm in the structure [97].

CHAPTER 2

EXPERIMENTAL PROCEDURE

Experimental procedure includes synthesis of the zeolites [B]-ZSM-5, [Al]-ZSM-5, mesoporous [B]-ZSM-5, SSZ-13 and SSZ-39, ion-exchange of these zeolites, characterization procedures and hydrogen tests.

2.1. Synthesis of the Zeolites

[B]-ZSM-5

[B]-ZSM-5 is synthesized hydrothermally following the procedure reported by Sanhoob et al. [98] with a gel formula of $1.0\text{SiO}_2:0.1\text{TPAOH}:35.5\text{H}_2\text{O}:0.1\text{B}(\text{OH})_3:0.10\text{NaOH}$. 0.163 g of sodium hydroxide (Merck; 99.5 wt. %) is dissolved in 21.14 mL de-ionized water, followed by adding 2.07 g of tetrapropylammonium hydroxide (TPAOH, Merck, 40 wt. % solution in water). After that, 6.12 g of SiO_2 (Sigma-Aldrich, Ludox HS-40, colloidal silica, 40 wt. % suspension in water) is added to the mixture. After a homogeneous mixture is achieved, 0.51 g H_3BO_3 (Merck, 99.5 wt. %) is added. The mixture is stirred at 550 rpm at ambient conditions for 2 hours. Hydrothermal synthesis is carried at 453 K for 3 days using autoclaves with 35 mL Teflon containers. After that, the product is cooled and it is recovered by vacuum filtration and washed with deionized water. Zeolite is then calcined at 823 K for 5 hours (using a heating rate of 2 K min^{-1}).

[Al]-ZSM-5

[Al]-ZSM-5 is synthesized by a hydrothermal method reported by Zhang et al. [99] Firstly, 0.1 g of sodium aluminate (Reidel De Haen, 44% Na_2O , 55% Al_2O_3 , 1% H_2O , NaAlO_2) and 1.2 g of sodium hydroxide (Merck, 99%, NaOH) are dissolved in 202.5 mL of H_2O and stirred for 12 hours. Afterwards, 12.85 g of tetraethyl orthosilicate

(Merck, 98%, TEOS) is added drop-wise under agitation. Then 4.2 g of tetrapropylammonium bromide (Merck; 99 wt.%, TPABr) are added and stirred for additional 12 hours. The mixture is transferred into Teflon lined autoclaves and heated at 448 K for 3 days. Then the solid is separated, washed with distilled water, dried at 373 K and calcined at 823 K (using a heating rate of 1 K min⁻¹) for 5 hours.

Mesoporous [B]-ZSM-5

Mesoporous boron ZSM-5 is synthesized by using a mixture with the molar composition of 1.0SiO₂:0.064H₃BO₃:0.13Na₂O:0.14HDA:0.1CTABr:60H₂O. Firstly, NaOH and H₃BO₃ [96] are dissolved in distilled water. Then, CTABr (Sigma Aldrich, 98 wt.%) and HDA (Sigma Aldrich, 98 wt.%) are added and dissolved. After that fumed silica is added. After obtained mixture is stirred for 6 hours, it is transferred into a Teflon lined autoclave and heated at 423 K for 14 days. The product is recovered by vacuum filtration and washing, dried in air, and calcined at 853 K (heating rate of 1 K min⁻¹) for 10 hours.

[Al]-SSZ-13

SSZ-13/12 is synthesized using a gel mixture has a molar composition of SiO₂:Al₂O₃:TMAdaOH:H₂O of 1:0.035:0.5:20, respectively. Firstly, 0.681 gram of aluminum triethoxide (Sigma Aldrich, 97 wt.%), 2.264 gram of de-ionized water and 24.864 gram *N,N,N*-trimethyl-1-adamantanonium hydroxide solution (Luzhou Dazhou, TMAdaOH, 25 wt.%) are stirred at 323 K for 0.5 hour to dissolve all the aluminum ethoxide. At 323 K, 12.504 gram of tetraethyl orthosilicate (Merck, 98 wt.%) is added to the solution and stirred. The gel-like solution is transferred to Teflon-lined autoclaves and synthesized hydrothermally heated at 423 K for 14 days. The hydrothermally produced crystals are recovered using vacuum filtration and washed with 500 mL de-ionized water. The as-made zeolite is then calcined at 853 K (heating rate of 1 K min⁻¹) for 6 hours.

[Al]-SSZ-39

[Al]-SSZ-39 is synthesized hydrothermally using the gel formula having a molar composition of SiO₂: Al₂O₃:SDA:Na₂O:H₂O of 1:0.02:0.19:0.25:22.3 respectively. Firstly, 23.415 g of tetramethyl piperidinium hydroxide (Sachem, Inc., 35.3 wt.%), which is the structure-directing agent (SDA), is mixed with 61.845 g of de-ionized water. After that, 44.940 gram of sodium silicate solution (Merck, 28 wt.% SiO₂, 9 wt.% Na₂O) and 3.591 gram of 1 M NaOH solution are added and stirred for 15 minutes at room conditions. After a homogeneous solution is obtained, 4.490 g NH₄-US-Y (Alfa Aesar, Zeolite Y, Si/Al=12) is added slowly to the mixture and the stirring continued for half an hour. The synthesis gel is then transferred to Teflon-lined autoclaves and hydrothermally treated at 323 K for 7 days under rotation at 45 rpm. The resulting crystals are then recovered using vacuum filtration and washed with 500 mL of de-ionized water. The zeolite is calcined at 833 K (with 1 K min⁻¹) for 8 hours to remove organic content and structure directing agents from the zeolite pores.

Ultra-stable-Y

Ultra-stable-Y is supplied commercially in ammonium form from Alfa Aesar (45869) with the silicon to aluminum ratio (Si/Al) of 6.

Mesoporous [Al]-SSZ-39 and US-Y

Microporous [Al]-SSZ-39 is synthesized by using the procedure given above. US-Y is supplied from Alfa Aesar. In order to create mesopores, dealumination procedure reported by Leng et al. [97] is followed. The dealumination procedure is mainly composed of three steps. Firstly, proton form of the zeolite is refluxed with 2 M HNO₃ solution (with the ratio of 20 mL solution per gram of zeolite) at 373 K for 2 hours. After filtration, washed sample is calcined at 823 K for 5 hours. Second step is to treat the sample with 0.2 M of NaOH (again with the ratio of 20 mL solution per gram of zeolite) at 343 K for half an hour. Finally, the resulting part is refluxed with 0.2 M of HNO₃ solution at 323 K for 1.5 hour. The final sample is exchanged with ammonium nitrate (see section 2.2.1.).

2.2. Ion-Exchange Procedure

2.2.1. Ammonium-Exchange

NH_4^+ -zeolites are obtained by exchanging 1 g of calcined zeolite in 500 mL of 0.2 M of NH_4NO_3 (Sigma Aldrich, 99 wt.%) aqueous solution (500 mL de-ionized water and 8 g of NH_4NO_3). The solution is stirred for 3 hours at a temperature of 353 K for ion-exchange, and then the zeolite is filtered, washed with de-ionized water and dried. This exchange procedure is repeated three times. Finally, NH_4^+ -zeolites are heat treated at 823 K for 5 hours with a heating rate of 2 K min^{-1} to obtain H^+ -form of the zeolites.

2.2.2. Copper(I)-Exchange

Pretreatment

CuCl (Sigma-Aldrich, 97 wt. %) is placed into oven at 353 K for 6 hours so as to eliminate water content. H^+ -zeolite is heated at 423 K under vacuum conditions for 6 hours in order to eliminate the water vapor in the zeolite pores.

Exchange

Cu(I) -exchange is performed in different molarity of CuCl -acetonitrile solutions. Acetonitrile (Reidel De Haen) is flushed with N_2 (Oksan, 99.99%) before mixing, so that oxygen molecules dissolved in the liquid are eliminated. After that, heated CuCl is dissolved in the acetonitrile by using magnetic stirrer. After homogeneity is obtained, 1 gram of H^+ -zeolite is added to the solution. When the homogeneity is obtained, the system is flushed with N_2 for 10 minutes to keep the system under inert conditions, then the N_2 flow is stopped and the solution is stirred for 6 hours at room temperature. After 6 hours, the mixture is filtered using polytetrafluoroethylene filter papers, washed with acetonitrile and dried at 385 K for 2 hours. Cu(I) -exchanged zeolite is calcined at 723 K for 3 hours with a heating rate of 2 K min^{-1} to remove acetonitrile.

2.3. Characterization Tests

The prepared and Cu(I)-exchanged samples are characterized using powder X-ray diffraction (XRD), inductively coupled plasma-optical emission spectrometry (ICP-OES), N₂ adsorption at 77 K and scanning electron microscopy (SEM).

The XRD analysis is performed using an X-ray diffractometer (Rigaku Ultima-IV, equipped with Cu K α radiation, $\lambda=1.5418$ Å, 40 kV, 30 mA, Central Laboratory, METU) with a scanning speed of 1° min⁻¹.

The ICP-OES analysis is performed using Perkin Elmer Optima 4300DV analyzer (Central Laboratory, METU). The samples are dissolved using a HF-HNO₃ mixture before ICP analysis.

The N₂ adsorption experiments at 77 K are performed at Chemical Engineering Department, METU using a surface area and pore volume analyzer (Micromeritics Tristar II 3020). The degassing process prior to the N₂ adsorption experiment was performed using Micromeritics VacPrep by heating the sample to 573 K for 6 hours under vacuum conditions before filling the sample with N₂ (Oksan, 99.999%). The N₂ adsorption/desorption experiment is performed using P/P₀ values of N₂ (Oksan, 99.999%) between 10⁻⁵ to 1 after measuring the free cell volume by using He gas (Oksan, 99.999%). The temperature of the sample cell is maintained at 77 K using liquid N₂.

The SEM analysis of the samples are performed using an electron microscope (QUANTA 400F Field Emission SEM, Central Laboratory, METU) with an accelerating voltage of 20 kV. The Energy-Dispersive X-ray Spectroscopy analysis is also performed using the same accelerating voltage.

2.4. Hydrogen Tests

Hydrogen tests are performed in two different systems, which are a Tian-Calvet type adsorption calorimetry device and an automated physisorption device (Micromeritics Tristar II 3020).

2.4.1. Adsorption Calorimetry Tests

H₂ adsorption tests on adsorption calorimetry are performed in two steps, which are vacuum pretreatment and H₂ adsorption experiments, where differential heat of adsorption values are calculated using a Seteram C80 Tian-Calvet Calorimeter [96].

2.4.1.1. Vacuum Pretreatment

The sample after O₂ treatment at 723 K is placed into the sample cell and evacuated using a turbo molecular pump at 523 K for 12 hours to desorb all the adsorbates from the zeolite pores. The system is cooled to 323 K and the dead volume is measured using Helium. The sample is degassed at 323 K for 2 more hours after dead volume measurement.

2.4.1.2. Hydrogen Adsorption Experiments

The adsorption experiments are performed at 323 K by introducing 0.033 bar to 0.533 bar of H₂ gas (Oksan, 99.99 wt.%) into the sorption chamber incrementally. The differential heats of adsorption for each dosing are calculated using the software of the calorimeter.

2.4.2. Hydrogen Tests in Physisorption Device

Hydrogen adsorption tests in an automated physisorption device (Micromeritics Tristar II 3020) are performed also in two steps, which are degas treatment and H₂ adsorption tests.

2.4.2.1. Degas Pretreatment

Samples are placed into the sample cells and evacuated at 623 K for 6 hours under vacuum using a degassing instrument (Micromeritics, VacPrep 061) so as to remove all the adsorbates from the zeolite pores. After the degas is complete, the cells are

cooled to room temperature and filled with N₂ gas (Oksan, 99.999%) before it is carried to the main instrument (Micromeritics Tristar II 3020) for H₂ analysis.

2.4.2.2. Hydrogen Adsorption Test

Degassed zeolites are placed to the physisorption device (Micromeritics Tristar II 3020). Firstly, the cells are evacuated for 30 minutes and filled with Helium so as to measure the dead volume. After evacuation for 2 more hours, hydrogen gas (Oksan, 99.999%) is introduced to the sample cell incrementally from 0.013 bar up to 1.067 bar. The adsorption isotherm data are collected from the software of the Micrometric device. The hydrogen adsorption tests on Micromeritics device are performed at 77 K, 278 K, 293 K and 303 K to calculate the differential heat of adsorption by using Clasius-Clapeyron equation (Equation 2.1).

$$\ln\left(\frac{P_2}{P_1}\right) = \frac{-\Delta H_{ads}}{R} \left(\frac{1}{T_2} - \frac{1}{T_1}\right) \quad (\text{Eqn.2.1})$$

CHAPTER 3

RESULTS AND DISCUSSION

Results consist two parts, i) adsorption calorimetry for ZSM-5 samples and ii) physisorption for SSZ-13, SSZ-39 and US-Y samples, which shows H₂ adsorption isotherms obtained on adsorption calorimetry and on physisorption apparatus respectively.

3.1. ZSM-5 Results

Hydrogen adsorption tests on Cu(I)-[Al]-ZSM-5, Cu(I)-[B]-ZSM-5 and mesoporous Cu(I)-ZSM-5 are conducted using a Seteram C80 Tian-Calvet Calorimeter [100], whose experimental procedure is explained in Section 2.3.1.

3.1.1. Characterization Results

3.1.1.1. XRD

Firstly, the crystallinity of the synthesized zeolites are analyzed using X-ray diffraction method. As seen in Figure 3.1, all of the synthesized zeolites shows high crystallinity with characteristic peaks for MFI structure. In addition, Figure 3.2 shows the XRD pattern of the zeolites [Al]-ZSM-5 and [B]-ZSM-5 before and after the Cu(I)-exchange. It can be clearly seen that there is no change in the characteristic peaks for MFI. Therefore, there is no crystallinity loss upon Cu(I)-exchange.

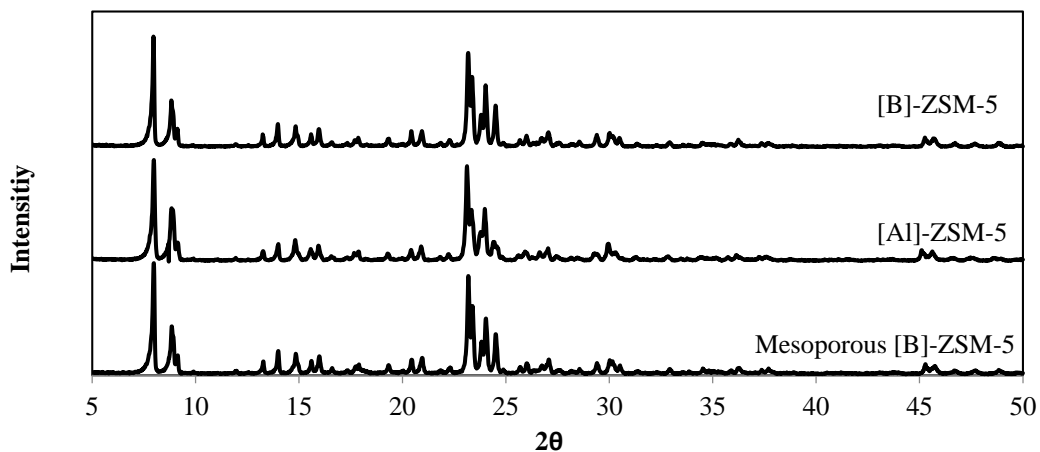


Figure 3.1. XRD patterns of [B]-ZSM-5, [Al]-ZSM-5 and mesoporous [B]-ZSM-5 (wavelength= 0.15418 nm)

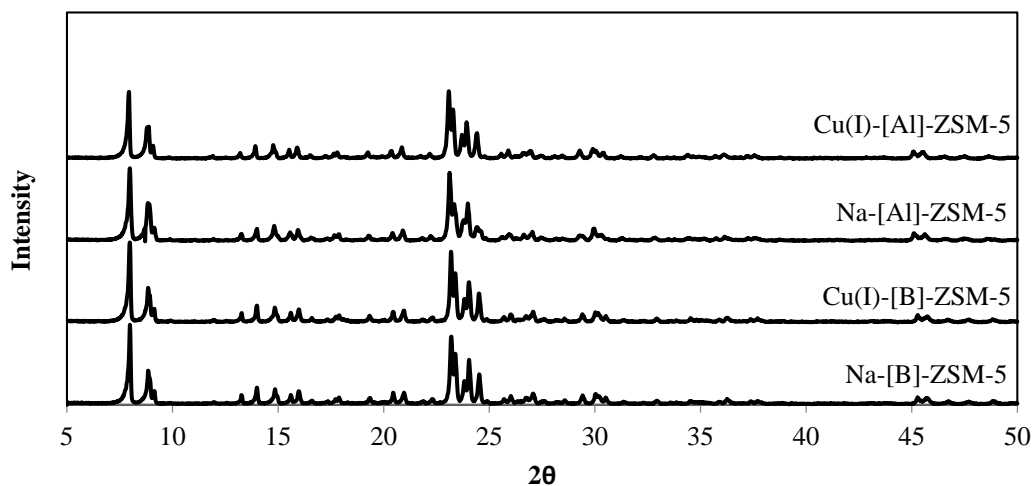


Figure 3.2. XRD patterns of [B]-ZSM-5 and [Al]-ZSM-5 in Na and Cu form (wavelength=0.15418 nm)

3.1.1.2. SEM Images

To see the morphologies and the particles sizes of the zeolites, SEM micrographs are observed in Figure 3.3. [Al]-ZSM-5 and [B]-ZSM-5 have typical coffin-shaped uniform ZSM-5 crystals with particles sizes between 2 and 5 μm . Mesoporous [B]-ZSM-5 crystals have bigger crystal size of 10 μm , which are composed of attached small crystals.

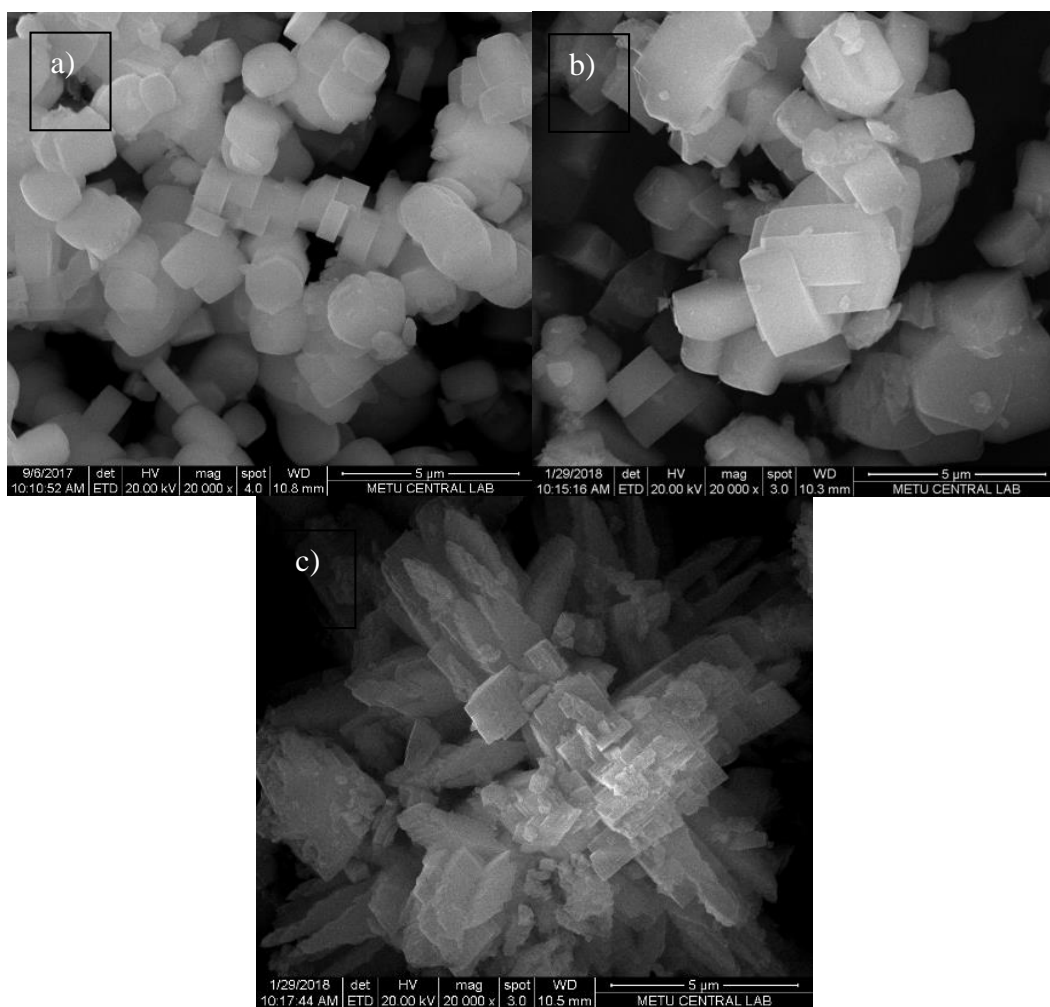


Figure 3.3. SEM images of zeolites; a) Cu(I)-[B]-ZSM-5, b) Cu(I)-[Al]-ZSM-5, c) mesoporous Cu(I)-[B]-ZSM-5

3.1.1.3. Elemental Analysis

The results of Cu(I)-exchange of [Al]-ZSM-5, [B]-ZSM-5 and mesoporous [B]-ZSM-5 in 0.01 M CuCl/acetonitrile solution show Cu/B and Cu/Al ratios reaching up to 0.78 (Table 3.1). Cu/B ratios for Cu(I)-[B]-ZSM-5 and mesoporous Cu(I)-[B]-ZSM-5 obtained by ICP-EOS and EDX methods are 0.51 versus 0.66 and 0.79 versus 0.78, respectively. These similar results refer that Cu(I)-exchange of the zeolites are achieved to be homogeneous since EDX method is a surface characterization method,

whereas ICP-EOS gives averaged elemental analysis. Moreover, Cl/B or Cl/Al ratios are found lower than 0.1 mol % with the EDX method as seen in Table 3.1.

Si/Al and Si/B ratios for Cu(I)-[Al]-ZSM-5, Cu(I)-[B]-ZSM-5 and mesoporous Cu(I)-[B]-ZSM-5 are found as 43, 55 and 101, respectively. Due to limited B incorporation in the framework, achieved Si/B ratio on [B]-ZSM-5 is very high. For this reason, [Al]-ZSM-5 is also synthesized to give similar Si/Al ratio.

Higher Cu/B ratio of 0.78 is observed on mesoporous Cu(I)-[B]-ZSM-5, when compared to the Cu/B ratio of 0.66 on Cu(I)-[B]-ZSM-5, which might indicate easier diffusion of Cu(I)-ions into the zeolite pores at the same conditions.

Table 3.1. *Elemental analysis of Cu(I)-[Al]-ZSM-5, Cu(I)-[B]-ZSM-5 and mesoporous Cu(I)-[B]-ZSM-5 exchanged in 0.01 M CuCl-acetonitrile solution.*

Sample	Si/Al*	Si/B	Cu/Al*	Cu/B	Cl/Al* or Cl/B	Cu conc. (μmol/g)
	(EDX)	(ICP-EOS)	(EDX)	(ICP-EOS)		
Cu(I)-[Al]-ZSM-5	43±3	-	0.55±0.12	-	0.05±0.05	221
Cu(I)-[B]-ZSM-5	-	55		0.66±0.04	0.12±0.04	196
Cu(I)-[B]-ZSM-5 (mesoporous)	-	101		0.78±0.08	0.08±0.08	127

*: Elemental analysis was obtained by EDX at 20 keV.

Cu(I)-exchange is performed in different CuCl/acetonitrile concentrations of 0.01, 0.02 and 0.04 M on [B]-ZSM-5 in order to examine whether or not the Cu(I) concentration of the resulting zeolite could be increased. As seen from Table 3.2, Cu/B ratios obtained by EDX analysis are 0.66, 1.41 and 2.37 for 0.01, 0.02 and 0.04 M of CuCl/acetonitrile solution, whereas these ratios obtained by ICP-EOS are 0.51, 0.92 and 1.82, respectively. Increasing CuCl concentration in acetonitrile solution causes an increase of Cu(I) concentration of the zeolites; on the other hand, Cl contents are also increased. Starting CuCl concentrations of 0.02 and 0.04 M in acetonitrile result in Cl/B ratios of 0.43 and 0.73, respectively. The difference between the Cu/B ratios

obtained by the ICP-EOS and EDX analysis and the increasing Cl-content show that Cu(I)-exchange cannot be performed homogeneously in 0.02 and 0.04 M of CuCl/acetonitrile solutions and CuCl dissolution is insufficient especially in 0.02 and 0.04 M concentrations.

In order to eliminate the resulting Cl content of the zeolite, the pretreatment conditions are changed. Instead of drying the zeolite in the conventional oven at 423 K for 6 hours, the H⁺-form of the zeolite is dehydrated under vacuum conditions at 523 K for 12 hours; so that, all the water content, which can cause inhomogeneous Cu(I)-exchange, is eliminated from the zeolite pores before the Cu(I)-exchange. As seen from Table 3.2, Cl/B ratio for Cu(I)-[B]-ZSM-5 with the new pretreatment method decreased from 0.43 to 0.08 with reasonable Cu/B ratios of 1.05.

Table 3.2. Cu-exchange results of [B]-ZSM-5 in different molarity of CuCl/acetonitrile solutions.

Concentration of CuCl/acetonitrile solution (M)	Si/B*	Cu/B (EDX)**	Cu/B(ICP-EOS)	Cl/B (EDX)
0.01	54.7	0.66±0.04	0.51	0.12±0.04
0.02	54.7	1.41±0.24	0.92	0.43±0.14
0.02***	54.7	1.05±0.42	-	0.08±0.05
0.04	54.7	2.37±0.18	1.82	0.73±0.08

*: Elemental analysis of B was obtained from ICP-EOS method.

** : EDX analysis was obtained at 20 keV.

***: New pretreatment method (drying 12 hours at 523 K under vacuum conditions) is performed.

3.1.1.4. Pore Volume Characterization

Micropore and mesopore volumes of the zeolites are given in Table 3.3. Micropore volumes of the zeolites are found by t-plot method using N₂ adsorption data at 77 K (see Figure A.1-3). [Al]-ZSM-5 and [B]-ZSM-5 have micropore volumes of 0.134 and 0.126 cm³ g⁻¹, respectively, which are in the typical MFI framework micropore volume range. Moreover, they also seem to have negligible mesopore volumes of 0.020 and 0.052 cm³ g⁻¹, respectively. Mesoporous [B]-ZSM-5 has lower micropore volume of 0.100 cm³ g⁻¹ and relatively higher mesopore volume of 0.095 cm³ g⁻¹. These pore

volume characterization data show that mesopores are successfully formed in [B]-ZSM-5 using CTABr as structure directing agent.

Table 3.3. Micro- and meso-pore volumes of [Al]-ZSM-5, [B]-ZSM-5 and mesoporous [B]-ZSM-5 before and after Cu(I)-exchange.

Sample	$V_{\text{micro}} (\text{cm}^3 \text{g}^{-1})^*$	$V_{\text{meso}} (\text{cm}^3 \text{g}^{-1})^{**}$
[Al]-ZSM-5	0.134	0.020
Cu(I)-[Al]-ZSM-5	0.123	0.063
[B]-ZSM-5	0.126	0.052
Cu(I)-[B]-ZSM-5	0.121	0.057
[B]-ZSM-5 (meso)	0.100	0.095
Cu(I)-[B]-ZSM-5 (meso)	0.111	0.142

*: Micropore volumes are obtained using t-plot method from N_2 adsorption data at 77 K.

** : Mesopore volume is obtained by subtracting the micropore volume from the single point pore volume (total volume) obtained at $P/P_0=0.98$.

3.1.2. Adsorption Calorimetry Results

Adsorption isotherms and the differential heat of adsorption data are obtained using a Seteram C-80 Tian-Calvet adsorption calorimeter at 323 K [101].

3.1.2.1. Adsorption Isotherms

Figure 3.4 shows that Cu(I)-[Al]-ZSM-5, Cu(I)-[B]-ZSM-5 and mesoporous Cu(I)-[B]-ZSM-5 have similar H_2 uptake capacities per gram of zeolite. On the other hand, in Figure 3.5, mesoporous Cu(I)-[B]-ZSM-5 has higher H_2 uptake capacity on $\text{H}_2 \text{ Cu}^{-1}$ basis (0.99, at 290 mmHg) compared with Cu(I)-[Al]-ZSM-5 (0.69 at 290 mmHg) and Cu(I)-[B]-ZSM-5 (0.56 at 290 mmHg). These results show that there is a stronger interaction between H_2 molecules and Cu(I)-cations in mesoporous Cu(I)-[B]-ZSM-5.

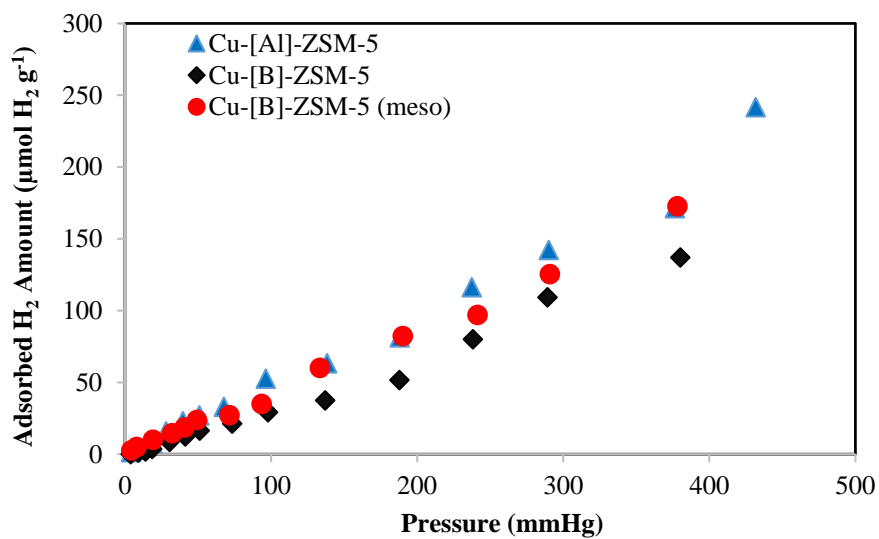


Figure 3.4. H₂ adsorption isotherms of Cu(I)-[Al]-ZSM-5, Cu(I)-[B]-ZSM-5 and mesoporous Cu(I)-[B]-ZSM-5 at 293 K

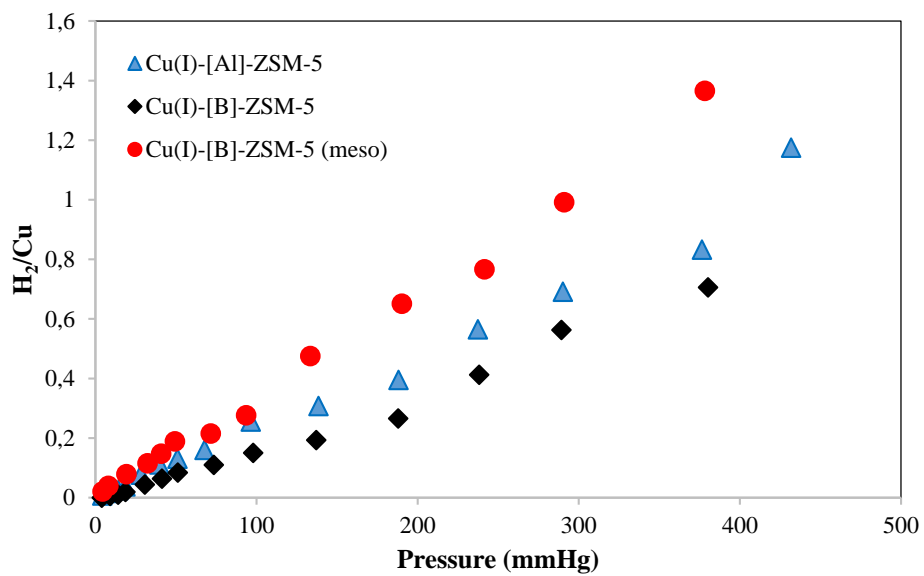


Figure 3.5. H₂ adsorption isotherms of Cu(I)-[Al]-ZSM-5, Cu(I)-[B]-ZSM-5 and mesoporous Cu(I)-[B]-ZSM-5 on a per Cu-basis at 293 K

3.1.2.2. Differential Heat of Adsorption

Differential heat of adsorption values are calculated using the software of Seteram C-80 Tian-Calvet adsorption calorimeter. Coverage dependent differential heat of adsorption values on Cu(I)-[Al]-ZSM-5, Cu(I)-[B]-ZSM-5 and mesoporous Cu(I)-[B]-ZSM-5 can be seen in Figure 3.6. Initial heat of adsorption data for Cu(I)-[Al]-ZSM-5, Cu(I)-[B]-ZSM-5 and meso-Cu(I)-[B]-ZSM-5 are 52, 95 and 76 kJ mol⁻¹, respectively. These experimental data are in agreement with the isosteric heat of adsorption data reported by Georgiev et al. between 73 and 39 kJ mol⁻¹ for Cu(I)-[Al]-ZSM-5 [63], and the theoretical binding energies of H₂ (87-64 kJ mol⁻¹) reported by Kozyra [98]. Differential heat of H₂ adsorption values for Cu(I)-[Al]-ZSM-5 and Cu(I)-[B]-ZSM-5 are around 30-10 kJ mol⁻¹ for H₂ Cu⁻¹ around 0.15. For higher H₂ Cu⁻¹ ratios, differential heat of adsorption values decreases to 8-5 kJ mol⁻¹.

Differential heat of adsorption values for mesoporous Cu(I)-[B]-ZSM-5 are higher for H₂ Cu⁻¹ ratios up to 0.15, which is consistent with higher H₂ uptake capacity of the zeolite in H₂ Cu⁻¹ basis (Figure 3.5).

Higher heats of H₂ adsorption are important for obtaining higher H₂ uptake capacities, but desorption of H₂ needs to be obtained at low temperatures. Optimal H₂ binding energies for zeolites are reported around 20-25 kJ mol⁻¹ [69]. Experimental data obtained are between 30 kJ mol⁻¹ and 10 kJ mol⁻¹ for H₂ Cu⁻¹ ratios between 0 and 0.15, which are very close to the reported optimum differential heat of adsorption values.

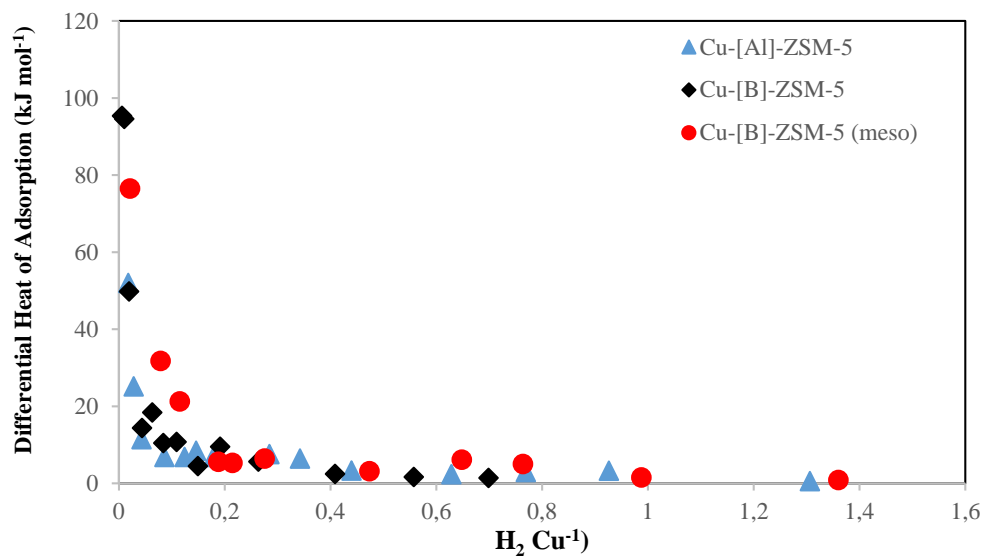


Figure 3.6. Differential heat of adsorption for Cu(I)-[Al]-ZSM-5, Cu(I)-[B]-ZSM-5 and mesoporous Cu(I)-[B]-ZSM-5 obtained at 323 K.

3.2. SSZ-13, SSZ-39, US-Y Results

3.2.1. Characterization Results

3.2.1.1. XRD

As done in the first part, X-Ray diffraction method is used to analyze the crystallinity of the synthesized zeolites; SSZ-13, SSZ-39, US-Y, acid-treated SSZ-39 and acid-treated US-Y. As seen in Figure 3.7-A, all of the zeolites show high crystallinity except for acid-treated US-Y. Acid-treated US-Y has no peaks which means the zeolite US-Y lost its crystallinity during the acid treatment; therefore, it is not used in further studies. Moreover, Figure 3.7-B also shows the XRD patterns of the zeolites after Cu(I)-exchange procedure, where it can be clearly seen that there is no change in the characteristic peaks. Thus, the zeolites do not lose any crystallinity upon Cu(I)-exchange procedure.

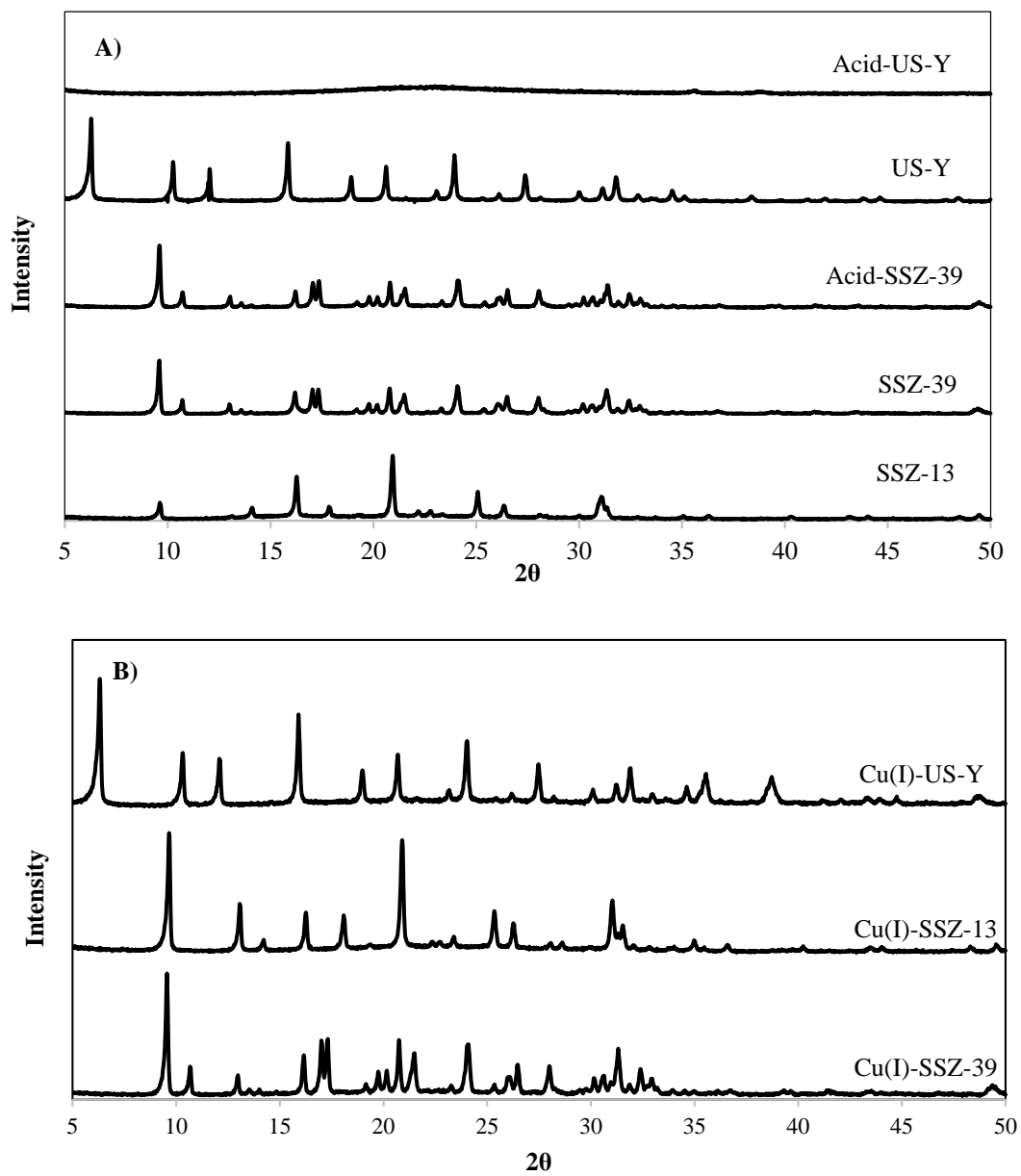


Figure 3.7. A) XRD patterns of SSZ-13, SSZ-39, acid-treated SSZ-39 (acid-SSZ-39), US-Y and acid-treated US-Y (acid-US-Y) B) Cu(I)-SSZ-13, Cu(I)-SSZ-39, Cu(I)-US-Y.

3.2.1.2. SEM Images

SEM micrographs of Cu(I)-exchanged zeolites are observed in order to determine the morphologies and the particle sizes. SSZ-13 crystals have crystal sizes around 1-2 μm (see Figure 3.8a), where smaller crystals are also observed on these 1-2 μm crystals that could form mesopores between the smaller crystals. SSZ-39 (see Figure 3.8b) has orthorhombic crystals with sizes also around 1-2 μm . US-Y has typical FAU crystal morphology (octahedrons and truncated octahedrons) also between 1 and 2 μm . In Figure 3.8-d, it can be seen that there are macropores on the surface of SSZ-39 crystals and also smaller-sized particles resulting from the acid treatment.

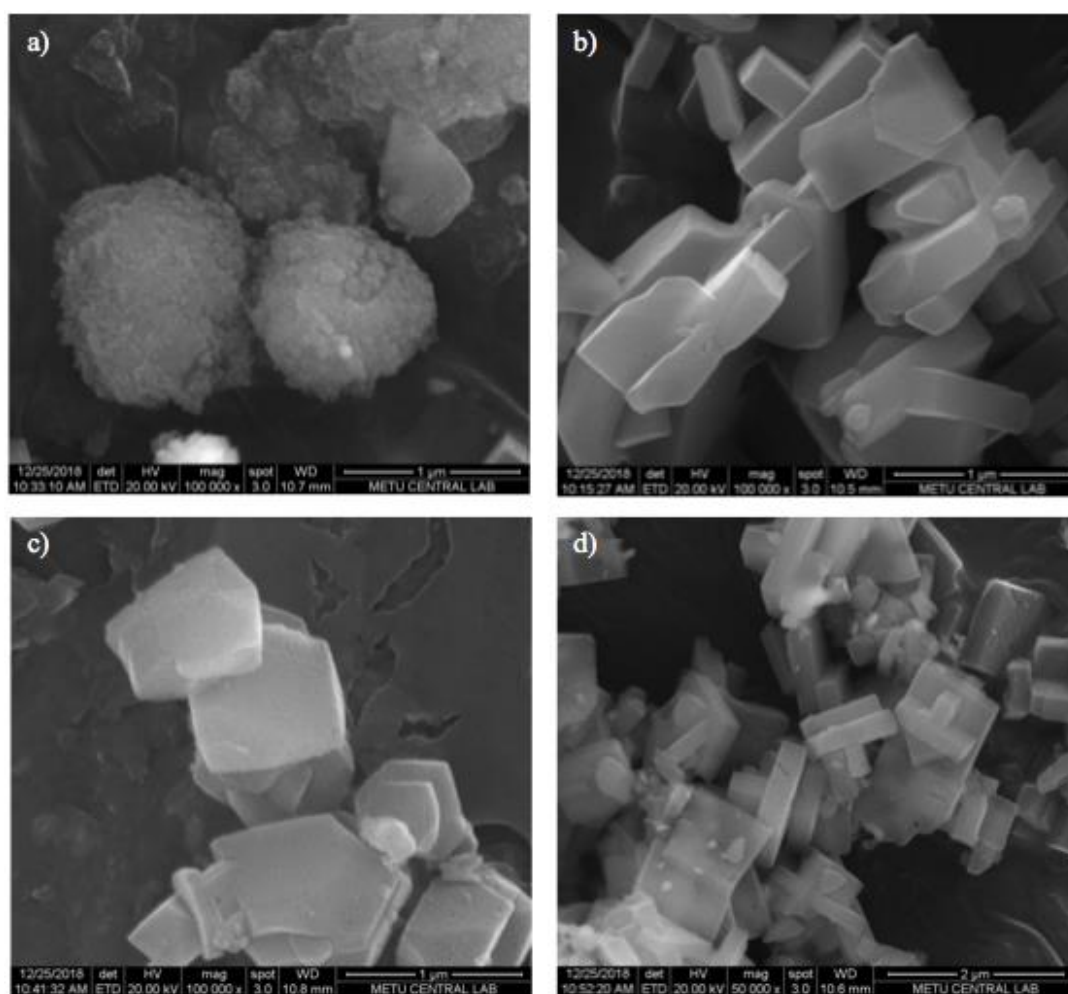


Figure 3.8. SEM images of zeolites a) Cu(I)-SSZ-13, b) Cu(I)-SSZ-39, c) Cu(I)-US-Y, d) acid-treated Cu(I)-SSZ-39.

3.2.1.3. Elemental Analysis

Elemental analysis of zeolites Cu(I)-SSZ-13, Cu(I)-SSZ-39, Cu(I)-US-Y and acid-treated Cu(I)-SSZ-39 with varying starting CuCl/acetonitrile concentration and exchange durations are given in Table 3.4 (elemental analysis performed by EDX and ICP-EOS methods). For each zeolite, increased concentration of CuCl in acetonitrile and increased exchange duration increase the observed Cu/Al ratios and Cu concentrations obtained by both EDX and ICP-EOS methods. Increasing molarity of CuCl/acetonitrile solution from 0.01 M to 0.02 M does not affect the Cu/Al ratio and Cu concentrations as expected for six hour of exchange duration. On the other hand, increasing exchange duration from 6 hours to 18 hours affects Cu/Al ratios and Cu concentrations more than the increasing CuCl concentration in acetonitrile. The reason of this situation might be the lower Si/Al ratios of the zeolites (higher Al content when compared to ZSM-5 samples). Zeolite having higher Si/Al ratios (ZSM-5) do not require extended exchange duration to obtain higher Cu/Al ratios and Cu concentrations (see section 3.1.1.3). When Cu(I)-exchange conditions are changed from 0.01 M CuCl/acetonitrile concentration and 6 hours of exchange duration to 0.04 M CuCl/acetonitrile concentration and 18 hours of exchange duration, Cu/Al ratio of Cu(I)-SSZ-13 increased from 0.27 to 1.08, obtained from ICP-EOS analysis (from 0.34 to 0.89 by EDX method). Moreover, Cu concentration of Cu(I)-SSZ-13 increases from 0.450 to 1.450 mmol g⁻¹.

For Cu(I)-SSZ-39, Cu/Al ratios obtained by ICP-EOS and EDX are 0.34 and 0.57, respectively. The difference between the results obtained by ICP-EOS and EDX might refer that Cu(I)-exchange of SSZ-39 cannot be achieved to be homogeneously.

Si/Al ratios of acid-treated Cu(I)-SSZ-39 (acid-Cu(I)-SSZ-39) are slightly higher when compared with those of Cu(I)-SSZ-39 given in Table 3.4, indicating dealumination of the zeolite. Cu/Al ratio and Cu concentration of acid-treated Cu(I)-SSZ-39 are obtained as high as 0.73 and 1.424 mmol g⁻¹, respectively.

Commercially supplied US-Y has Si/Al ratio around 5, which is expected for steam-treated (one of the dealumination methods) Zeolite-Y, whose Si/Al ratio is around 2.5. Cu/Al ratio of the acid-treated Cu(I)-US-Y are found as 1.06 and 0.84 (Cu(I)-exchange in 0.06 M CuCl/acetonitrile for 18 hour) obtained by ICP-EOS and EDX method, respectively.

Table 3.4. Elemental analysis of Cu(I)-SSZ-13, Cu(I)-SSZ-39, Cu(I)-US-Y and acid treated Cu(I)-SSZ-39 (acid-Cu(I)-SSZ-39) obtained by ICP-EOS and EDX methods.

Sample	Si/Al*	Cu/Al*	Si/Al**	Cu/Al**	Cl/Al**	Cu Concentration (mmol g ⁻¹)
Cu(I)-SSZ-13						
0.01 M, 6 h	8.8	0.27	10.7±0.6	0.34±0.09	0.02±0.02	0.450
0.02 M, 6 h	7.94	0.34	9.4±0.6	0.38±0.09	0.02±0.01	0.610
0.04 M, 18 h	10.29	1.08	9.4±0.4	0.89±0.08	0.02±0.02	1.450
Cu(I)-SSZ-39						
0.01 M, 6 h	5.71	0.3	7.4±0.2	0.32±0.04	0.01±0.01	0.713
0.02 M, 6 h	4.99	0.33	6.1±0.5	0.35±0.22	0.02±0.02	0.857
0.04 M, 18 h	6.52	0.34	8.1±0.5	0.57±0.02	0.00±0.00	0.727
Acid-Cu(I)-SSZ-39						
0.02 M, 6 h	6.57	0.35	7.1±0.1	0.31±0.03	0.08±0.02	0.736
0.04 M, 18 h	6.79	0.73	7.5±0.3	0.73±0.10	0.06±0.04	1.424
Cu(I)-US-Y						
0.01 M, 6 h	4.56	0.11	5.8±0.2	0.14±0.02	0.00±0.00	0.324
0.04 M, 6h	4.39	0.32	5.1±0.2	0.32±0.09	0.03±0.02	0.934
0.06 M, 18 h	5.43	1.06	5.5±0.1	0.84±0.07	0.02±0.02	2.344

*: Elemental analysis obtained by ICP/EOS method.

**: Elemental analysis is obtained by EDX at 20 keV.

3.2.1.4. Pore Volume Characterization

Micropore and mesopore volumes of the zeolites before and after Cu(I)-exchange are given in Figures 3.9-3.11 and Table 3.5. Micropore volumes are calculated applying statistical thickness method (t-plot) from N₂ adsorption data at 77 K. Total pore volume of the sample is calculated from the single point pore volume obtained at P/P₀=0.98. Mesopore volumes are calculated by subtracting micropore volumes from the total pore volumes.

H⁺-SSZ-13 has micropore and mesopore volumes of 0.226 and 0.736 cm³ g⁻¹, respectively, indicating significant mesoporosity. On the other hand, micropore and mesopore volumes of H⁺-SSZ-39 are 0.250 and 0.002 cm³ g⁻¹, respectively. Thus, H⁺-SSZ-39 is said to be a microporous zeolite. Acid treatment is performed on H⁺-SSZ-39 to obtain mesoporous zeolite by decreasing the alumina content of the zeolite crystals. When the micropore and mesopore values of the acid-treated H⁺-SSZ-39 (acid-H⁺-SSZ-39) are considered, it can be concluded that the treatment did not result in significant mesopore formation, but instead resulted in crystal size reduction as seen in Figure 3.8d. Small pores (3.8 Å) of SSZ-39 might have prevented the Al extraction from the framework, similar to SSZ-13 samples. Since the formed mesopore volumes were not as high as expected, the Cu(I)-exchanged acid-treated SSZ-39 is not further used for H₂ adsorption tests.

The pore volume analysis is also conducted on the commercially supplied US-Y, and micropore and mesopore volumes are 0.279 and 0.171 cm³ g⁻¹, respectively. These results show relatively small amount of mesopores in US-Y.

As seen from Table 3.5, micropore volume of the zeolites are decreased after Cu(I)-exchange (with a pronounced decrease after exchange with highly concentrated CuCl/acetonitrile solutions) indicating Cu(I) incorporation inside the micropores.

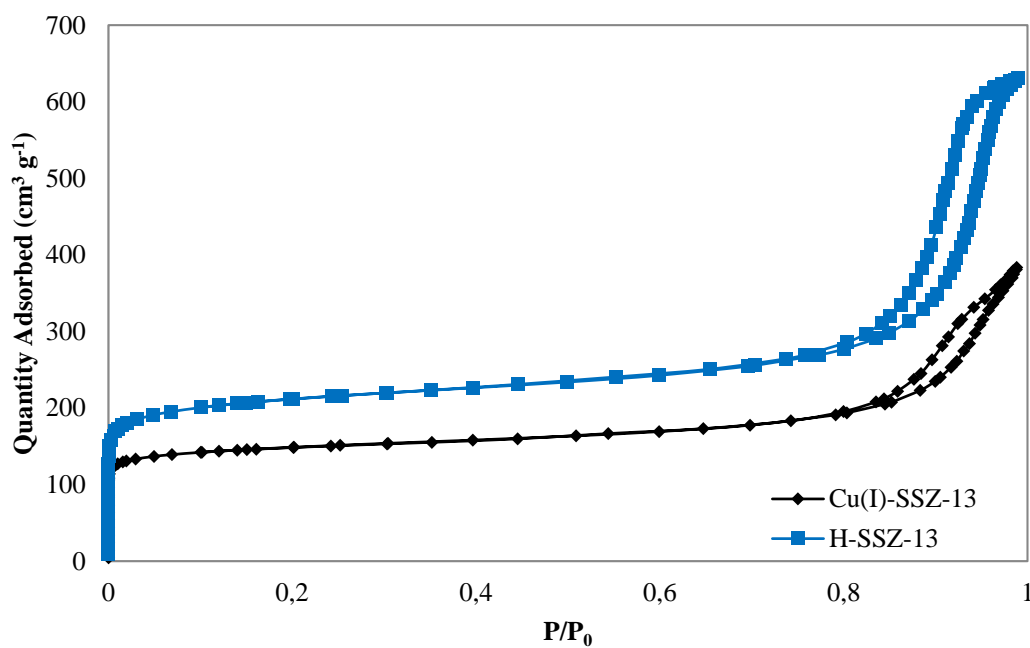


Figure 3.9: Nitrogen adsorption/desorption isotherm at 77 K for SSZ-13 before and after Cu(I)-exchange

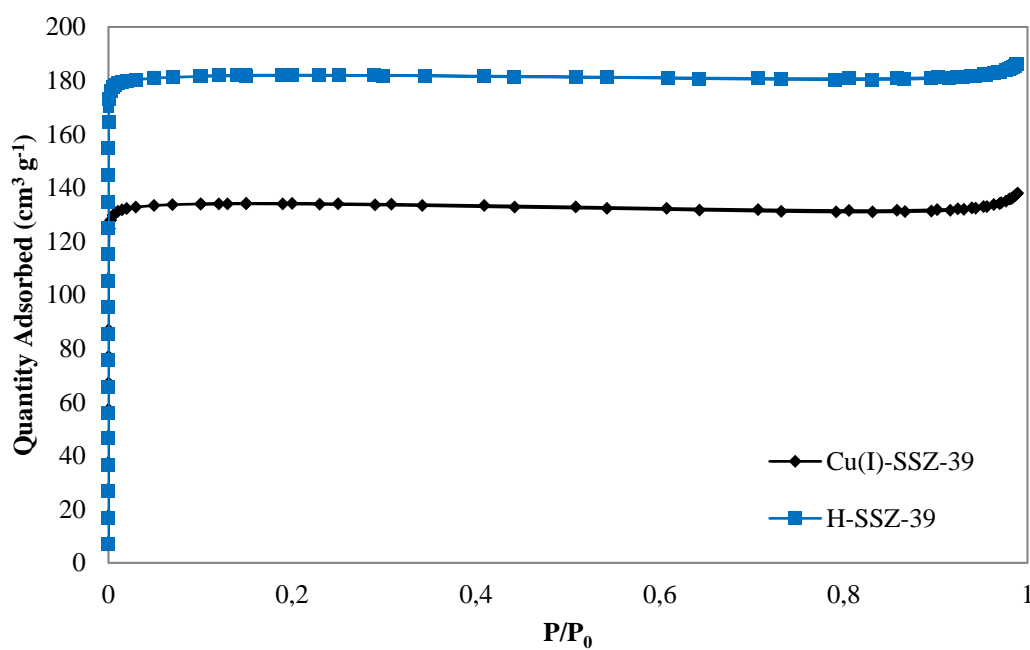


Figure 3.10: Nitrogen adsorption/desorption isotherm at 77 K for SSZ-39 before and after Cu(I)-exchange

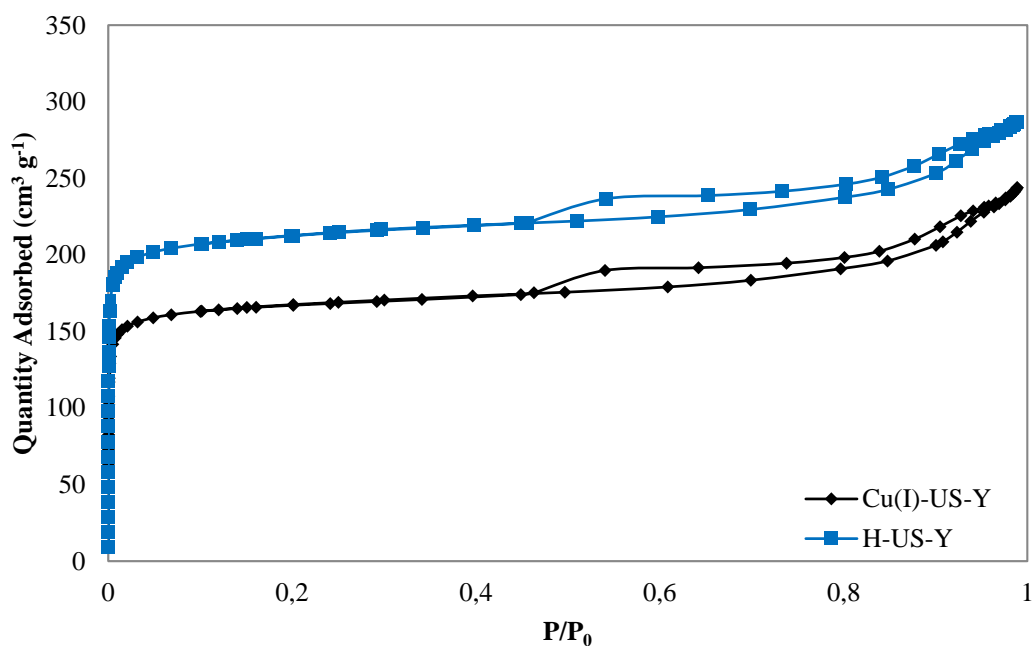


Figure 3.11: Nitrogen adsorption/desorption isotherm at 77 K for US-Y before and after Cu(I)-exchange.

Table 3.5. Pore volumes of zeolites; SSZ-13, SSZ-39, US-Y and acid-treated SSZ-39 (acid-SSZ-39) before and performing Cu(I)-exchange.

Sample	CuCl Concentration (M)	Exchange Duration (h)	V_{total} ($cm^3 g^{-1}$)	V_{micro}^* ($cm^3 g^{-1}$)	V_{meso}^{**} ($cm^3 g^{-1}$)
H ⁺ -SSZ-13	-	-	0.962	0.226	0.736
Cu(I)-SSZ-13	0.02	6	0.854	0.190	0.664
Cu(I)-SSZ-13	0.04	18	0.572	0.169	0.403
H ⁺ -SSZ-39	-	-	0.252	0.250	0.002
Cu(I)-SSZ-39	0.01	6	0.244	0.233	0.011
Cu(I)-SSZ-39	0.04	18	0.211	0.207	0.004
Acid-H ⁺ -SSZ-39	-	-	0.273	0.251	0.022
H ⁺ -US-Y	-	-	0.440	0.279	0.161
Cu(I)-US-Y	0.01	6	0.420	0.245	0.175
Cu(I)-US-Y	0.06	18	0.371	0.220	0.151

*: Micropore volumes are obtained using t-plot method from N₂ adsorption data at 77 K.

** : Mesopore volume is obtained by subtracting the micropore volume from the single point pore volume (total volume) obtained at P/P₀=0.98.

3.2.2. Hydrogen Adsorption Results

3.2.2.1. Adsorption Isotherms

Figure 3.12 and 3.13 shows the H₂ uptake capacity of Cu(I)-SSZ-13 (Cu/Al= 0.34, Cu(I)-exchange in 0.02 M CuCl/acetonitrile for 6 hours), -SSZ-39 (Cu/Al= 0.34, Cu(I)-exchange in 0.04 M CuCl/acetonitrile for 18 hours) and US-Y (Cu/Al= 1.06, Cu(I)-exchange in 0.06 M CuCl/acetonitrile for 18 hours) at room temperature (293 K).

At room temperature, H₂ uptake capacities are expected to be correlated to the H₂ binding energies since major binding sites are expected to be the Cu(I) -centers (H₂ Cu⁻¹ <1, see Figure 3.13). Therefore, the Cu(I)-sites on different zeolite frameworks are expected to result in different H₂ binding energies (which will be discussed later) and H₂ adsorption capacity values. According to Figure 3.12 and 3.13, Cu(I)-SSZ-39 shows the highest H₂ uptake capacity in both per gram of zeolite and per Cu indicating Cu(I)- sites that have potential high energy H₂ binding sites.

When Cu(I)-SSZ-13 is compared for H₂ uptake capacity on per gram of zeolite and per Cu, it showed lower H₂ adsorption capacity than Cu(I)-SSZ-39 indicating smaller H₂ binding energies.

Cu(I)-US-Y shows the lowest H₂ uptake capacity both per gram of zeolite and per Cu. Although the Cu(I)-concentrations is high, the framework of US-Y, which has Cu(I) sites mainly at the inaccessible 6-member rings (MR) [94], might prevent the high energy interaction of Cu(I)-sites with H₂, resulting in H₂ interaction with lower energy sites.

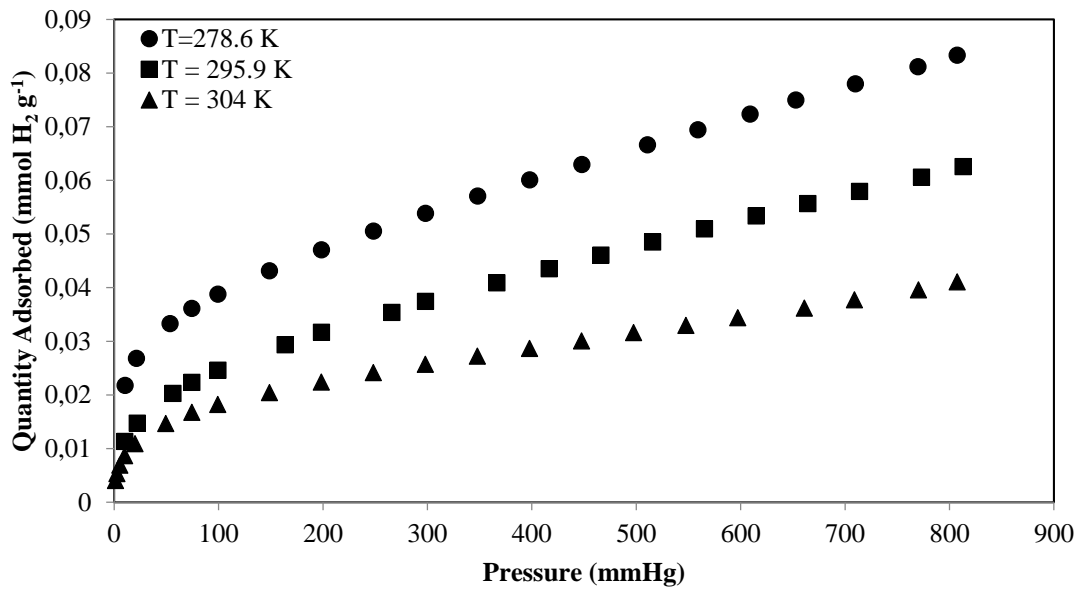


Figure 3.12. Adsorption isotherms of Cu(I)-SSZ-13, Cu(I)-SSZ-39 and Cu(I)-US-Y at 293 K.

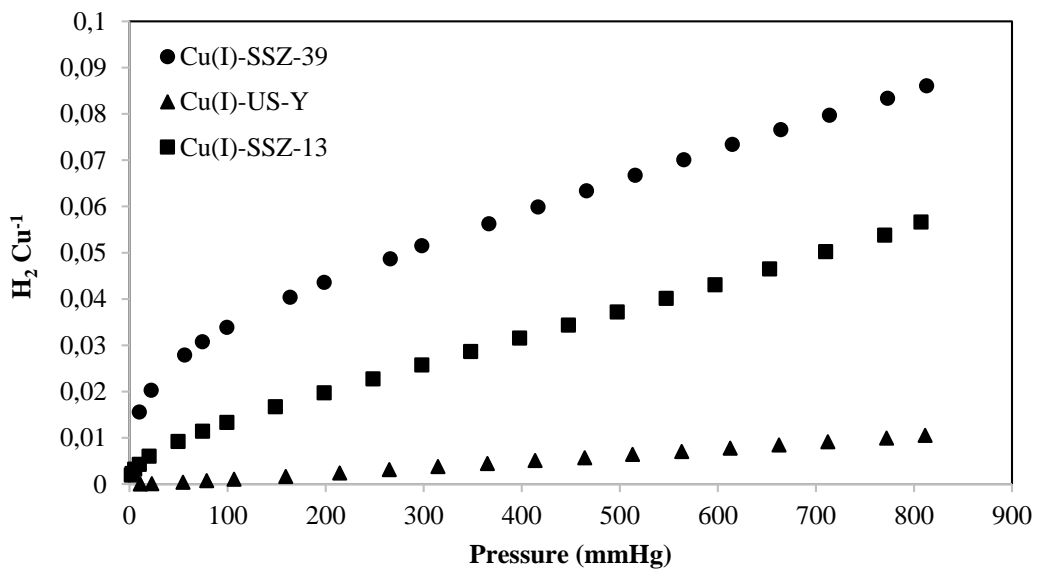


Figure 3.13. Adsorption isotherms in H₂/Cu of Cu(I)-SSZ-13, Cu(I)-SSZ-39 and Cu(I)-US-Y at 293 K

The H₂ adsorption isotherms (per gram of zeolite) obtained at 77 K can be seen in Figure 3.14. According to Figure 3.14, highest H₂ uptake capacity is obtained on Cu(I)-SSZ-39 followed by Cu(I)-SSZ-13 and Cu(I)-US-Y.

The calculated H₂ Cu⁻¹ ratios at 77 K are higher (Figure 3.15) when compared to 293 K, which means that H₂-zeolite pore wall interaction becomes more important at this temperature. When zeolite wall interaction is important (van der Waals interactions), cage size around 1 nm such as in Cu(I)-SSZ-13 (1.27 nm*0.94 nm) and Cu(I)-SSZ-39 (1.27 nm*1.16 nm) are expected to result in a higher H₂ uptake capacity [103]. Figure 3.14 and 3.15 confirm this theory with maximum H₂ uptake capacity for Cu(I)-SSZ-39 and Cu(I)-SSZ-13 (with cage sizes between 7 and 10 Å), but a very low capacity for Cu(I)-US-Y (with cage size around 12–18 Å). The isotherms obtained at 77 K are also fitted with a Langmuir (Equation 3.1) and a Sips model (Equation 3.2). Better goodness of fitting values (R²) are obtained with a Sips model (see Table 3.6-3.7), which is often used as an adsorption model for zeolites, and accounts for the heterogeneous adsorption sites (adsorption sites with different adsorption enthalpies).

$$Q_e = \frac{Q_{max}K_{eq}P}{1+K_{eq}P} \quad (\text{Eqn.3.1})$$

$$Q_e = \frac{Q_{max}bP^{1/n}}{1+bP^{1/n}} \quad (\text{Eqn.3.2})$$

According to the results of these fittings (Figure 3.16-3.18 and Table 3.6), higher affinity constant (b, in mmHg^{-1/n}) values for Cu(I)-SSZ-39 and Cu(I)-SSZ-13 samples are obtained, which further supports the theory of increasing interaction strength for smaller pore sizes.

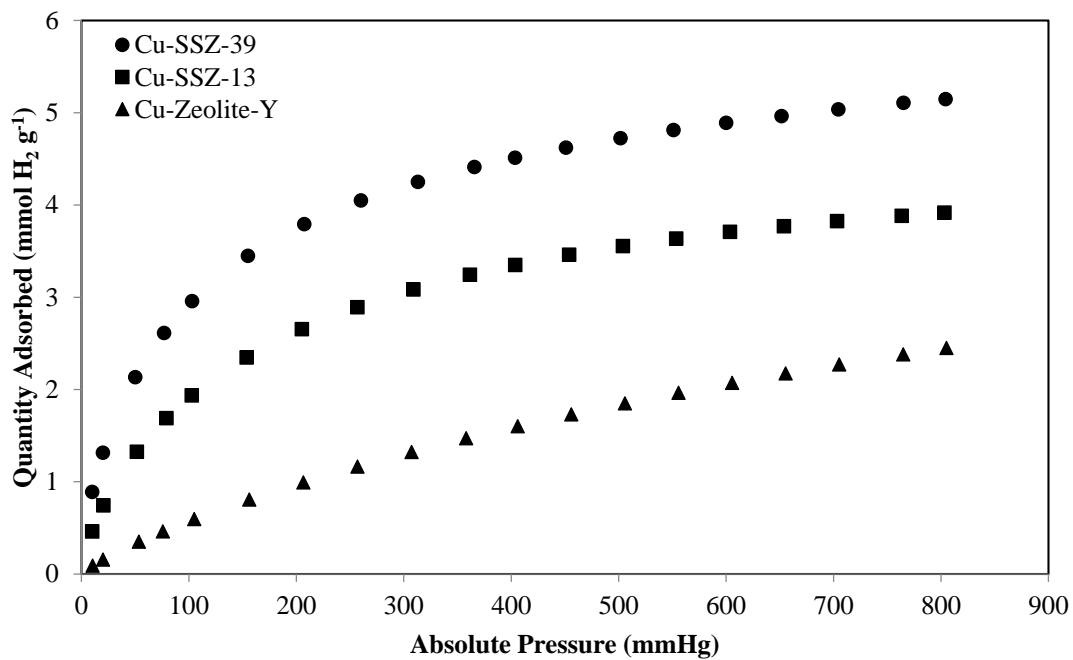


Figure 3.14. H₂ adsorption isotherms of Cu(I)-SSZ-13, Cu(I)-SSZ-39 and Cu(I)-US-Y at 77 K

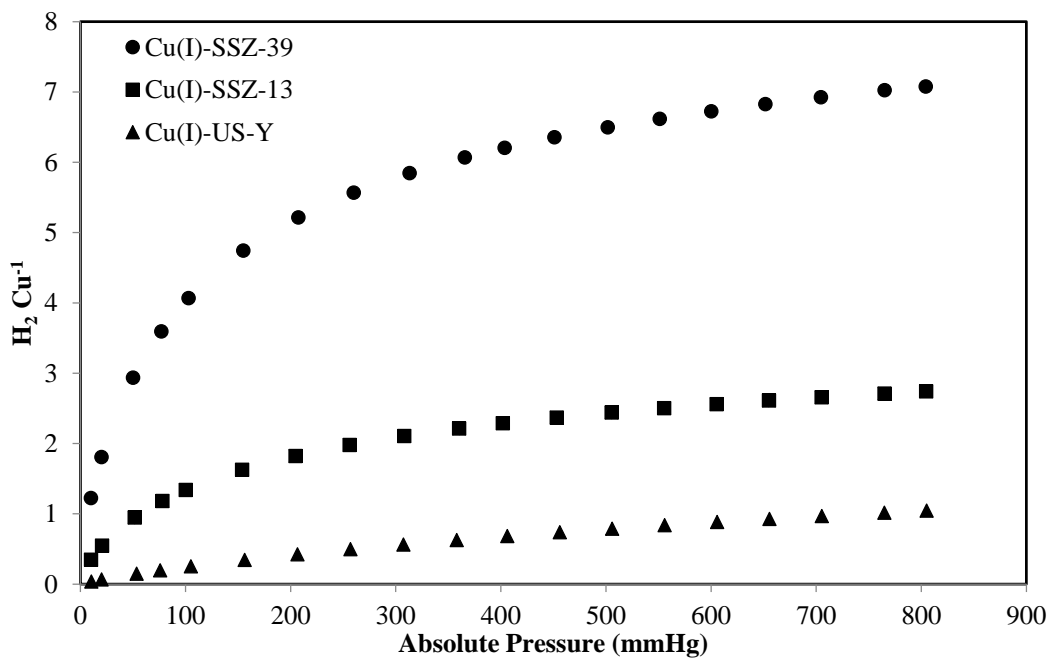


Figure 3.15. H₂ adsorption isotherms in H₂/Cu of Cu(I)-SSZ-13, Cu(I)-SSZ-39 and Cu(I)-US-Y at 77 K

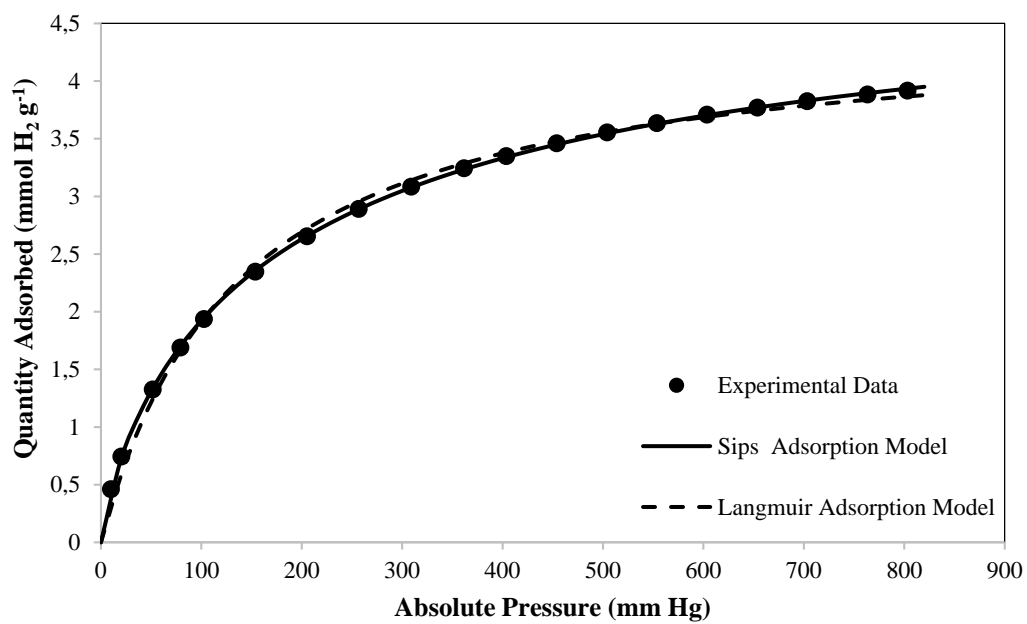


Figure 3.16. Experimental H₂ adsorption on Cu(I)-SSZ-13 at 77 K, Sips adsorption model and Langmuir adsorption model

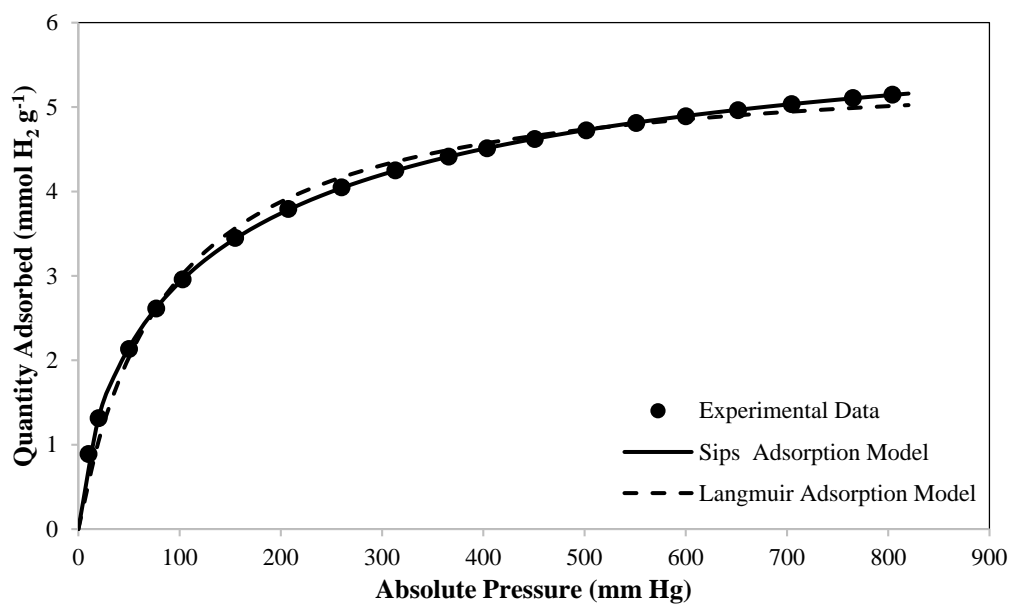


Figure 3.17. Experimental H₂ adsorption on Cu(I)-SSZ-39 at 77 K, Sips adsorption model and Langmuir adsorption model

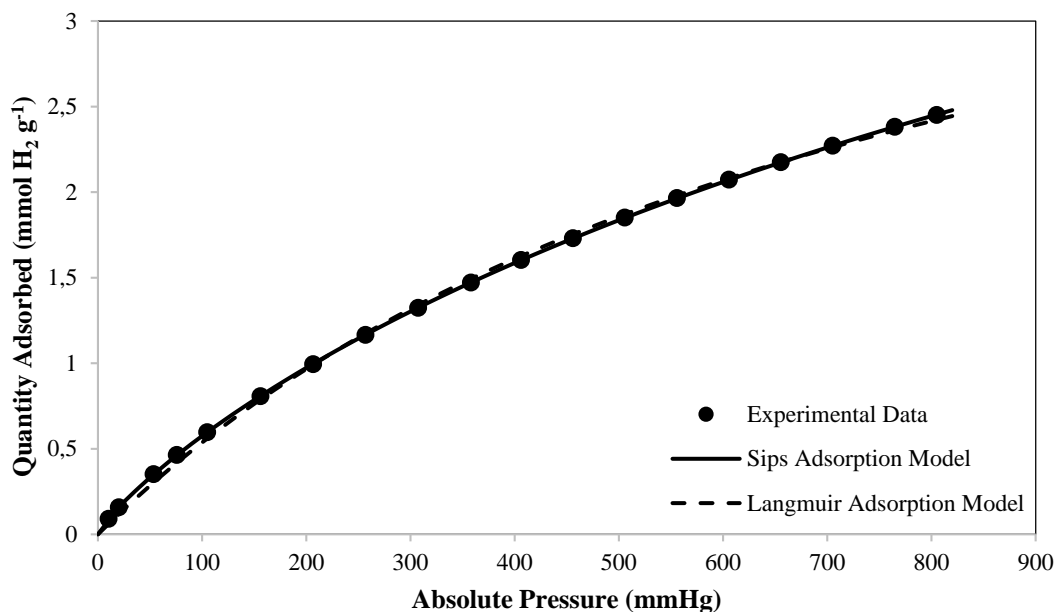


Figure 3.18. Experimental H₂ adsorption on Cu(I)-US-Y at 77 K, Sips adsorption model and Langmuir adsorption model

However, when pressure is increased at 77 K, the total micropore volumes will be important, which can be also inferred from Table 3.6. The potential adsorption capacity (Q_{\max} in mmol/g) obtained from a fitted Sips isotherm model for Cu(I)-US-Y is the highest among the tested zeolites (Micropore volume of Cu(I)-US-Y is higher (0.220 cm³/g) than other Cu(I)-exchanged samples, see Table 3.5). This situation indicates promising H₂ storage capacities on Cu(I)-US-Y for the high-pressure applications.

Table 3.6. Sips adsorption model fitting parameters of Cu(I)-SSZ-39, Cu(I)-SSZ-13 and, Cu(I)-US-Y at 77 K.

Sample	1/n	b (mmHg ^{-1/n})	Q_{\max} (mmol g ⁻¹)	R ²
Cu(I)-SSZ-39	0.722	0.0288	6.565	1
Cu(I)-SSZ-13	0.804	0.0145	5.182	0.9999
Cu(I)-US-Y	0.843	0.0017	7.683	1

Table 3.7 Langmuir adsorption model fitting parameters of Cu(I)-SSZ-39, Cu(I)-SSZ-13 and, Cu(I)-US-Y at 77 K

Sample	K_{eq} (mmHg ⁻¹)	Q_{max} (mmol g ⁻¹)	R^2
Cu(I)-SSZ-39	0.0116	5.551	0.9900
Cu(I)-SSZ-13	0.0075	4.507	0.9926
Cu(I)-US-Y	0.0013	4.830	0.9988

3.2.2.1. Isothermic Heat of Adsorption

H₂ adsorption capacities at room temperature are known to be directly correlated with H₂ adsorption enthalpies (binding strength at the adsorption sites). To be able to estimate the binding energies, application of Clasius-Clapeyron equation (Equation 3.3) is often performed on adsorption data obtained at three different temperatures. The pressure values for the identical adsorbed H₂ amounts are used in Clasius-Clapeyron equation for calculation of each isosteric heat of adsorption data.

$$\ln\left(\frac{P_2}{P_1}\right) = \frac{-\Delta H_{ads}}{R}\left(\frac{1}{T_2} - \frac{1}{T_1}\right) \quad (\text{Eqn.3.3})$$

In this project, we have performed H₂ adsorption on Cu(I)-SSZ-39 (Figure 3.19), Cu(I)-US-Y (Figure A.7) and Cu(I)-SSZ-13 (Figure A.11) at temperatures near 278 K, 293 K and 303 K. In order to get pressure data from the isotherms, the isotherms are modelled with a combination of Sips model and a linear model for the best prediction values.

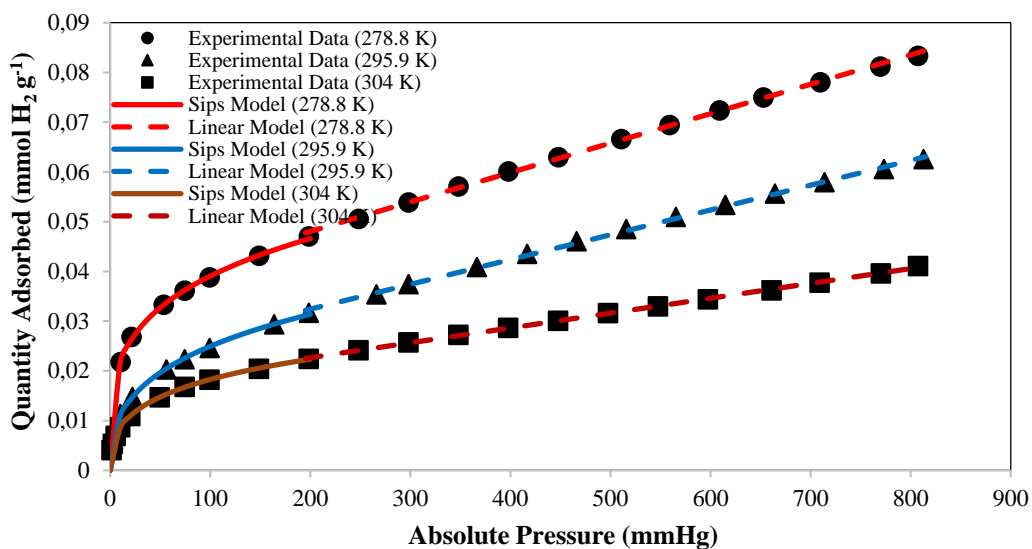


Figure 3.19. Experimental H₂ adsorption data on Cu(I)-SSZ-39 at 278.6 K, 295.9 K and 304 K, fitted Sips adsorption (continuous line) and linear models (dashed lines)

Using the fitted models, pressure values are calculated at constant n_{ads} values at three different temperatures and then at each n_{ads} value, $\ln P$ versus $1/T$ is plotted (Figure 3.20) and the slope of the linear regression is used to calculate isosteric heat of adsorption values (see Figures 3.21-3.22) using Clasius-Clapeyron adsorption model (slope: $-Q_{\text{st}}/R$).

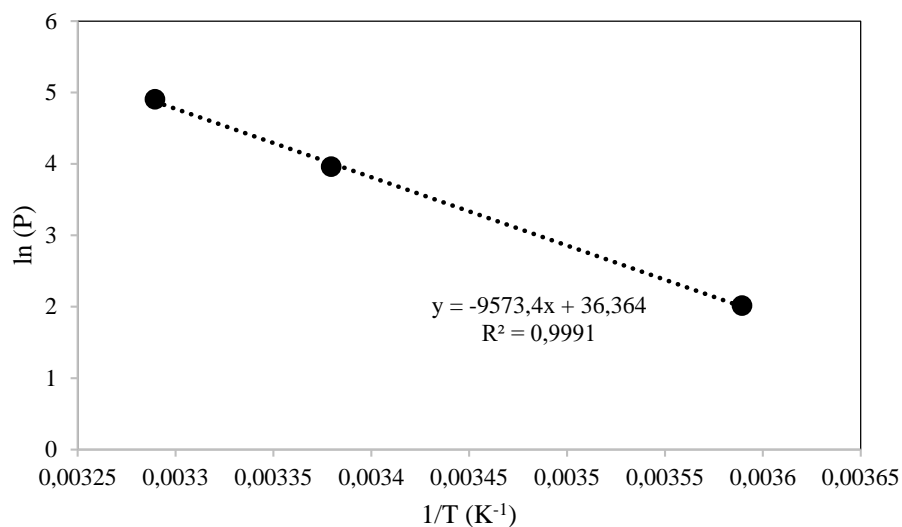


Figure 3.20. $\ln(P)$ versus $1/T$ of Cu(I)-SSZ-39 at quantity adsorbed = 0.024 mmol H₂ g⁻¹

Table 3.8. Data used to obtain isosteric heat of adsorption of Cu(I)-SSZ-39 between the temperatures 278.6 K and 304 K.

n_{adsorbed} (mol)	Q_{st}			R^2	
	$\ln(P_{278.6})$	$\ln(P_{295.9})$	$\ln(P_{304})$		
0.02	2.016	3.961	4.906	79.59	0.9991
0.022	2.389	4.236	5.178	76.57	0.9983
0.024	2.729	4.490	5.499	75.53	0.9949
0.026	3.043	4.727	5.741	73.38	0.9929
0.028	3.333	4.950	5.937	70.75	0.9923
0.03	3.603	5.160	6.100	67.89	0.9928
0.032	3.856	5.253	6.240	64.21	0.9838
0.034	4.093	5.444	6.363	61.27	0.9863
0.036	4.317	5.604	6.473	58.22	0.9868
0.038	4.528	5.742	6.571	55.13	0.986
0.04	4.729	5.863	6.661	52.04	0.984
0.042	4.920	5.971	6.744	48.98	0.9809

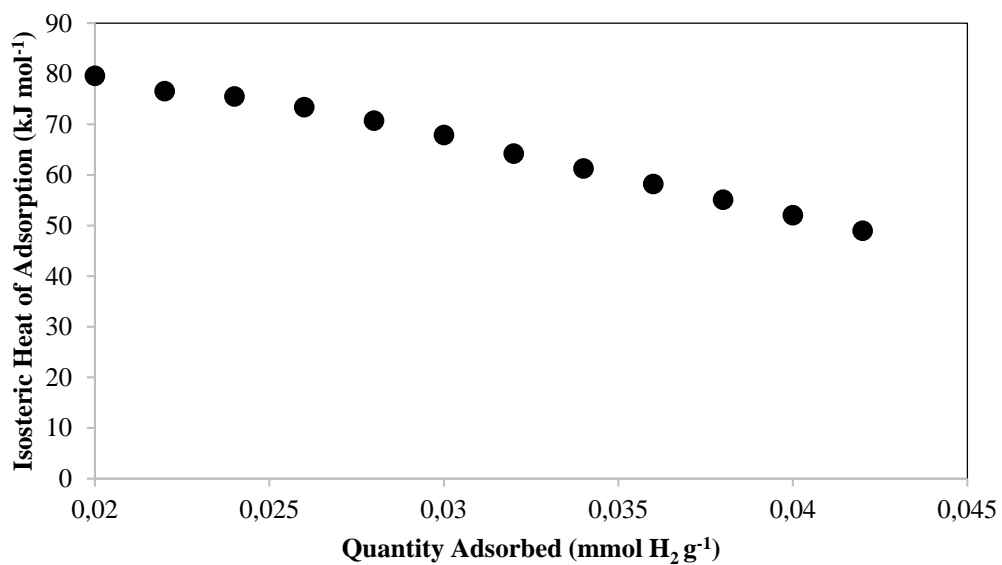


Figure 3.21. Isosteric heat of H₂ adsorption of Cu(I)-SSZ-39 between 278.6 K and 304 K

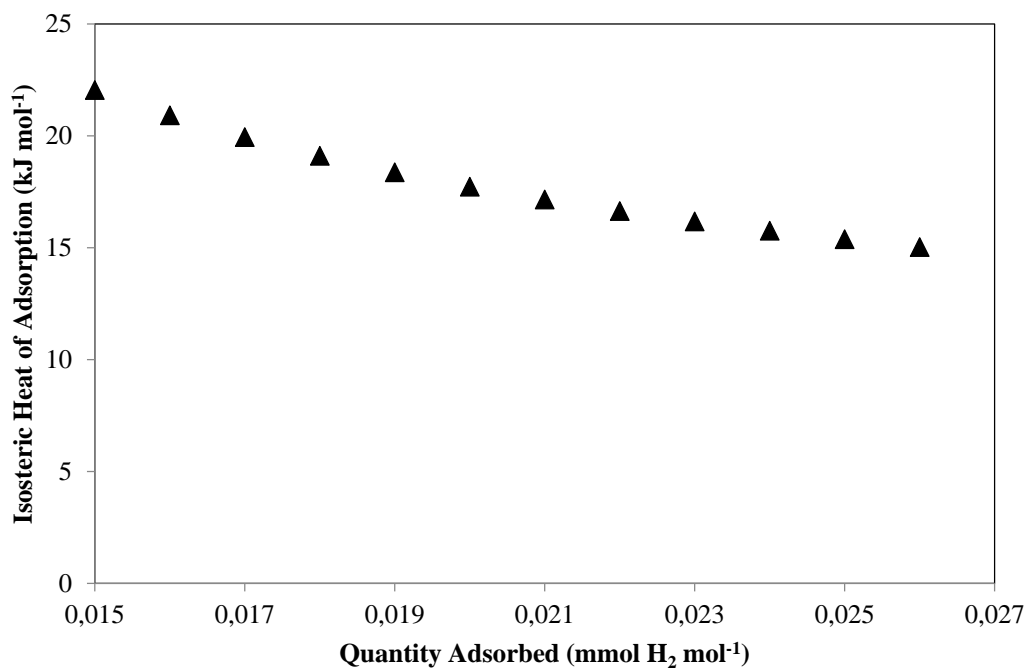


Figure 3.22. Isosteric heat of H₂ adsorption of Cu(I)-US-Y between 278.8 K and 303 K

Comparison of isosteric heat of H₂ adsorption data versus hydrogen uptake per copper ratio of Cu(I)-SSZ-39 and Cu(I)-US-Y is given in Figure 3.23. As seen from the figure, Cu(I)-SSZ-39 shows very high isosteric heat of adsorption values for the same H₂ Cu⁻¹ ratios. This situation explains the high H₂ uptake capacity per copper at room temperature (293 K) given in Figure 3.13. SSZ-39 has a framework consisting double-6-membered-ring (d6MR) and 8-membered-ring (8MR) structures similar to SSZ-13 framework. Cu(I)-sites on SSZ-13 and SSZ-39 are expected to be on the window of the 6MR windows and on the window of 8MR windows [104], [105]. For these Cu(I)-sites, H₂ binding energy on Cu(I) located on 8 MR is theoretically calculated to be higher (67 kJ mol⁻¹) when compared to binding on Cu(I) located on 6MR (18 kJ mol⁻¹) [105] Therefore, observed high Q_{st} values on Cu(I)-SSZ-39 might be explained by a dominating fraction of H₂ adsorbed on Cu(I) located on 8MRs.

SSZ-13 also has a framework consisting double-6-membered-ring (d6MR) and 8-membered-ring (8MR) structures that are arranged in a different sequence to form a *cha* cage (compared to *aei* cage in SSZ-39, Figure 3.24). Since SSZ-13 has similar framework building units as SSZ-39, Cu(I)-sites and therefore H₂ binding energies are expected to be similar. According to Ipek et al. the differential heat of H₂ adsorption values were found to be between 50 and 15 kJ/mol indicating H₂ adsorption on Cu(I) located both at 8MR and 6MR [102]. The lower expected H₂ binding energies would explain the lower H₂/Cu ratios observed here (see Figure 3.13).

Cu(I)-US-Y showed the lowest Q_{st} values and accordingly low H₂ adsorption capacity values (see Figure 3.13). US-Y and Zeolite Y, having a FAU framework consist of d6MRs that are connected with sodalite cages that are not accessible for adsorbates (Figure 3.24). On the other hand, some of the 6MRs are located near the super cage in the FAU framework that are accessible (43% of total copper on Zeolite Y, [94]). Observed Q_{st} values between 15 and 22 kJ mol⁻¹ on Cu(I)-US-Y should be resulting from Cu(I)- sites on these accessible 6MRs. On the other hand, observed lower mmol H₂ g⁻¹ and H₂ Cu⁻¹ ratios (Figure 3.12 and 3.13) can be explained by the low fraction of accessible Cu sites on US-Y.

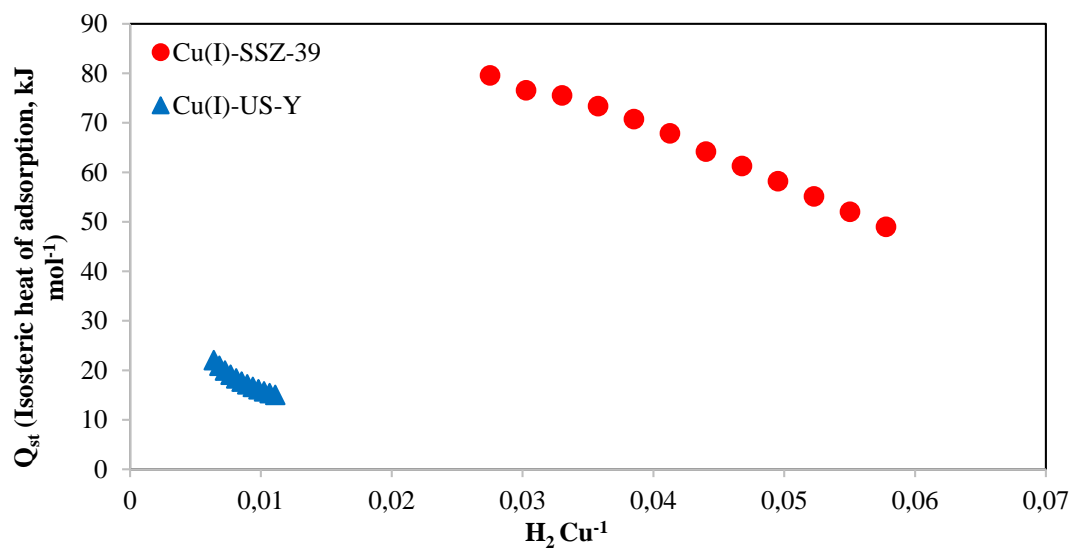


Figure 3.23. Isosteric heat of adsorption data versus H_2/Cu^{-1} ratio of Cu(I)-SSZ-39 and Cu(I)-US-Y between the temperatures of 278 and 304 K

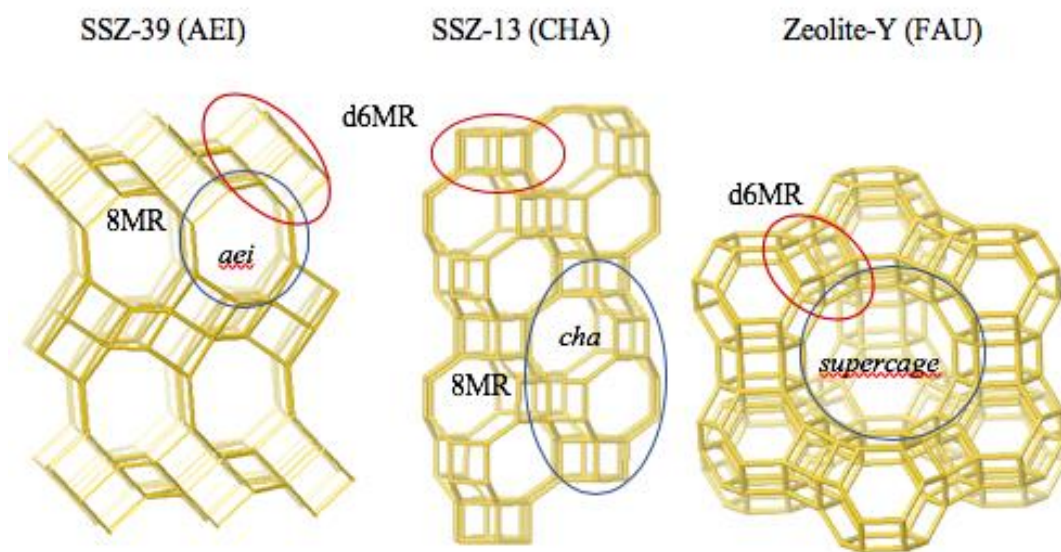


Figure 3.24. Schematic drawing of SSZ-39 (AEI), SSZ-13 (CHA), Zeolite-Y (FAU) and building units

CHAPTER 4

CONCLUSION

To conclude, Cu(I)-exchanged zeolites are prepared to develop a lightweight, safe and economic H₂ storage system to be implemented in fuel cell powered vehicles, which would potentially reach the target H₂ storage capacity of 5.5 wt.%.

In the first part of the study, [B]-ZSM-5, [Al]-ZSM-5 and mesoporous [B]-ZSM-5 are synthesized successfully with Si/Al ratios 55, 43 and 101, respectively. A new Cu(I)-exchange method is developed and applied to the synthesized zeolites. In this new Cu(I)-exchange method, after increasing CuCl/acetonitrile concentration from 0.01 M to 0.02 M and adopting vacuum pretreatment, Cu/Al ratios are found as high as 1.05 with trace amounts of Cl in the zeolite crystals. Cu(I)-exchanged zeolites; [B]-ZSM-5 and [Al]-ZSM-5 show promising H₂ uptake capacities reaching 0.03 wt. % at 323 K and 40 kPa. Their initial adsorption enthalpies are reaching up to 95 kJ mol⁻¹, which then decays below 15 kJ mol⁻¹ after H₂ Cu⁻¹ ratios of 0.15. When compared, Cu(I)-[Al]-ZSM-5 and Cu(I)-[B]-ZSM-5 show similar H₂ binding energies, which result in similar H₂ uptake capacities per Cu basis. In contrast, higher differential heat of adsorption values and a higher H₂ storage capacities per Cu are observed for mesoporous Cu(I)-[B]-ZSM-5 at similar conditions, indicating higher energy Cu(I) sites on mesoporous sample.

In the second part of the study, SSZ-13, SSZ-39, acid-treated SSZ-39 and US-Y are Cu(I)-exchanged to reach Cu/Al ratios of 1.08, 0.34, 0.73 and 1.06, respectively. At room temperature (293 K), Cu(I)-SSZ-39 shows the highest adsorption capacity both per gram of zeolite and per Cu basis. Isothermic heat of H₂ adsorption values on these zeolites are also calculated for these samples applying Clausius-Clapeyron equation to the experimental isotherm data obtained at three different temperatures (278 K, 293 K, 303 K). According to the calculations, isothermic heat of adsorption values were found to be in the range of 80-49 kJ mol⁻¹ and 21-15 kJ mol⁻¹ for Cu(I)-SSZ-39 and

Cu(I)-US-Y respectively. Higher values of isosteric heat of adsorption observed on Cu(I)-SSZ-39 is related to the exclusive H₂ adsorption on Cu(I)-sites on 8MR of the SSZ-39, which is expected to give high H₂ binding energies (around 67 kJ mol⁻¹). For Cu(I)-SSZ-13, H₂ adsorption on a combination of Cu(I)-locations on 8MR and 6MRs are suggested, which explains lower H₂ Cu⁻¹ ratios obtained at 1 atm.

Acid-treatment did not result in successful mesopore formation but crystal size reduction and macropore formations on SSZ-39.

Cu(I)-US-Y showed both low H₂ Cu⁻¹ ratios and low isosteric heat of H₂ adsorption values (21-15 kJ mol⁻¹) at room temperature due to inaccessible Cu(I)-centers in FAU framework. The accessible sites are Cu(I)-sites on 6MRs on FAU, whose isosteric heat of adsorption values are in agreement with the theoretical H₂ binding energies around 18 kJ mol⁻¹, which renders Cu(I)-US-Y a non-desirable storage material at room temperature and low pressure values.

The H₂ adsorption capacities per gram basis at 77 K were observed to be correlated with cage sizes in AEI, CHA and FAU frameworks. Smaller cage sizes in AEI (Cu(I)-SSZ-39) and CHA (Cu(I)-SSZ-13) resulted in higher H₂ uptake capacities at 77 K and 1 atm when compared to Cu(I)-US-Y. However, when the maximum H₂ adsorption capacity values are calculated using a Sips isotherm model, the high mesopore volume of US-Y resulted in higher potential H₂ storage capacity, which may be useful for higher H₂ adsorption pressures.

REFERENCES

- [1] S. Niaz, T. Manzoor, and A. H. Pandith, "Hydrogen storage: Materials, methods and perspectives," *Renew. Sustain. Energy Rev.*, vol. 50, pp. 457–469, 2015.
- [2] "Daily CO₂," 2018. [Online]. Available: <https://www.co2.earth/daily-co2>. [Accessed: 20-Aug-2018].
- [3] T. N. Veziroglu and F. Barbir, "Hydrogen: the wonder fuel," *Int. J. Hydrogen Energy*, vol. 17, no. 6, pp. 391–404, 1992.
- [4] A. W. C. van den Berg and C. O. Areán, "Materials for hydrogen storage: current research trends and perspectives," *Chem. Commun.*, no. 6, pp. 668–681, 2008.
- [5] A. Züttel, "Materials for hydrogen storage," *Mater. Today*, vol. 6, no. 9, pp. 24–33, 2003.
- [6] R. Kothari, D. Buddhi, and R. L. Sawhney, "Comparison of environmental and economic aspects of various hydrogen production methods," *Renew. Sustain. Energy Rev.*, vol. 12, no. 2, pp. 553–563, 2008.
- [7] H. Gaffron, "Fermentative AND Photochemical Production of Hydrogen in Algae," *Rubin, J.*, vol. 26, p. 219, 1942.
- [8] E. Fakioglu, Y. Yurum, and T. N. Veziroglu, "A review of hydrogen storage systems based on boron and its compounds.," *Int. J. Hydrogen Energy*, vol. 29, p. 1371, 2004.
- [9] S. Z. Baykara and E. Bilgen, "An overall assessment of hydrogen production by solar water thermolysis.," *Int. J. Hydrogen Energy*, vol. 14, p. 881, 1989.
- [10] B. Ewan and R. Allen, "A figure of merit assessment of the routes to hydrogen.," *Int. J. Hydrog. Energy*, vol. 30, p. 809, 5AD.
- [11] W. Kreuter and H. Hofmann, "Electrolysis: the important energy transformer in a world of sustainable energy.," *Int. J. Hydrogen Energy*, vol. 23, p. 661, 1998.

- [12] M. Hirscher, *Handbook of hydrogen storage: new materials for future energy storage*. Weinheim: Wiley-VCH Verlag GmbH & Co. KGaA, 2010.
- [13] L. Schlapbach and A. Züttel, “Hydrogen-storage materials for mobile applications,” *Nature*, vol. 414, no. 6861, pp. 353–358, 2001.
- [14] M. P. Suh, H. J. Park, T. K. Prasad, and D. W. Lim, “Hydrogen storage in metal-organic frameworks,” *Chem. Rev.*, vol. 112, no. 2, pp. 782–835, 2012.
- [15] S. Tedds, A. Walton, D. P. Broom, and D. Book, “Characterisation of porous hydrogen storage materials: Carbons, zeolites, MOFs and PIMs,” *Faraday Discuss.*, vol. 151, pp. 75–94, 2011.
- [16] A. F. Dalebrook, W. Gan, M. Grasmann, S. Moret, and G. Laurenczy, “Hydrogen storage: Beyond conventional methods,” *Chem. Commun.*, vol. 49, no. 78, pp. 8735–8751, 2013.
- [17] B. Sakintuna, F. Lamari-Darkrim, and M. Hirscher, “Metal hydride materials for solid hydrogen storage: A review,” *Int. J. Hydrogen Energy*, vol. 32, no. 9, pp. 1121–1140, 2007.
- [18] F. Ding and B. I. Yakobson, “Challenges in hydrogen adsorptions: From physisorption to chemisorption,” *Front. Phys.*, vol. 6, no. 2, pp. 142–150, 2011.
- [19] S. Bulyarskiy and A. Saurov, Eds., *Doping of Carbon Nanotubes*. Springer International, 2017.
- [20] H. Imamura, K. Masarani, M. Kusuhara, H. Katsumoto, T. Sumi, and T. Sakata, “High hydrogen storage capacity of nanosized magnesium synthesized by high energy ball-milling,” *J. Alloy. Compd.*, vol. 386, p. 211, 2005.
- [21] S. Corre, M. Bououdina, D. Fruchart, and G. Y. Adachi, “Stabilisation of high dissociation pressure hydrides of formula $\text{La}_{1-x}\text{Ce}_x\text{Ni}_5$ with carbon monoxide,” *J. Alloys Compd.*, vol. 275, pp. 99–104, 1998.
- [22] U. B. Demirci, O. Akdim, and P. Miele, “Ten-year efforts and a no-go recommendation for sodium borohydride for on-board automotive hydrogen storage,” *Int. J. Hydrogen Energy*, vol. 34, no. 6, pp. 2638–2645, 2009.
- [23] D. Hua, Y. Hanxi, A. Xinping, and C. Chuansin, “Hydrogen production from catalytic hydrolysis of sodium borohydride solution using nickel boride

- catalyst.," *Int. J. Hydrogen Energy*, vol. 28, p. 1095, 2003.
- [24] G. Barkhordarian, T. Klassen, and R. Bormann, "Effect of Nb₂O₅ content on hydrogen reaction kinetics of Mg.," *J. Alloys Compd.*, vol. 364, p. 242, 2004.
- [25] F. E. Pinkerton, G. P. Meisner, M. S. Meyer, M. P. Balogh, and M. D. Kundrat, "Hydrogen desorption exceeding ten weight percent from the new quaternary hydride LiBN₂H₈," *J. Phys. Chem.*, vol. 109, pp. 6–8, 2005.
- [26] J. J. Vajo, S. L. Skeith, and F. Mertens, "Reversible storage of hydrogen in destabilized LiBH₄," *J. Phys. Chem.*, vol. 109, pp. 3719–3722, 2005.
- [27] S. C. Amendola, S. L. Sharp-Goldman, M. Saleem Janjua, M. T. Kelly, P. J. Petillo, and M. Binder, "An ultrasafe hydrogen generator: aqueous, alkaline borohydride solutions and Ru catalyst.," *J. Power Sources*, vol. 85, p. 186, 2000.
- [28] H. I. Schlesinger, H. C. Brown, A. E. Finholt, J. R. Gilbreath, H. R. Hoekstra, and E. K. Hyde, "Sodium borohydride, its hydrolysis and use as a reducing agent and in the generation of hydrogen.," *J. Am. Chem. Soc.*, vol. 75, p. 215, 1953.
- [29] S. S. Muir and X. Yao, "Progress in sodium borohydride as a hydrogen storage material : Development of hydrolysis catalysts and reaction systems," *Int. J. Hydrogen Energy*, vol. 36, no. 10, pp. 5983–5997, 2011.
- [30] A. Bouza, C. J. Read, S. Satyapal, and J. Milliken, "Annual DOE hydrogen program review, hydrogen storage, office of hydrogen, fuel cells, and infrastructure technologies.," 2004.
- [31] D. P. Broom and D. Book, *Hydrogen storage in nanoporous materials*. Woodhead Publishing Limited, 2014.
- [32] H. Wang, Q. Gao, and J. Hu, "High Hydrogen Storage Capacity of Porous Carbons Prepared by Using Activated Carbon," no. 13, pp. 7016–7022, 2009.
- [33] M. Jordá-Beneyto, F. Suárez-García, D. Lozano-Castelló, D. Cazorla-Amorós, and A. Linares-Solano, "Hydrogen storage on chemically activated carbons and carbon nanomaterials at high pressures," *Carbon N. Y.*, vol. 45, no. 2, pp. 293–303, 2007.

- [34] P. Chen, "High H₂ Uptake by Alkali-Doped Carbon Nanotubes Under Ambient Pressure and Moderate Temperatures," *Science (80-.)*, vol. 285, no. 5424, pp. 91–93, 1999.
- [35] L. J. Murray, M. Dinc, and J. R. Long, "Hydrogen storage in metal-organic frameworks," *Chem. Soc. Rev.*, vol. 38, no. 5, pp. 1294–1314, 2009.
- [36] P. Falcaro *et al.*, "Application of metal and metal oxide nanoparticles at MOFs," *Coord. Chem. Rev.*, vol. 307, pp. 237–254, 2016.
- [37] Q. L. Zhu and Q. Xu, "Metal-organic framework composites," *Chem. Soc. Rev.*, vol. 43, no. 16, pp. 5468–5512, 2014.
- [38] S. Kitagawa, R. Kitaura, and S. I. Noro, "Functional porous coordination polymers," *Angew. Chemie - Int. Ed.*, vol. 43, no. 18, pp. 2334–2375, 2004.
- [39] H. Furukawa *et al.*, "Ultrahigh porosity in metal-organic frameworks," *Science (80-.)*, vol. 329, no. 5990, pp. 424–428, 2010.
- [40] T. Yamada, K. Otsubo, R. Makiura, and H. Kitagawa, "Designer coordination polymers: Dimensional crossover architectures and proton conduction," *Chem. Soc. Rev.*, vol. 42, no. 16, pp. 6655–6669, 2013.
- [41] B. Chen, Y. Yang, F. Zapata, G. Lin, G. Qian, and E. B. Lobkovsky, "Luminescent open metal sites within a metal-organic framework for sensing small molecules," *Adv. Mater.*, vol. 19, no. 13, pp. 1693–1696, 2007.
- [42] J. Della Rocca, D. Liu, and W. Lin, "Nanoscale Metal – Organic Frameworks for Biomedical Imaging and Drug Delivery Synthesis of Nanoscale Metal – Organic Frameworks," pp. 1–14.
- [43] A. G. Wong-Foy, A. J. Matzger, and O. M. Yaghi, "Exceptional H₂ saturation uptake in microporous metal-organic frameworks," *J. Am. Chem. Soc.*, vol. 128, no. 11, pp. 3494–3495, 2006.
- [44] O. K. Farha *et al.*, "Metal-organic framework materials with ultrahigh surface areas: is the sky the limit?," *J. Am. Chem. Soc.*, vol. 134, no. 36, 2012.
- [45] H. Furukawa, M. A. Miller, and O. M. Yaghi, "Independent verification of the saturation hydrogen uptake in MOF-177 and establishment of a benchmark for hydrogen adsorption in metal-organic frameworks," *J. Mater. Chem.*, vol. 17,

- no. 30, pp. 3197–3204, 2007.
- [46] S. S. Kaye, A. Dailly, O. M. Yanghi, and J. R. Long, “Impact of Preparation and Handling on the Hydrogen Storage Properties of $\text{Zn}_4\text{O}(\text{1,4-benzenedicarboxylate})_3$ (MOF-5),” *J. Am. Chem. Soc.*, vol. 129, no. 14176, 2007.
- [47] X. Wang *et al.*, “No Title,” *Chem. Mater.*, vol. 20, p. 3145, 2008.
- [48] W. Yang *et al.*, “No Title,” *Chem. Commun.*, vol. 44, p. 359, 2008.
- [49] T. K. Kim and M. P. Suh, “Selective CO_2 adsorption in a flexible non-interpenetrated metal–organic framework,” *Chem. Commun.*, vol. 47, p. 4258, 2011.
- [50] J. Y. Lee, D. H. Olson, L. Pan, T. J. Emge, and J. Li, “Microporous metal-organic frameworks with high gas sorption and separation capacity,” *Adv. Funct. Mater.*, vol. 17, p. 1255, 2007.
- [51] T. Takei *et al.*, “Hydrogen Adsorption Properties of Lantern-Type Dinuclear $\text{M}(\text{BDC})(\text{DABCO})_{1/2}$,” *Bull. Chem. Soc. Jpn.*, vol. 81, p. 847, 2008.
- [52] X. Liu, M. Oh, and M. S. Lah, “Size- and shape-selective isostructural microporous metal-organic frameworks with different effective aperture sizes,” *Inorg. Chem.*, vol. 50, p. 5044, 2011.
- [53] D. J. Collins and H. C. Zhou, “Hydrogen storage in metal–organic frameworks,” *J. Mater. Chem.*, vol. 15, p. 3154, 2007.
- [54] T. K. Prasad, D. H. Hong, and M. P. Suh, “High Gas Sorption and Metal-Ion Exchange of Microporous Metal–Organic Frameworks with Incorporated Imide Groups,” *Chem.-Eur. J.*, vol. 16, p. 14043, 2010.
- [55] B. Zheng, Z. Liang, G. Li, Q. Huo, and Y. Liu, “Synthesis, Structure, and Gas Sorption Studies of a Three-Dimensional Metal–Organic Framework with NbO Topology,” *Cryst. Growth Des.*, vol. 20, p. 3405, 2010.
- [56] S. H. Yang *et al.*, “No Title,” *Chem.-Eur. J.*, vol. 15, p. 4829, 2009.
- [57] H. W. Langmi *et al.*, “Hydrogen storage in ion-exchanged zeolites,” *J. Alloys Compd.*, vol. 404–406, no. SPEC. ISS., pp. 637–642, 2005.
- [58] J. G. Vitillo, G. Ricchiardi, G. Spoto, and A. Zecchina, “Theoretical maximal

- storage of hydrogen in zeolitic frameworks.," vol. 7, pp. 3948–3954, 2005.
- [59] H. W. Langmi *et al.*, "Hydrogen adsorption in zeolites A, X, Y and RHO," *J. Alloys Compd.*, vol. 356–357, pp. 710–715, 2003.
- [60] S. B. Kayiran and F. Lamari-Darkrim, "Synthesis and ionic exchanges of zeolites for gas adsorption," *Surf Interface Anal*, vol. 34, no. 100, 2002.
- [61] J. Weitkamp, M. Fritz, and S. Ernst, "Zeolites as Media for Hydrogen Storage," *Int. J. Hydrogen Energy*, vol. 20, no. 967, 1995.
- [62] V. B. Kazansky, V. Y. Borovkov, A. Serich, and H. G. Karge, "Low Temperature Hydrogen Adsorption on Sodium Forms of Faujasites; Barometric Measurements and Drift Spectra," *Microporous Mesoporous Mater.*, vol. 22, no. 251, 1998.
- [63] P. A. Georgiev, A. Albinati, and J. Eckert, "Room temperature isosteric heat of dihydrogen adsorption on Cu(I) cations in zeolite ZSM-5," *Chem. Phys. Lett.*, vol. 449, no. 1–3, pp. 182–185, 2007.
- [64] C. Otero Areán, G. Turnes Palomino, and M. R. Llop Carayol, "Variable temperature FT-IR studies on hydrogen adsorption on the zeolite (Mg,Na)-Y," *Appl. Surf. Sci.*, vol. 253, no. 13 SPEC. ISS., pp. 5701–5704, 2007.
- [65] C. Otero Areán, O. V. Manoilova, B. Bonelli, M. Rodriguez Delgado, G. Turnes Palomino, and E. Garrone, "Thermodynamics of hydrogen adsorption on the zeolite Li-ZSM-5.," *Chem. Phys. Lett.*, vol. 370, no. 5–6, pp. 631–635, 2003.
- [66] C. O. Areán *et al.*, "Thermodynamic studies on hydrogen adsorption on the zeolites Na-ZSM-5 and K-ZSM-5," *Microporous Mesoporous Mater.*, vol. 80, no. 1–3, pp. 247–252, 2005.
- [67] G. Turnes Palomino *et al.*, "Variable temperature FTIR studies on the interaction between molecular hydrogen and alkali-metal-exchanged ZSM-5 zeolites.," *Stud. Surf. Sci. Catal.*, vol. 158, pp. 853–860, 2005.
- [68] G. Turnes Palomino, M. R. Llop Carayol, and C. Otero Areán, "Thermodynamics of hydrogen adsorption on the zeolite Ca-Y.," *Catal. Today*, vol. 138, no. 3–4, pp. 249–252, 2008.

- [69] E. Garrone, B. Bonelli, and C. Otero Areán, “Enthalpy–entropy correlation for hydrogen adsorption on zeolites.,” *Chem. Phys. Lett.*, vol. 456, no. 1–3, pp. 68–70, 2008.
- [70] L. Regli *et al.*, “Hydrogen storage in Chabazite zeolite frameworks,” *Phys. Chem. Chem. Phys.*, vol. 7, no. 17, pp. 3197–3203, 2005.
- [71] A. Zecchina *et al.*, “Liquid hydrogen in protonic chabazite.,” *J. Am. Chem. Soc.*, vol. 127, p. 6361, 2005.
- [72] M. G. Nijkamp, J. E. M. J. Raaymakers, A. J. van Dillen, and K. P. de Jong, “Hydrogen storage using physisorption – materials demands,” *Appl. Phys. A Mater. Sci. Process.*, vol. 72, no. 5, pp. 619–623, 2001.
- [73] C. Baerlocher, W. M. Meier, and D. H. Olson, *Atlas of zeolite framework types*. Amsterdam: Elsevier, 2001.
- [74] M. A. Makarova, K. M. Zholobenko, N. E. Alghefaili, J. D. Thompson, and J. Dwyer, “Brønsted acid sites in zeolites. FTIR study of molecular hydrogen as a probe for acidity testing,” *J. Chem. Soc. Faraday Trans.*, vol. 90, p. 1047, 1994.
- [75] R. Ding, Z. Zhu, X. Yao, Z. Yan, and G. M. Lu, “NiNaY Composites at Room and Cryogenic Temperatures,” *Catal. Today*, vol. 158, 2010.
- [76] F. Darkrim, A. Aoufi, P. Malbrunot, and D. Levensque, “Hydrogen adsorption in the NaA zeolite: a comparison between numerical simulations and experiments.,” *J. Chem. Phys.*, vol. 112, no. 9, p. 5991, 2000.
- [77] M. Iwamoto, S. Yokoo, K. Sakai, and S. Kagawa, “Catalytic decomposition of nitric oxide over copper(II)-exchanged, Y-type zeolites,” *J. Chem. Soc. Faraday Trans.*, vol. 77, p. 1629, 1981.
- [78] M. Iwamoto, H. Furukawa, Y. Mine, F. Uemura, S. Mikuiya, and S. Kagawa, “Copper(II) ion-exchanged ZSM-5 zeolites as highly active catalysts for direct and continuous decomposition of nitrogen monoxide.,” *J. Chem. Soc. Chem. Commun.*, vol. 16, p. 1272, 1986.
- [79] J. Li, H. Chang, L. Ma, J. Hao, and R. T. Yang, “Low-temperature selective catalytic reduction of NO_x with NH₃ over metal oxide and zeolite catalysts-a

- review.,” *Catal. Today*, vol. 175, pp. 147–156, 2011.
- [80] A. B. Ene, T. Archipov, and E. Roduner, “Competitive Adsorption and Interaction of Benzene and Oxygen on Cu/HZSM5 Zeolites.,” *J. Phys. Chem.*, vol. 115, pp. 3688–3694, 2011.
- [81] N. V. Beznis, B. M. Weckhuysen, and J. H. Bitter, “Cu-ZSM-5 Zeolites for the Formation of Methanol from Methane and Oxygen: Probing the Active Sites and Spectator Species.,” *Catal. Letters*, vol. 138, pp. 14–22, 2010.
- [82] S. A. Anderson and T. W. Root, “Investigation of the effect of carbon monoxide on the oxidative carbonylation of methanol to dimethyl carbonate over Cu+X and Cu+ZSM-5 zeolites,” *J. Mol. Catal. A Chem.*, vol. 220, pp. 247–255, 2004.
- [83] P. Kozyra, M. Świetek, J. Datka, and E. Broclawik, “Ag+ and Cu+ Cations Ligated by Zeolite Environment Enhancing Hydrogen Activation – ETS-NOCV Charge-Transfer Analysis,” *J. Comput. Chem. Japan*, vol. 12, no. 1, pp. 30–37, 2013.
- [84] A. I. Serykh and V. B. Kazansky, “Unusually strong adsorption of molecular hydrogen on Cu+ sites in copper-modified ZSM-5.,” *Phys. Chem. Chem. Phys.*, vol. 6, p. 5250, 2004.
- [85] X. Solans-Monfort *et al.*, “Can Cu+-Exchanged Zeolites Store Molecular Hydrogen? An Ab-Initio Periodic Study Compared with Low-Temperature FTIR.,” *J. Phys. Chem.*, vol. 108, pp. 8278–8286, 2004.
- [86] B. Ipek, R. A. Pollock, C. M. Brown, D. Uner, and R. F. Lobo, “H₂ Adsorption on Cu(I)-SSZ-13,” *J. Phys. Chem. C*, vol. 122, no. 1, pp. 540–548, 2017.
- [87] S. Yashnik and Z. Ismagilov, “Zeolite ZSM-5 containing copper ions: The effect of the copper salt anion and NH₄OH/Cu²⁺ ratio on the state of the copper ions and on the reactivity of the zeolite in DeNO_x,” *Kinet. Catal.*, vol. 57, pp. 776–796, 2016.
- [88] J. H. Kwak, R. G. Tonkyn, T. D. Kim, J. Szanyi, and C. H. Peden, “Excellent activity and selectivity of Cu-SSZ-13 in the selective catalytic reduction of NO_x with NH₃.,” *J. Catal.*, vol. 275, no. 2, pp. 187–190, 2010.
- [89] D. W. Fickel and R. F. Lobo, “Copper coordination in Cu-SSZ-13 and Cu-SSZ-

- 16 investigated by variable-temperature XRD.," *J. Phys. Chem.*, vol. 114, pp. 1633–1640, 2010.
- [90] Y. Zhang, I. J. Drake, and A. T. Bell, "Characterization of Cu-ZSM-5 prepared by solid-state ion exchange of H-ZSM-5 with CuCl," *Chem. Mater.*, vol. 18, no. 9, pp. 2347–2356, 2006.
- [91] I. J. Drake, Y. Zhang, D. Briggs, B. Lim, T. Chau, and A. T. Bell, "The local environment of Cu⁺ in Cu-Y zeolite and its relationship to the synthesis of dimethyl carbonate," *J. Phys. Chem. B*, vol. 110, no. 24, pp. 11654–11664, 2006.
- [92] D. Sen, C. W. Kim, N. H. Heo, and K. Seff, "Using CuCl vapor to ion exchange copper into zeolite Na-Y. Single crystal structure of [Cu₃₀Na₃₀Cl₁₉][Si₁₂₁Al₇₁O₃₈₄]-FAU containing Cu₁₆Cl₇ 21⁺, Cu₄Cl₇⁺, Cu₃Cl₂⁺, and Cu²⁺," *Microporous Mesoporous Mater.*, vol. 185, no. 3, pp. 16–25, 2014.
- [93] V. B. Kazansky and E. A. Pidko, "A new insight in the unusual adsorption properties of Cu⁺cations in Cu-ZSM-5 zeolite," *Catal. Today*, vol. 110, no. 3–4, pp. 281–293, 2005.
- [94] T. Palomino, S. Bordiga, A. Zecchina, G. L. Marra, and C. Lamberti, "XRD, XAS, and IR characterization of copper-exchanged γ zeolite.," *J. Phys. Chem. B*, vol. 104, pp. 8641–8651, 2000.
- [95] H. Frost, T. Düren, and R. Q. Snurr, "Effects of surface area, free volume, and heat of adsorption on hydrogen uptake in metal-organic frameworks," *J. Phys. Chem. B*, vol. 110, no. 19, pp. 9565–9570, 2006.
- [96] T. Xue, H. Liu, Y. Zhang, H. Wu, P. Wu, and M. He, "Synthesis of ZSM-5 with hierarchical porosity: In-situ conversion of the mesoporous silica-alumina species to hierarchical zeolite," *Microporous Mesoporous Mater.*, vol. 242, pp. 190–199, 2017.
- [97] K. Leng, Y. Sun, X. Zhang, M. Yu, and W. Xu, "Ti-modified hierarchical mordenite as highly active catalyst for oxidative desulfurization of dibenzothiophene," *Fuel*, vol. 174, pp. 9–16, 2016.

- [98] M. A. Sanhoob, O. Muraza, E. N. Shafei, T. Yokoi, and K. H. Choi, "Steam catalytic cracking of heavy naphtha (C12) to high octane naphtha over B-MFI zeolite," *Appl. Catal. B Environ.*, vol. 210, pp. 432–443, 2017.
- [99] C. Zhang, H. Chen, X. Zhang, and Q. Wang, "TPABr-grafted MWCNT as bifunctional template to synthesize hierarchical ZSM-5 zeolite," *Mater. Lett.*, vol. 197, pp. 111–114, 2017.
- [100] V. García-Cuello, J. C. Moreno-Piraján, L. Giraldo-Gutiérrez, K. Sapag, and G. Zgrablich, "Design, calibration, and testing of a new Tian-Calvet heat-flow microcalorimeter for measurement of differential heats of adsorption," *Instrum. Sci. Technol.*, vol. 36, no. 5, pp. 455–475, 2008.
- [101] D. Uner and M. Uner, "Adsorption calorimetry in supported catalyst characterization: adsorption structure sensitivity on Pt/-Al₂O₃," *Thermochim Acta*, vol. 434, pp. 107–12, 2005.
- [102] P. Kozyra and W. Piskorz, "A comparative computational study on hydrogen adsorption on the Ag⁺, Cu⁺, Mg²⁺, Cd²⁺, and Zn²⁺ cationic sites in zeolites," *Phys. Chem. Chem. Phys.*, vol. 18, pp. 12592–603, 2016.
- [103] J. Chen *et al.*, "Spatial confinement effects of cage-type SAPO molecular sieves on product distribution and coke formation in methanol-to-olefin reaction," *Catal. Commun.*, vol. 46, pp. 36–40, 2014.
- [104] U. Deka, I. Lezcano-Gonzalez, B. M. Weckhuysen, and A. M. Beale, "Local environment and nature of Cu active sites in zeolite-based catalysts for the selective catalytic reduction of NO_x," *ACS Catal.*, vol. 3, pp. 413–427, 2013.
- [105] X. Solans-Monfort *et al.*, "Can Cu⁺-Exchanged Zeolites Store Molecular Hydrogen? An Ab-Initio Periodic Study Compared with Low-Temperature FTIR," *J. Phys. Chem. B*, vol. 108, pp. 8278–8286, 2004.

APPENDICES

A. Cu(I)-ZSM-5

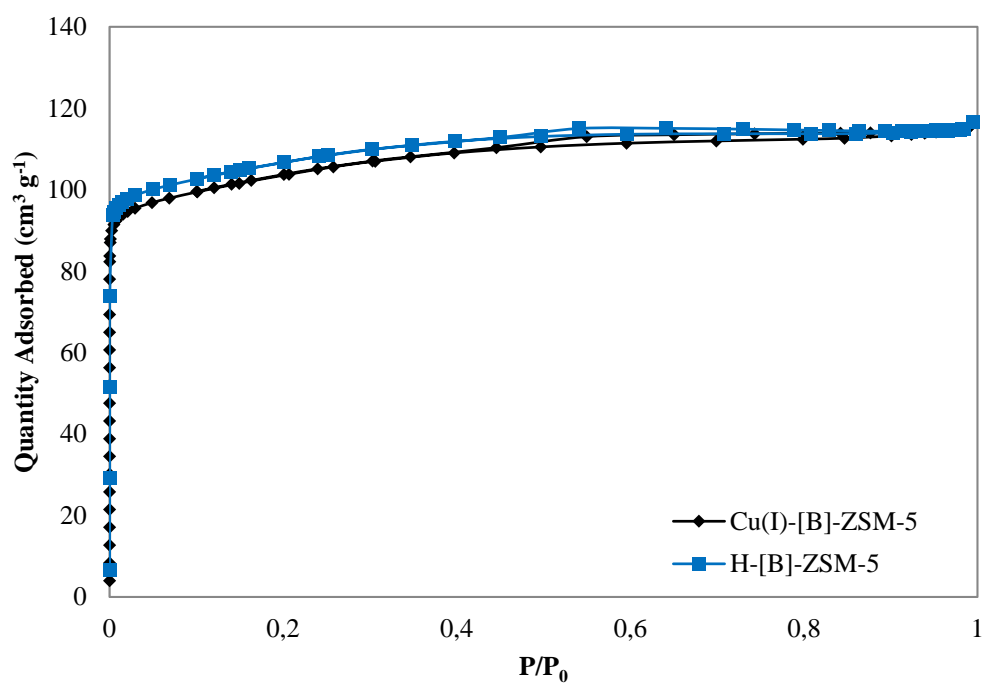


Figure A.1: Nitrogen adsorption/desorption isotherm at 77 K for [B]-ZSM-5

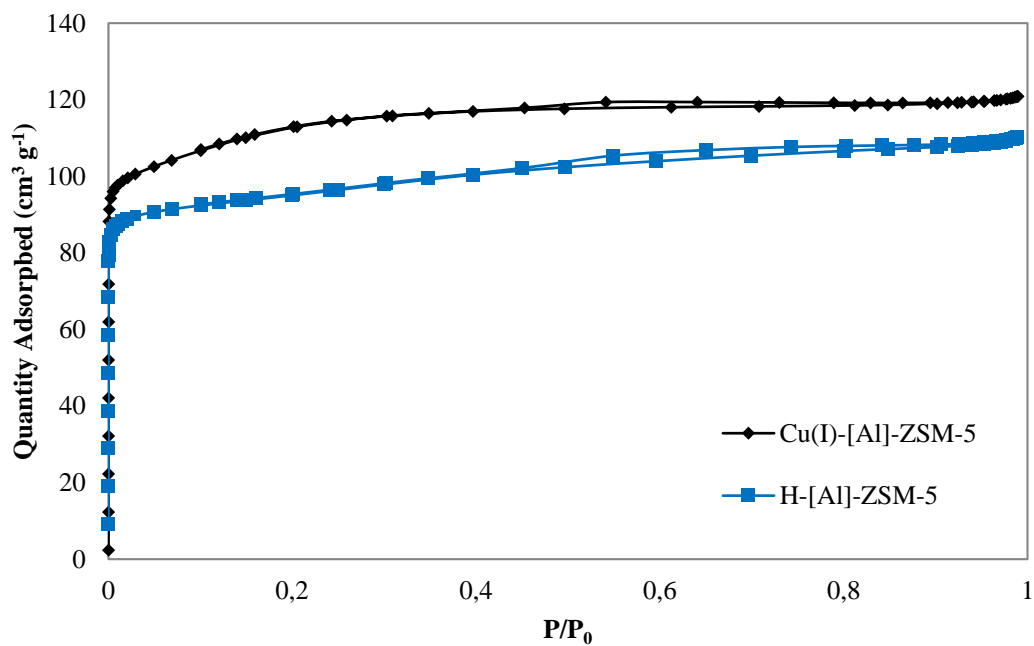


Figure A.2: Nitrogen adsorption/desorption isotherm at 77 K for [Al]-ZSM-5

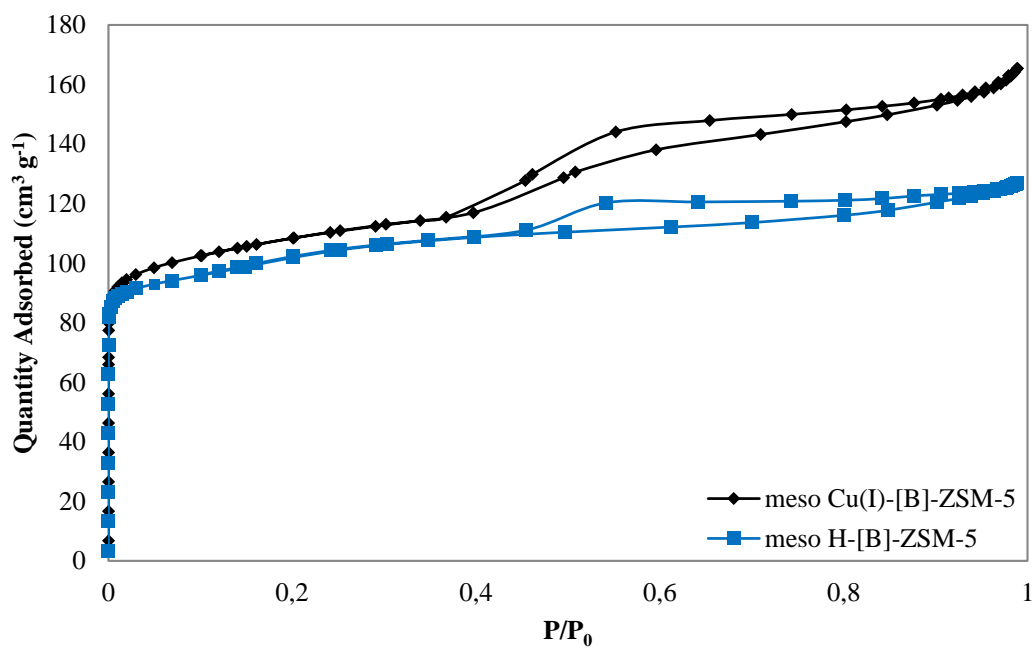


Figure A.3: Nitrogen adsorption/desorption isotherm at 77 K for mesoporous [B]-ZSM-5

Table A.1. H_2 adsorption data obtained from adsorption calorimetry device for Cu(I)-[Al]-ZSM-5

$P_{\text{eq.}}$ (mmHg)	Incremental Quantity of H_2 adsorbed ($\mu\text{mole g}_{\text{zeo}}^{-1}$)	Cumulative Quantity of H_2 adsorbed ($\mu\text{mole g}_{\text{zeo}}^{-1}$)	Heat per peak (J g^{-1})	Differential Heat of Adsorption (kJ mol^{-1})
4.20	1.53	1.53	0.40	261.3
9.00	1.75	3.28	0.09	52.0
14.10	1.86	5.14	0.05	25.2
18.60	2.75	7.89	0.03	11.5
28.10	8.03	15.92	0.06	6.9
39.65	7.03	22.95	0.05	6.9
50.90	4.05	27.00	0.03	8.5
67.65	6.07	33.06	0.04	6.8
96.40	19.57	52.63	0.15	7.6
138.40	10.66	63.29	0.07	6.4
188.10	18.04	81.34	0.06	3.3
237.40	34.96	116.30	0.08	2.4
290.10	25.99	142.29	0.08	2.9
376.40	29.06	171.35	0.10	3.3
431.80	70.34	241.69	0.04	0.6

Table A.2. H_2 adsorption data obtained from adsorption calorimetry device for Cu(I)-[B]-ZSM-5

$P_{\text{eq.}}$ (mmHg)	Incremental Quantity of H_2 adsorbed ($\mu\text{mole g}_{\text{zeo}}^{-1}$)	Cumulative Quantity of H_2 adsorbed ($\mu\text{mole g}_{\text{zeo}}^{-1}$)	Heat per peak (J g^{-1})	Differential Heat of Adsorption (kJ mol^{-1})
9.10	1.10	1.14	0.11	95.4
14.00	0.83	1.97	0.08	94.6
18.65	1.76	3.73	0.09	49.8
30.60	4.85	8.58	0.07	14.4
41.30	3.79	12.37	0.07	18.4
51.10	4.04	16.41	0.04	10.5
73.40	4.95	21.36	0.05	10.8
97.90	7.87	29.22	0.04	4.5
137.00	8.26	37.48	0.08	9.5
187.90	14.17	51.65	0.08	5.7
238.20	28.40	80.06	0.07	2.5
289.20	29.20	109.26	0.05	1.7
380.20	27.71	136.97	0.04	1.4

Table A.3. H_2 adsorption data obtained from adsorption calorimetry device for mesoporous Cu(I)-[B]-ZSM-5

$P_{\text{eq.}}$ (mmHg)	Incremental Quantity of H_2 adsorbed (mole g_{zeo}^{-1})	Cumulative Quantity of H_2 adsorbed ($\mu\text{mole } g_{\text{zeo}}^{-1}$)	Heat per peak ($J g^{-1}$)	Differential Heat of Adsorption ($kJ mol^{-1}$)
4.40	2.67	2.67	0.20	76.5
8.00	2.35	5.01	0.03	11.5
19.20	4.99	10.01	0.16	31.8
32.35	4.61	14.61	0.10	21.3
40.80	4.04	18.66	0.02	4.9
49.30	5.22	23.88	0.03	5.6
71.55	3.37	27.25	0.02	5.3
93.50	7.73	34.98	0.05	6.5
133.40	25.17	60.15	0.08	3.2
190.20	22.17	82.32	0.14	6.2
241.40	14.66	96.98	0.07	5.0
290.90	28.45	125.43	0.04	1.5
378.20	47.29	172.72	0.04	0.9

B. Cu(I)-SSZ-13, -SSZ-39, -US-Y, H₂ Isotherms and Isotheric Heat of Adsorption Calculations

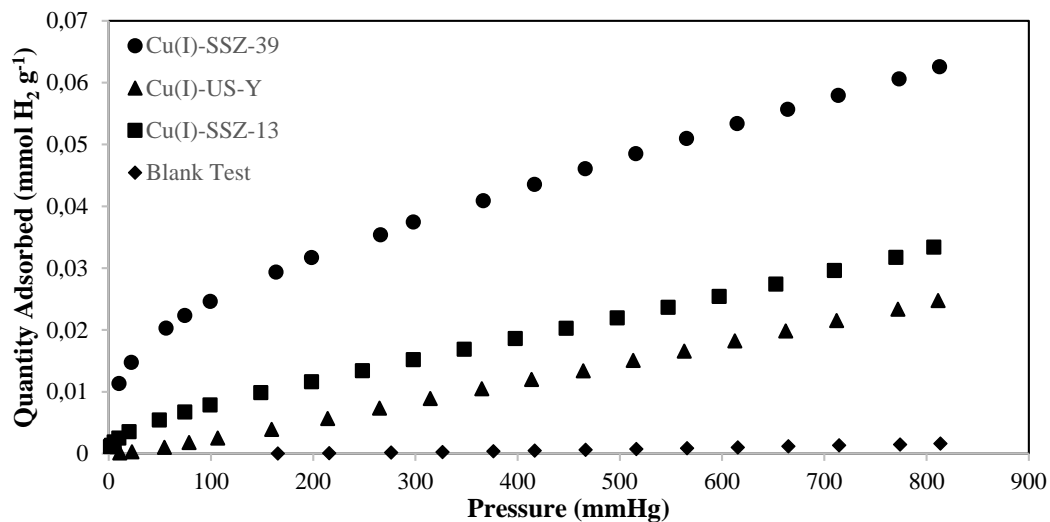


Figure A.4. H₂ adsorption isotherms of Cu(I)-SSZ-39, Cu(I)-US-Y, Cu(I)-SSZ-13 and blank tube at 293 K

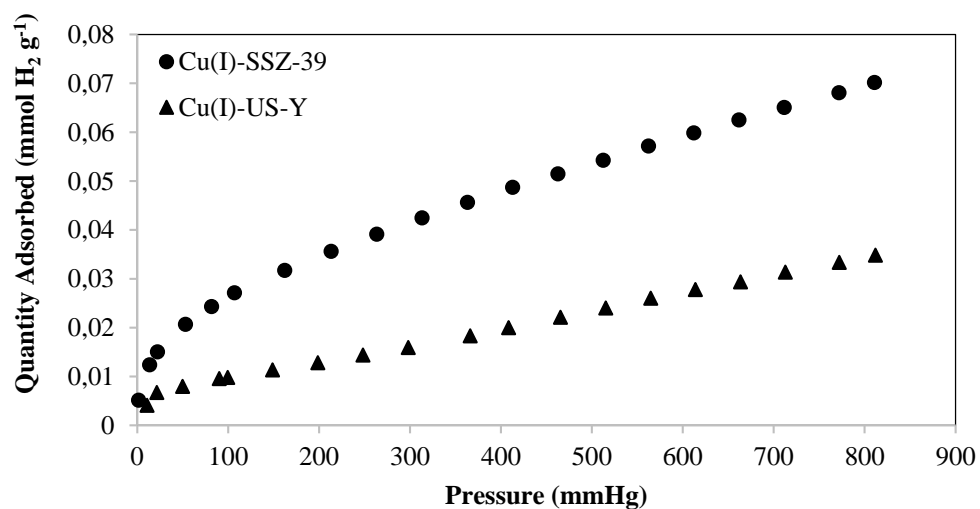


Figure A.5. H₂ adsorption isotherms of Cu(I)-SSZ-13, Cu(I)-SSZ-39, Cu(I)-US-Y, Acid-Cu(I)-SSZ-39 at 278 K

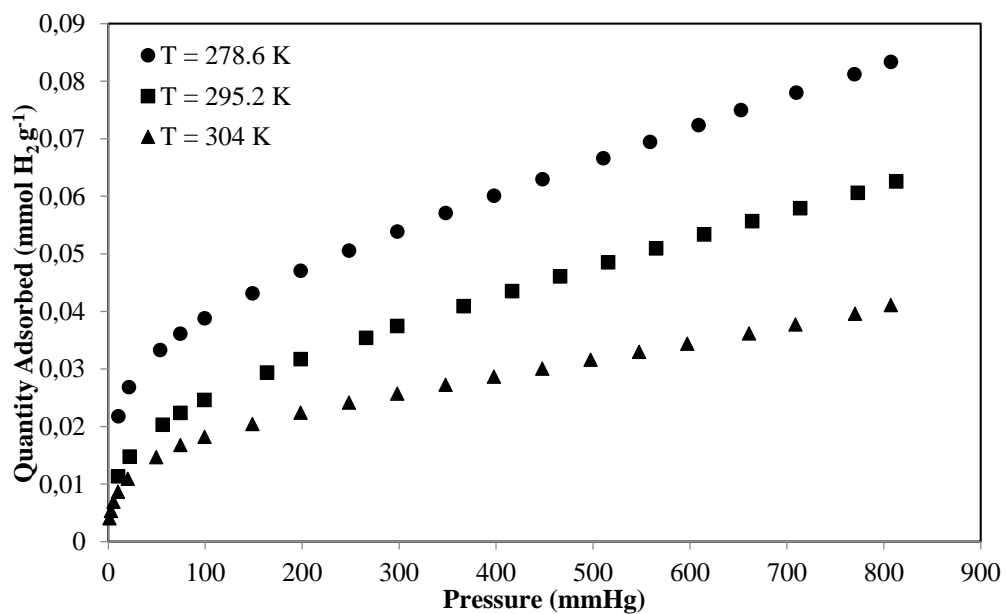


Figure A.6. H₂ adsorption isotherms of Cu(I)-SSZ-39 at different temperatures

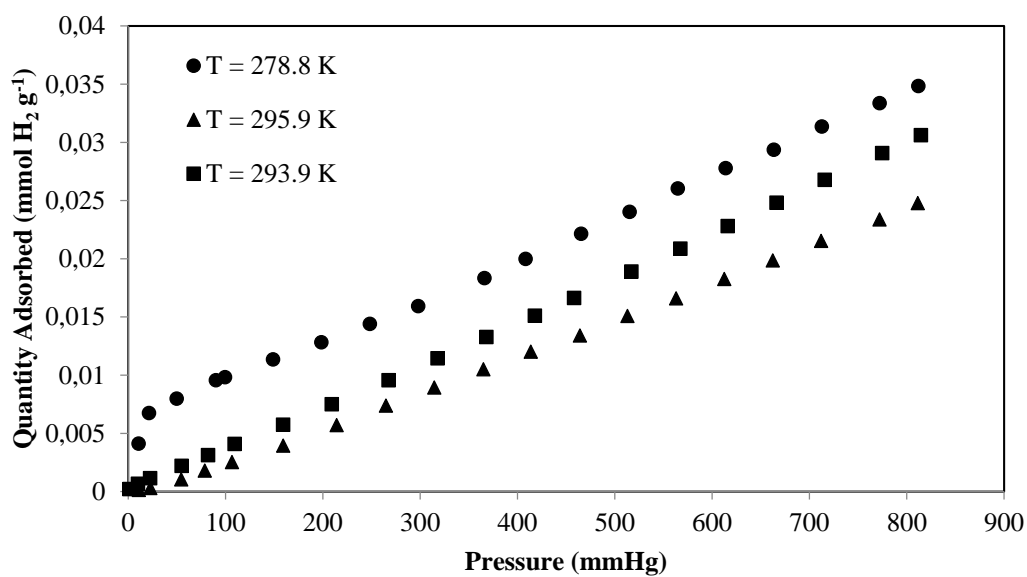


Figure A.7. H₂ adsorption isotherms of Cu(I)-US-Y at different temperatures

Table A.4: Hydrogen adsorption data at different temperatures of Cu(I)-SSZ-39

T = 278.5 K		T = 295.9 K		T = 304 K	
Absolute Pressure (mmHg)	Quantity Adsorbed (mmol g ⁻¹)	Absolute Pressure (mmHg)	Quantity Adsorbed (mmol g ⁻¹)	Absolute Pressure (mmHg)	Quantity Adsorbed (mmol g ⁻¹)
10.4	0.022	10.0	0.011	1.2	0.004
21.2	0.027	22.1	0.015	2.6	0.005
53.5	0.033	56.2	0.020	5.4	0.007
74.4	0.036	74.4	0.022	9.9	0.009
99.4	0.039	99.3	0.025	19.9	0.011
148.8	0.043	163.8	0.029	49.4	0.015
198.4	0.047	198.5	0.032	74.3	0.017
248.3	0.051	265.9	0.035	99.2	0.018
298.2	0.054	298.1	0.037	148.6	0.020
348.2	0.057	366.5	0.041	198.4	0.022
397.9	0.060	416.6	0.044	248.2	0.024
447.9	0.063	466.1	0.046	298.0	0.026
510.7	0.067	515.7	0.049	347.8	0.027
559.0	0.069	565.3	0.051	397.7	0.029
609.0	0.072	614.7	0.053	447.5	0.030
652.8	0.075	664.3	0.056	497.4	0.032
709.8	0.078	713.8	0.058	547.5	0.033
769.7	0.081	773.2	0.061	597.2	0.034
807.4	0.083	812.9	0.063	660.9	0.036
				708.9	0.038
				770.2	0.040
				807.3	0.041

Table A.5: Hydrogen adsorption data at different temperatures of Cu(I)-US-Y

T = 278.8 K		T = 295.9 K		T = 293.9 K	
Absolute Pressure (mmHg)	Quantity Adsorbed (mmol g ⁻¹)	Absolute Pressure (mmHg)	Quantity Adsorbed (mmol g ⁻¹)	Absolute Pressure (mmHg)	Quantity Adsorbed (mmol g ⁻¹)
10.6	0.0041	10.8	0.0001	1.3	0.0002
21.4	0.0067	22.6	0.0003	10.0	0.0007
49.8	0.0080	54.5	0.0010	22.6	0.0011
90.2	0.0096	78.6	0.0018	54.9	0.0022
99.5	0.0098	106.6	0.0025	82.1	0.0031
148.8	0.0113	159.3	0.0039	109.4	0.0041
198.5	0.0128	214.2	0.0057	159.1	0.0057
248.3	0.0144	264.8	0.0074	209.2	0.0075
298.1	0.0159	314.5	0.0089	267.5	0.0096
366.2	0.0183	364.9	0.0105	317.9	0.0114
408.3	0.0200	413.5	0.0120	368.1	0.0133
465.5	0.0221	464.2	0.0134	417.9	0.0151
515.2	0.0240	512.9	0.0151	458.2	0.0166
564.7	0.0260	563.0	0.0166	517.0	0.0189
613.9	0.0278	612.5	0.0183	567.4	0.0209
663.5	0.0294	662.3	0.0199	616.1	0.0228
712.8	0.0314	712.0	0.0215	666.2	0.0248
772.1	0.0334	771.9	0.0234	715.7	0.0268
811.9	0.0348	811.3	0.0248	774.8	0.0291
				814.6	0.0306

The obtained H₂ isotherms are fitted using Sips isotherm model for the low-pressure range and linear model for higher pressure range.

Sips Adsorption Model Equation

$$Q_e = \frac{Q_{max}bP^{1/n}}{1+bP^{1/n}}$$

Linear Adsorption Model Equation

$$Q_e = P_1P + P_2$$

Table A.6. *Cu(I)*-SSZ-39 Sips adsorption model fitting parameters for pressures between 10.40-198.47 mmHg for 278.6 K; 10.09-198.34 mmHg for 295.9 K and 1.25-198.38 mmHg for 304 K.

Temperature (K)	1/n	b (mmHg ^{-1/n})	Q _{max} (mmol g ⁻¹)	R ²
278.6	0.2555	2.948*10 ⁻⁵	4.05*10 ²	0.9987
295.9	0.3969	0.02818	0.167317	0.9987
304	0.3905	0.04985	0.079057	0.9999

Table A.7. *Cu(I)*-SSZ-39 Linear adsorption model fitting parameters for pressures between 198.47-807.40 mmHg for 278.6 K; 198.34-812.95 mmHg for 295.9 K and 198.38-807.30 mmHg for 304 K.

Temperature (K)	P ₁	P ₂	R ²
278.6	5.902*10 ⁻⁵	0.03619	0.9988
295.9	4.984*10 ⁻⁵	0.02247	0.9988
304	2.979*10 ⁻⁵	0.01672	0.9993

Table.A.8 *Cu(I)*-US-Y Linear adsorption model fitting parameters for pressures between 148.80-811.98 mmHg for 278.8 K; 364.94-811.36 mmHg for 293.9 K and 364.94-811.36 mmHg for 295.9 K

Temperature (K)	P ₁	P ₂	R ²
278.8	4*10 ⁻⁵	0.0055	0.9992
293.9	4*10 ⁻⁵	-0.001	0.9998
295.9	3*10 ⁻⁵	-0.0013	0.9996

Isosteric Heat of H₂ Adsorption Calculations

Cu(I)-US-Y

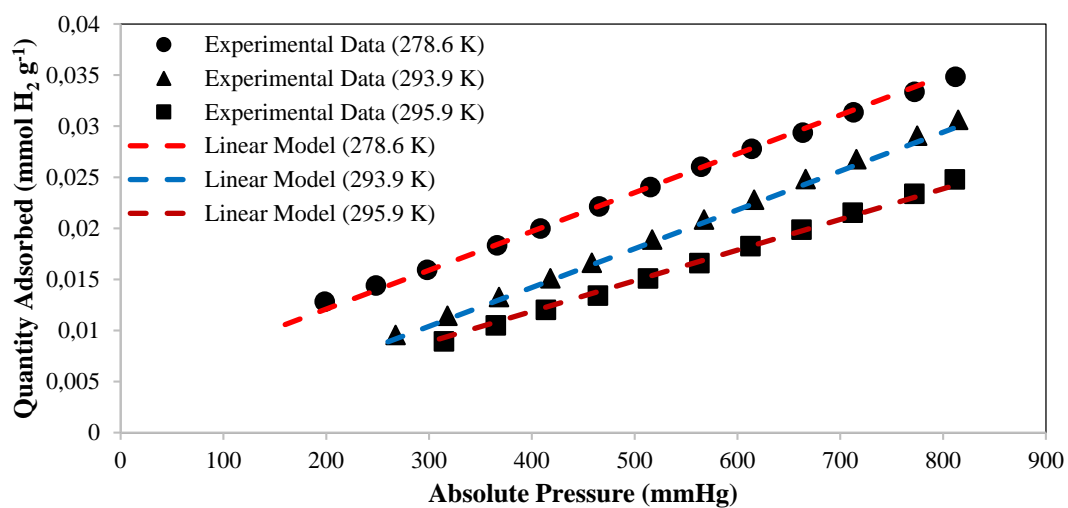


Figure A.8. Experimental H₂ adsorption data on Cu(I)-US-Y at 278.6 K, 293.9 K and 304 K linear models (dashed lines)

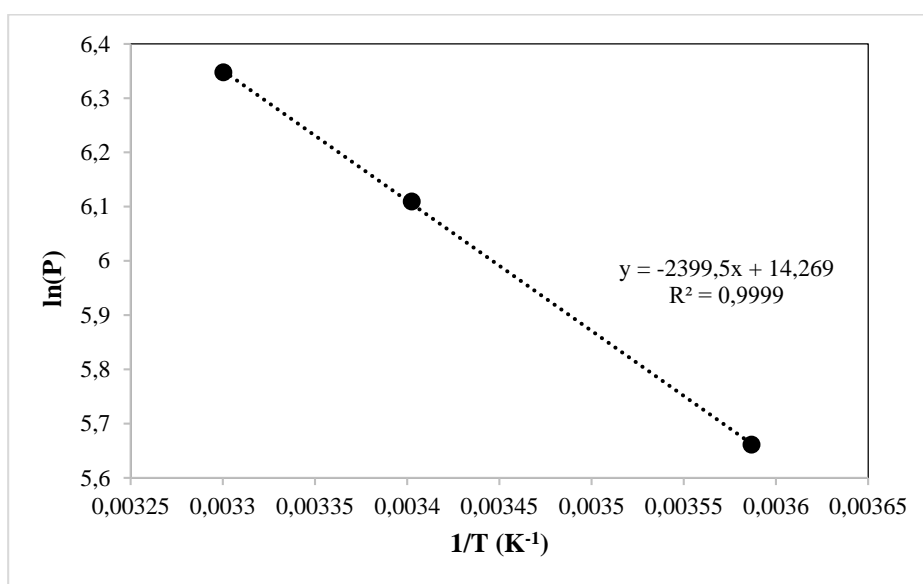


Figure A.9. ln(P) versus 1/T of Cu(I)-US-Y at quantity adsorbed = 0.018 mmol H₂ g⁻¹

Table A.9. Data used to obtain isosteric heat of adsorption of Cu(I)-US-Y between the temperatures 278.6 K and 304 K

n_{adsorbed} (mol)				Q_{st}	R^2
	$\ln(P_{278.6})$	$\ln(P_{293.9})$	$\ln(P_{295.9})$	(kJ mol ⁻¹)	
0.015	5.470	5.991	6.223	22.05	0.9970
0.016	5.570	6.052	6.287	20.92	0.9990
0.017	5.661	6.109	6.347	19.95	0.9999
0.018	5.745	6.163	6.404	19.11	0.9999
0.019	5.822	6.215	6.458	18.38	0.9992
0.02	5.893	6.263	6.509	17.73	0.9978
0.021	5.960	6.310	6.557	17.16	0.9958
0.022	6.022	6.354	6.603	16.64	0.9933
0.023	6.081	6.397	6.648	16.18	0.9905
0.024	6.137	6.438	6.690	15.76	0.9873
0.025	6.189	6.477	6.731	15.38	0.9838
0.026	6.239	6.515	6.770	15.04	0.9801

Cu(I)-SSZ-13

Cu(I)-SSZ-13 (Cu/Al= 1.08, Cu(I)-exchange in 0.04 M CuCl/acetonitrile for 18 hours) sample was tested for H₂ adsorption at temperatures between 278 K and 303 K. However, the XRD pattern obtained after the H₂ tests showed mixture of Cu(I)-SSZ-13 (Cu/Al= 1.08, Cu(I)-exchange in 0.04 M CuCl/acetonitrile for 18 hours) sample with Cu(I)-SSZ-39 (Cu/Al= 0.34, Cu(I)-exchange in 0.04 M CuCl/acetonitrile for 18 hours) sample (Figure A.7). Therefore, the H₂ adsorption isotherms (Figure A.8) and the isosteric heat of H₂ adsorption calculations given in this section represents averaged results for Cu(I)-SSZ-13 and Cu(I)-SSZ-39.

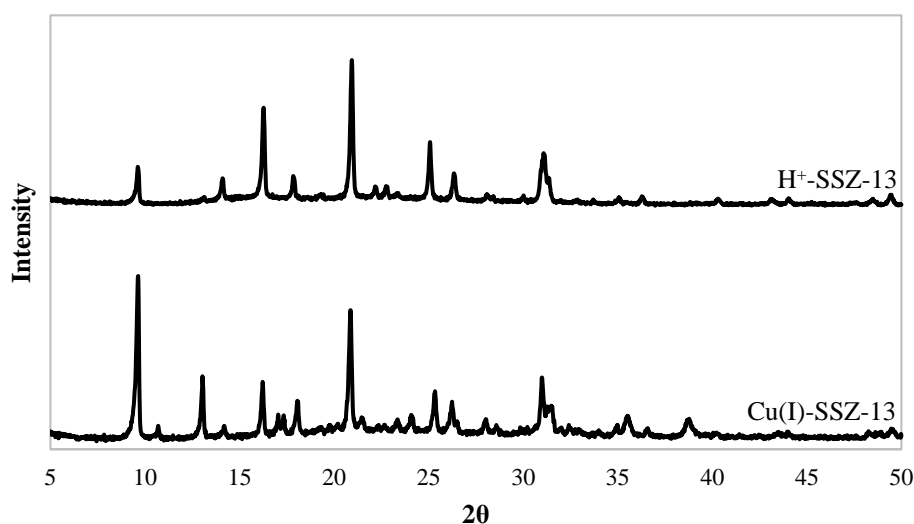


Figure A.10. XRD patterns of SSZ-13 before and after Cu(I)-exchange

Table A.10 : *Hydrogen adsorption data at different temperatures of Cu(I)-SSZ-13*

T = 278.8 K		T = 295.9 K		T = 304 K	
Absolute Pressure (mmHg)	Quantity Adsorbed (mmol g ⁻¹)	Absolute Pressure (mmHg)	Quantity Adsorbed (mmol g ⁻¹)	Absolute Pressure (mmHg)	Quantity Adsorbed (mmol g ⁻¹)
1.5	0.005	1.7	0.004	10.6	0.005
13.6	0.012	11.8	0.008	21.7	0.006
22.3	0.015	22.3	0.010	53.9	0.008
53.1	0.021	59.5	0.014	74.5	0.009
81.9	0.024	81.5	0.016	99.3	0.010
106.9	0.027	109.2	0.017	148.7	0.012
162.2	0.032	159.4	0.019	198.4	0.013
213.3	0.036	215.4	0.021	248.1	0.015
263.4	0.039	258.6	0.023	297.9	0.016
313.4	0.042	317.1	0.024	347.8	0.017
363.3	0.046	367.1	0.025	397.8	0.019
413.0	0.049	416.7	0.027	447.6	0.020
462.8	0.051	466.3	0.028	497.6	0.021
512.5	0.054	515.8	0.029	547.5	0.023
562.3	0.057	565.4	0.030	610.9	0.025
612.2	0.060	614.9	0.032	658.8	0.026
661.9	0.062	664.4	0.033	709.0	0.028
711.7	0.065	713.9	0.034	770.2	0.030
771.9	0.068	773.4	0.036	807.2	0.031
811.1	0.070	813.0	0.037		

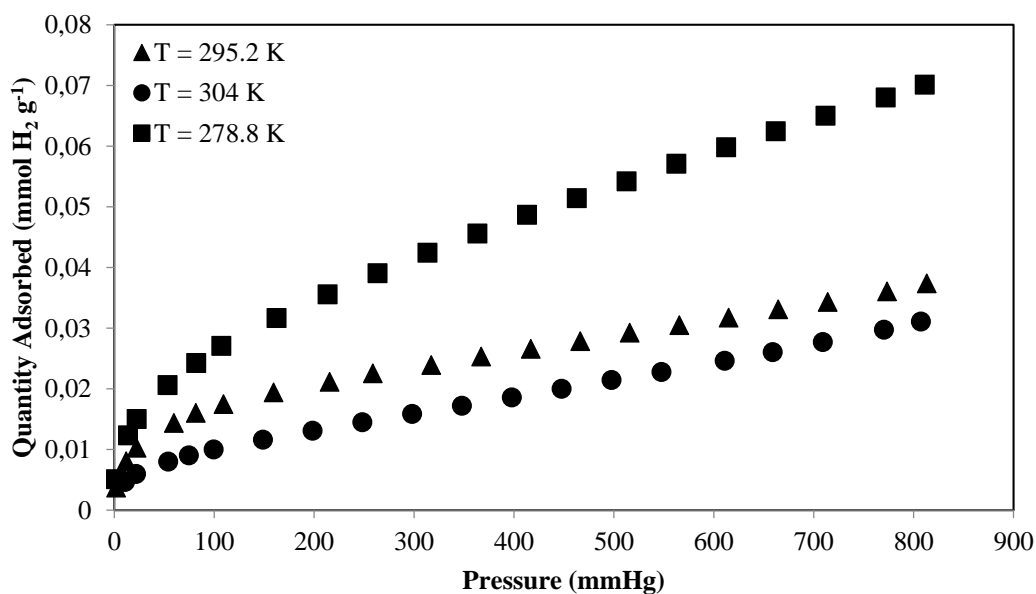


Figure A.11. H₂ adsorption isotherms of Cu(I)-SSZ-13 at different temperatures

Table A.11. Cu(I)-SSZ-13 Sips adsorption model fitting parameters for pressures between 1.55-263.45 mmHg for 278.6 K; 1.78-159.39 mmHg for 295.9 K and 10.60-148.70 mmHg for 304 K

Temperature (K)	1/n	b(mmHg ^{-1/n})	Q _{max} (mmol g ⁻¹)	R ²
278.8	0.4182	0.01181	0.3551	0.9991
295.9	0.4686	0.06471	0.047365	0.9999
304	0.3474	1.766*10 ⁻⁶	1150.623	0.9992

Table A.12. Cu(I)-SSZ-13 Linear adsorption model fitting parameters for pressures between 263.45-811.09 mmHg for 278.6 K; 159.39-813.05 mmHg for 295.9 K and 148.70-807.40 mmHg for 304 K

Temperature (K)	P ₁	P ₂	R ²
278.8	5.834*10 ⁻⁵	0.02376	0.9965
295.9	2.676*10 ⁻⁵	0.0154	0.9994
304	2.905*10 ⁻⁵	0.007161	0.9987

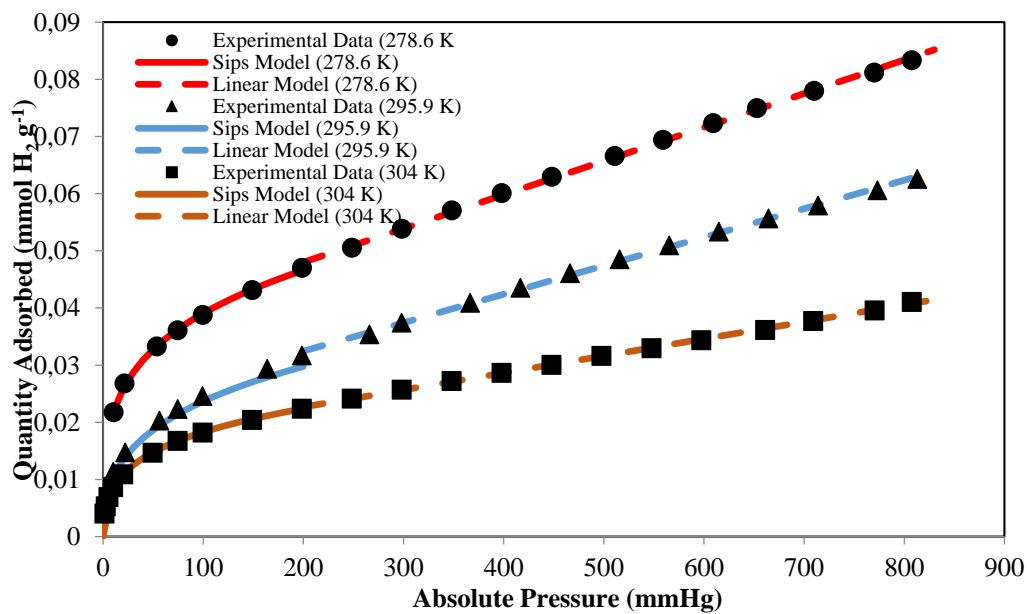


Figure A.12. Experimental H₂ adsorption data on Cu(I)-SSZ-13 at 278.6 K, 295.9 K and 304 K, fitted Sips adsorption (continuous line) and linear models (dashed lines)

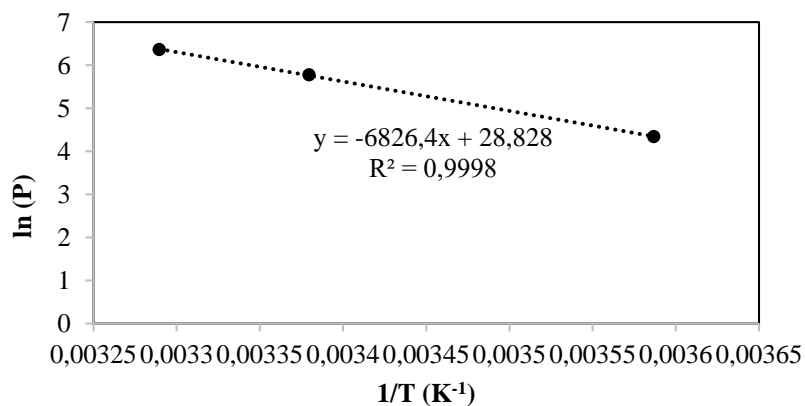


Figure A.13. $\ln(P)$ versus $1/T$ of Cu(I)-SSZ-13 at quantity adsorbed = 0.020 mmol H₂ g⁻¹

Table A.13. Data used to obtain isosteric heat of adsorption of Cu(I)-SSZ-13 between the temperatures 278.6 K and 304 K

n_{adsorbed} (mol)	ln(P_{278.6})	ln(P_{295.9})	ln(P₃₀₄)	Q_{st} (kJ mol⁻¹)	R²
0.024	4.339	5.773	6.362	56.8	0.9998
0.025	4.443	5.883	6.420	55.7	0.9989
0.026	4.544	5.982	6.475	54.6	0.9974
0.027	4.642	6.072	6.526	53.5	0.9956
0.028	4.736	6.155	6.576	52.4	0.9937
0.029	4.827	6.231	6.622	51.3	0.9918
0.030	4.916	6.302	6.667	50.1	0.9899
0.031	5.002	6.368	6.710	48.9	0.9881
0.032	5.085	6.430	6.751	47.9	0.9863
0.033	5.166	6.489	6.791	46.8	0.9847
0.034	5.245	6.544	6.829	45.7	0.9831
0.035	5.322	6.596	6.865	44.6	0.9816